



# **First-principles Studies of Novel Two-dimensional Materials and Their Physical Properties**



**Yierpan Aierken**

Supervisor: Prof. François M. Peeters

Advisor: Dr. Ortwin Leenaerts

Dr. Deniz Çakır

Department of Physics, University of Antwerp

This dissertation is submitted for the degree of  
*Doctor of Philosophy*

Antwerp, Belgium

September 2017



*I would like to dedicate this thesis  
to my loving parents Arkin and Perwin,  
to my beloved wife Adila Dilshat,  
to my cherished sons Esran and Wildan.*



## **Declaration**

I hereby declare that except where specific reference is made to the work of others, the contents of this dissertation are original and have not been submitted in whole or in part for consideration for any other degree or qualification in this, or any other university. This dissertation is my own work and contains nothing which is the outcome of work done in collaboration with others, except as specified in the text and Acknowledgements. This dissertation contains fewer than 65,000 words including appendices, bibliography, footnotes, tables and equations and has fewer than 150 figures.

Yierpan Aierken  
September 2017



## **Acknowledgements**

And I would like to acknowledge ...



## **Abstract**

This is where you write your abstract ...



# Table of contents

<b>List of figures</b>	<b>xv</b>
<b>List of tables</b>	<b>xxi</b>
<b>1 Introduction</b>	<b>1</b>
1.1 Graphene . . . . .	3
1.1.1 History . . . . .	3
1.1.2 Physical properties . . . . .	6
1.2 Post-graphene materials and their general properties . . . . .	7
1.2.1 Functionalized graphene . . . . .	8
1.2.2 Group IV 2D materials . . . . .	10
1.2.3 2D from layered materials . . . . .	11
1.3 1D from 2D: nanotubes and nanoribbons . . . . .	14
1.4 Synthesis methods . . . . .	16
<b>2 Computational methods</b>	<b>19</b>
2.1 Theory . . . . .	19
2.1.1 Density Functional Theory . . . . .	19
2.1.2 Exchange-correlation functional . . . . .	23
2.2 Implementation . . . . .	28
2.2.1 Software Packages . . . . .	31
<b>3 General physical properties of 2D materials</b>	<b>33</b>
3.1 Structural properties . . . . .	33
3.1.1 Layered structure: from multi- to monolayer . . . . .	33
3.1.2 $sp^n$ hybridization . . . . .	37

3.2	Electronic properties . . . . .	39
3.2.1	Graphene . . . . .	39
3.2.2	Dirac cone and symmetry . . . . .	41
3.2.3	Examples: 2D-h-BN, 2D-MoS <sub>2</sub> and graphene . . . . .	42
3.3	Vibrational properties . . . . .	43
3.3.1	Example: 2D-MoS <sub>2</sub> . . . . .	44
3.3.2	Dynamic stability from phonon dispersion . . . . .	46
3.4	Mechanical properties . . . . .	47
3.4.1	Examples: graphene, 2D-BN and 2D-MoS <sub>2</sub> . . . . .	48
3.4.2	Mechanical stability: Born stability criteria . . . . .	49
<b>4</b>	<b>Results of Physical Properties Calculations in Novel 2D Materials</b>	<b>51</b>
4.1	Thermal properties of phosphorene . . . . .	51
4.1.1	Introduction: Phosphorene . . . . .	51
4.1.2	Thermal expansion and Quasi-harmonic approximation .	53
4.1.3	Computational details . . . . .	56
4.1.4	Phonon modes and dispersion . . . . .	56
4.1.5	Results of temperature-dependent thermal properties .	57
4.1.6	Summary . . . . .	60
4.2	Piezoelectric properties of 2D-TMDCs and 2D-TMDOs . . . . .	60
4.2.1	Introduction . . . . .	60
4.2.2	Piezoelectric constants . . . . .	62
4.2.3	Computational details . . . . .	63
4.2.4	Accurate band gaps from HSE06 hybrid functional . . .	64
4.2.5	Elastic constants . . . . .	65
4.2.6	Piezoelectric stress/strain coefficients . . . . .	67
4.2.7	Importance of internal relaxation . . . . .	69
4.2.8	Summary . . . . .	70
4.3	Magnetic properties of penta-hexa-graphene . . . . .	71
4.3.1	Introduction . . . . .	71
4.3.2	Computational details . . . . .	72
4.3.3	Bond hybridization and magnetic moment . . . . .	73
4.3.4	Stability and electronic structure . . . . .	74
4.3.5	Summary . . . . .	76

---

4.4	Battery related properties of MXenes/graphene heterostructure	76
4.4.1	Introduction . . . . .	76
4.4.2	Computational details . . . . .	78
4.4.3	Results . . . . .	79
4.4.4	Conclusion . . . . .	88
4.4.5	Principle of Lithium battery . . . . .	90
4.4.6	Key quantities and their modelling . . . . .	90
<b>5</b>	<b>Results of Physical Properties Modification in Novel 2D materials</b>	<b>93</b>
5.1	Number of layers . . . . .	93
5.1.1	Few-layer of Calcium hydroxide . . . . .	93
5.1.2	Few-layer of pentasilicene . . . . .	108
5.2	Mechanical strain . . . . .	119
5.2.1	Strain modulation of band gap of pentasilicene . . . . .	119
5.2.2	Variation of vibrational modes under strain in phosphorene . . . . .	121
5.2.3	Carrier mobility enhancement in TiS <sub>3</sub> monolayer with strain	125
5.2.4	Carrier mobility . . . . .	125
5.2.5	Magnetic properties modulation in penta-hexa-graphnene with strain . . . . .	125
5.3	Adatom adsorption . . . . .	129
5.3.1	Nitrogen edge-decorated graphene nanoribbon . . . . .	129
5.4	Heterostructures . . . . .	129
5.4.1	Electrical transport in 1T/2H/1T MoS <sub>2</sub> lateral heterostructure . . . . .	131
5.4.2	Li storage and diffusion in MXenes/graphene vertical heterostructure . . . . .	131
5.5	Defect induction . . . . .	131
5.5.1	Faceted blue phosphorene nanotube formed by line defects . . . . .	131
5.5.2	Electronic structure of penta-hexa defects in graphene .	131
<b>6</b>	<b>Conclusions</b>	<b>133</b>
<b>Bibliography</b>		<b>135</b>

<b>List of Publications</b>	<b>159</b>
-----------------------------	------------

# List of figures

1.1	Graphene related publications and patents during the last decade	2
1.2	Relation of graphite, graphene, fullerene and nanotube . . . . .	4
1.3	Graphene lattice and band structure. . . . .	7
1.4	Atomic and electronic structure of graphane . . . . .	9
1.5	Graphite fluoride to fluorographene . . . . .	9
1.6	Group IV 2D materials . . . . .	10
1.7	Layered hexagonal structures of h-BN . . . . .	12
1.8	Layered structures of TMDs . . . . .	13
1.9	Band structure evolution of MoS <sub>2</sub> from bulk to single layer . . .	14
1.10	Chiral vector and different type of nanotubes as obtained by rolling them up in different directions . . . . .	15
1.11	Graphene production setups . . . . .	16
1.12	The growth of graphene on SiC wafer . . . . .	17
1.13	An ultra-large-area graphene film . . . . .	18
2.1	Comparison of different electronic structure calculation methods	20
2.2	Jacob's ladder for DFT approximations . . . . .	25
2.3	MAE of the equilibrium lattice constants and band gaps of different functionals . . . . .	26
2.4	Schematic illustration of the relation between $E_g$ and $E_g^{KS}$ . . .	27

3.1 (a) Energy-momentum dispersion relations of single layer and bilayer graphene as approximated by plane intersections of 3D graphite dispersion relation and (b) their 3D dispersion relations around the K point. (c) Matching of the wavelength in graphite to that in single layer and bilayer graphene. Image is adapted from Ref. [114]. . . . .	34
3.2 (a) The atomic structures of monolayer and layered bulk MoS <sub>2</sub> . (b) The energy-momentum dispersion relation of monolayer MoS <sub>2</sub> as a plane intersection of the 3D dispersion relation. Image is adapted from Ref. [116]. . . . .	36
3.3 Three types of sp hybridized orbitals. Image is adapted from Ref. [118]. . . . .	38
3.4 The formation of $sp^2 \sigma$ and $p_z \pi$ double bond. Image source: Ref. [121] . . . . .	40
3.5 Graphene lattice and its Brillouin zone. Image source: Ref. [14] . .	41
3.6 Possible positions for the second atom (blue area) in order to guarantee the existence of Dirac cones as going from (a) square lattice to (f) hexagonal lattice. The first atom is located at the corners of the unit cell. Image source: Ref. [122] . . . . .	41
3.7 Electronic band structures of 2D-hBN, 2D-MoS <sub>2</sub> and graphene calculated with PBE-GGA functional. . . . .	42
3.8 (a) Phonon modes of layered bulk (first row) and monolayer (second row) MoS <sub>2</sub> at the $\Gamma$ point. (b) Phonon dispersion and projected DOS of monolayer MoS <sub>2</sub> . . . . .	45
3.9 Imaginary frequencies are shown as negative frequencies in a phonon dispersion plot. . . . .	46
3.10 (a) A structure at the convex (left) and the concave (right) of the PES. (b) Searching for a stable structure (phase transition). . . . .	46
4.1 Black and blue phosphorene structures . . . . .	52
4.2 Schematic illustration of the relation between asymmetric interatomic potential and thermal expansion. . . . .	54
4.3 Thermal expansion coefficients of graphite and graphene calculated using QHA (continuous line) and experimental result for graphite (points). Image source: [153] . . . . .	55

---

4.4	Calculated phonon dispersions for pristine (a) black and (b) blue P. (c) Optical phonon modes together with their frequencies (in units of $\text{cm}^{-1}$ ) at the $\Gamma$ point and irreducible representations for black P and blue P . . . . .	57
4.5	(a) Lattice constants and (b) TEC as a function of temperature. Here, ZZ and AC are denoted for the zigzag and armchair directions, respectively. (c) TEC of monolayer MoS <sub>2</sub> for comparison from Ref. [155]. . . . .	58
4.6	Thermal properties variations of phosphorene with temperature	59
4.7	Mechanism of direct piezoelectric effect. Image source: [172] . .	62
4.8	Top and side views of MX <sub>2</sub> where M= Cr, Mo, W, Ti, Zr, Hf, Sn and X=O, S, Se, Te. P denotes the direction of the polarization. Piezoelectric calculations are done in a rectangular cell. . . . .	64
4.9	The calculated PBE-GGA and HSE06 E <sub>gap</sub> values for TMDCs and TMDOs. Here, white * sign indicates that it is a direct band gap material. . . . .	65
4.10	(a) Clamped-ion and (b) relaxed-ion polarization change under applied uniaxial strain ( $\epsilon_{11}$ ) along the x direction for the selected 2D-TMDCs and 2D-TMDOs structures. Piezoelectric coefficient is determined from the slope of the curves. . . . .	67
4.11	The calculated clamped and relaxed-ion (a) piezoelectric stress ( $e_{11}$ ) and (b) piezoelectric strain ( $d_{11}$ ) coefficients. . . . .	68
4.12	Atomic structure of a 2×2 supercell of monolayer ph-graphene. (a) Top view with hexagonal and pentagonal rings marked with red and yellow color, respectively; (b) Side view of the buckled structure. (Visualisation using VESTA [204]) . . . . .	72
4.13	Bond angles in the unit cell of monolayer ph-graphene. . . . .	73
4.14	Phonon dispersion relation of monolayer ph-graphene. . . . .	74
4.15	Electronic band structure of monolayer ph-graphene. The charge densities at the VBM and CBM in the unit cell are shown as insets. The arrows on the atoms indicate the orientation of their magnetic moments. . . . .	75

4.16 An example structure of mono-Ti <sub>2</sub> CO <sub>2</sub> presenting in (a) top view, (b) side view and (c) tilted view. (d) Simplified example structure of M <sub>2</sub> CX <sub>2</sub> +Gr heterostructure in ground state stacking. . . . .	79
4.17 The optimized locations of single Li atoms in different structures and the definition of interlayer distance <i>d</i> , which ignores the Li atom layer. . . . .	82
4.18 The locations of Li atoms intercalation between Ti <sub>2</sub> CO <sub>2</sub> +Gr het- erostructure as an example. . . . .	83
4.19 The average binding energy (a) and the average charge transfer (b) of Li atoms and the voltage profile of M <sub>2</sub> CX <sub>2</sub> +Gr heterostruc- ture as a function of Li concentration. . . . .	85
4.20 Initial guessed and final resulted Lithium diffusion paths between Ti <sub>2</sub> CO <sub>2</sub> +G heterostructure as an example. . . . .	87
4.21 The top view and the side view of Li diffusion paths along the low- est energy diffusion paths in Ti <sub>2</sub> CO <sub>2</sub> related systems as examples.	88
4.22 Energy profiles of the Li diffusions in different systems composed of (a) Sc <sub>2</sub> C(OH) <sub>2</sub> , (b) Ti <sub>2</sub> CO <sub>2</sub> and (c) V <sub>2</sub> CO <sub>2</sub> along the lowest en- ergy diffusion paths as indicated in Fig. 4.21. . . . .	89
5.1 Atomic structure of bulk Ca(OH) <sub>2</sub> : (a) tilted view, (b) top view of one layer. . . . .	94
5.2 (a) Optical image of the crystal structure and (b) Raman spec- trum measured using 488 nm laser in the low and the high fre- quency region. The fundamental phonon branches located at the low frequency (100-400 cm <sup>-1</sup> range) and the high frequency ( 3620 cm <sup>-1</sup> ) are associated with the OH stretching mode. (c) XRD measurements . . . . .	97
5.3 Different stacked bilayers (bottom layer is blurred) and their en- ergy difference with respect to the AA stacking of Ca(OH) <sub>2</sub> , i.e. $\Delta E = E_{ABX} - E_{AA}$ , (X=1,2,...,5). Energies are given per formula of Ca(OH) <sub>2</sub> . Blue, green and red circles are for Ca atom, upper hydroxyl group and lower hydroxyl group, respectively. For clarity, the bottom layer is shifted slightly. . . . .	101

---

5.4	Interlayer interaction energy per formula of AA-stacked bilayer Ca(OH) <sub>2</sub> . Blue and red curves are for GGA calculations without and with vdW correction, respectively. . . . .	102
5.5	(a) and (d) are the Band structures, (b) and (e) are the partial DOS and (c) and (g) are the band and $k$ -point decomposed charge densities of the bulk (c) and monolayer (g) Ca(OH) <sub>2</sub> , respectively. The charge density are the band edges indicated in (a) and (d), isovalue are kept constant. (f) Band structure around $\Gamma$ point is shown with (dashed line) and without (solid line) spin orbit coupling. . . . .	104
5.6	Two lowest conduction band charge density of monolayer and bilayer Ca(OH) <sub>2</sub> at the $\Gamma$ point. . . . .	105
5.7	Phonon dispersion of monolayer Ca(OH) <sub>2</sub> . . . . .	106
5.8	(a) Side view and (b) top view of the atomic structure, (c) phonon spectrum and (d) two vibration modes with imaginary frequency of monolayer penta-silicene. Visualization of vibration modes is done with the V_Sim package [274]. . . . .	109
5.9	Schematic illustration of the four stacking types for bilayer p-Si. The colors of the symbols correspond to those of the monolayer in Fig. 5.8(a) and Fig. 5.8(b). The bottom layer in the bilayer is blurred for clarity. The arrow represents translation and the angle represents the rotation of the top layer with respect to the bottom layer. . . . .	110
5.10	Atomic structure of the $2 \times 2$ supercell of few-layer p-Si. The number of atomic layers in the bulk structure is fixed to four for comparison (i.e. $2 \times 2 \times 4$ and $2 \times 2 \times 2$ supercells for AA and AB <sub>d</sub> stacked bulk p-Si). (Visualisation using VESTA [204]). . . . .	112
5.11	Phonon spectra of different-stacked few-layer p-Si. . . . .	115
5.12	The cohesive energy of monolayer and AA and AB <sub>d</sub> stacked bilayer p-Si as a function of time at a temperature of 100 K under NpT-ensemble. . . . .	116
5.13	Top and side views of the atomic structures of the $2 \times 2$ supercell of the three examined hexagonal silicene bilayers. . . . .	117

5.14	Electronic band structure of AA stacked few-layer and bulk p-Si, and a schematic of the first Brillouin zone. . . . .	119
5.15	(a) Electronic band structure of $\text{AB}_r^d$ stacked few-layer and $\text{AB}_r$ , stacked bulk p-Si, and (b) the corresponding charge distribution of CBM and VBM. The results for the monolayer are shown for comparison. . . . .	120
5.16	Band gaps (a) and band edges for uniaxially (b) and biaxially (c) strained $\text{AB}_r^d$ bilayer p-Si. . . . .	122
5.17	Calculated phonon dispersions for pristine (a) black and (b) blue P. (c) Optical phonon modes together with their frequencies (in units of $\text{cm}^{-1}$ ) at the $\Gamma$ point and irreducible representations for black P and blue P. (c) Optical phonon modes together with their frequencies (in units of $\text{cm}^{-1}$ ) at the $\Gamma$ point and irreducible representations for black P and blue P. . . . .	123
5.18	(Color online) Variation of the $\Gamma$ frequencies with strain: (a) zigzag and (b) armchair direction of black P and (c) blue P. . . . .	124
5.19	AFM to FM transition of monolayer ph-graphene under strain. .	126
5.20	(Color online) Band gap variation of AFM and FM monolayer ph-graphene under strain. . . . .	127
5.21	(Color online) AFM to FM transition through spin-flip in monolayer ph-graphene. . . . .	128
5.22	(a) and (d) vertical and (c) and (d) lateral $\text{WS}_2/\text{MoS}_2$ heterostructures. Image adapted from: [285] . . . . .	130

# List of tables

5.2 Calculated results for different structures of $\text{Ca}(\text{OH})_2$ : lattice constants $a$ , vertical shift of O and H atom $c_O$ $c_H$ , Ca-O and O-H bond length, energy band gap $E_{gap}$ , cohesive energy per atom $E_{coh}$ , charge transfer from Ca atom to O atom $\Delta Q$ , in-plane Young's modulus $E_{xx}$ , $E_{yy}$ , in-plane Poisson's ratio $\nu_{xy}$ , in-plane shear modulus $G_{xy}$ and in-plane stiffness $C$ . For comparison, theoretical calculation on same quantities of BN are shown in the last row. . . . .	100
5.3 The cohesive energy ( $E_{coh}$ ), the interlayer binding distance ( $d_{\text{inter}}$ ), the interlayer binding energy ( $E_{\text{inter}}$ ), number of interlayer bonds ( $N_b$ ) and energy per bond ( $E_{\text{bond}}$ ) of the four possible stacking types of bilayer p-Si. The interlayer binding energy per unit cell is defined as $E_{\text{inter}} = E_{\text{bi}} - 2E_{\text{mono}}$ . . . . .	111
5.4 The layer (space) group for few-layer (bulk) systems. The lattice constant ( $a$ ), the interlayer distance ( $d_{\text{inter}}$ ), the nearest-neighbor bond length range ( $d_{\text{min/max}}$ ), the cohesive energy ( $E_{coh}$ ), and the band gap (PBE) of few-layer and bulk p-Si. . . . .	113
5.5 Mechanical properties of $\text{AB}_r^d$ bilayer p-Si . . . . .	116
5.6 The interlayer distance $d_{\text{inter}}$ , the nearest-neighbor bond length range ( $d_{\text{min/max}}$ ) and the cohesive energy per atom $E_{coh}$ of the most stable hexagonal bilayer silicene and bilayer p-Si. . . . .	118

# **Chapter 1**

## **Introduction**

A new field of research related to both material science and condensed matter physics has been formed since the synthesis of graphene in 2004 [1, 2]. Graphene is a sheet of carbon atoms in a crystal form having a single atomic thickness. Given the thin plane-like structural nature of this type of material, the field is named two-dimensional (2D) material. The synthesis itself together with the phenomenal properties of graphene have led to a Nobel Prize in physics awarded to Andre Geim and Konstantin Novoselov in 2010 [3]. Since then, the field is expanding with the involvement of researchers not only from the young community, but also from the experts who have been working on graphene-related materials like graphite, fullerenes and carbon nanotubes. As a result, research that focused on graphene and related topics are increasing with unprecedented speed, see Fig. 1.1 for the publications and the patents made in the last decade. While a part of the research has been to explore more on the properties of graphene itself and its applications, the other part has been concentrated on the discovery of new 2D materials. It has been evidenced from graphene, same materials having different dimensions can have different properties. For example, as compared to graphite, its monolayer graphene has superior mechanical properties and massless carriers to name a few. Therefore, many materials with hidden properties which will only manifest themselves in other dimensions are yet to be discovered.

On the other hand, with the advent of powerful supercomputer facilities, calculations that seems impossible to finish in a reasonable time now has been made possible. The accuracy of such calculations is the most crucial aspect of

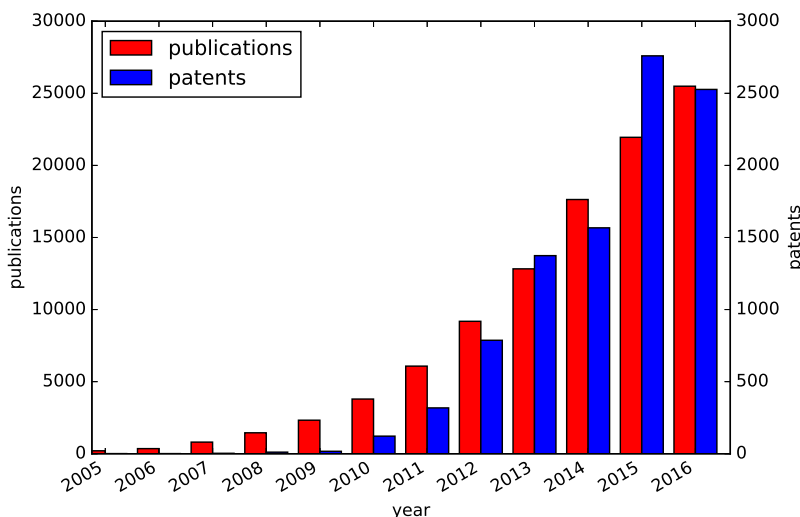


Fig. 1.1 Graphene related publications and patents during the last decade. Data source: ISI Web of Science and PATENTSCOPE.<sup>1</sup>

computational physics, especially when the results are utilized to predict real materials properties. To make the time spent on costly supercomputer valuable, researchers and programmers have been making important progress in order to make sure theories and its implementation are correct and the results they yield are within acceptable precision. Equipped with these tools, theoretical predictions have served well on discovering unexplored properties and applications of the materials. Moreover, detailed characterizations at atomic scale benefit the experimental results as well, or even to explain the unexpected outcomes.

Considering all mentioned, it is a sound approach to apply state-of-the-art computational methods that are accompanied with high-performance supercomputer facilities to investigate the physical properties of novel 2D materials. This thesis was initiated to this end, and it is a summary of several works which have been accomplished during my Ph.D. study. The thesis is organized as follows: For the rest of this chapter, I will first introduce graphene and some other 2D materials that were discovered right after graphene, and, briefly, several well-known methods used to synthesis 2D materials. The following chapter 2 will present the computational methods, the theory and the implementations of

<sup>1</sup>Publication and patent data are obtained by searching for "graphene" in the topic field of Web of Science and the title field of PATENTSCOPE, respectively.

them in available software packages. In chapter 3, I will discuss several general properties of 2D materials. The next two chapters will be the main results of the thesis. Starting from specific properties targeting at specific novel 2D materials in chapter 4, and followed by the modification of physical properties of 2D materials in chapter 5. Overlaps of materials themselves and their properties are inevitable between sections, yet it will be minimized such that each section will have a unique topic.

## 1.1 Graphene

Graphene is composed of carbon (C) atoms arranged on a honeycomb lattice in a single atomic layer. Graphite is made of van der Waals coupled graphene layers, see Fig. 1.2. These layers in graphite are stacked on top of another through weak physical bonds, whereas within each layer C atoms are held together by strong chemical bonds. As a result, it is possible to just isolate a single layer from graphite without damaging the layer itself.

### 1.1.1 History

The story of graphene can be traced back to the discovery of graphite around 1564 in England[5]. Ever since, people have been using graphite, the tip of a pencil, for writing and drawing. The black trace left behind by a pencil is actually stacks of graphite and graphene, and by chance, even a single layer of graphene can present. Apart from being a part of a pencil, graphite certainly has been holding a more important position in technology and industry due to its rich chemistry, low friction, high electrical and thermal conductivity etc. On the other hand, the synthesis of a single layer graphene seems to be discouraged by both experimental and theoretical limitation. On the experimental side, there have been attempts[6–9] to isolate graphene from graphite or even grow it on a substrate. However, they failed mostly due to the poor control of the number of layers and the difficulty to identify graphene itself. Addition to these experimental difficulties, theoretically, it was believed that strictly 2D materials should not exist because of a divergence in the thermal fluctuation in 2D materials that will make them unstable [10–12]. Nevertheless, graphene was still

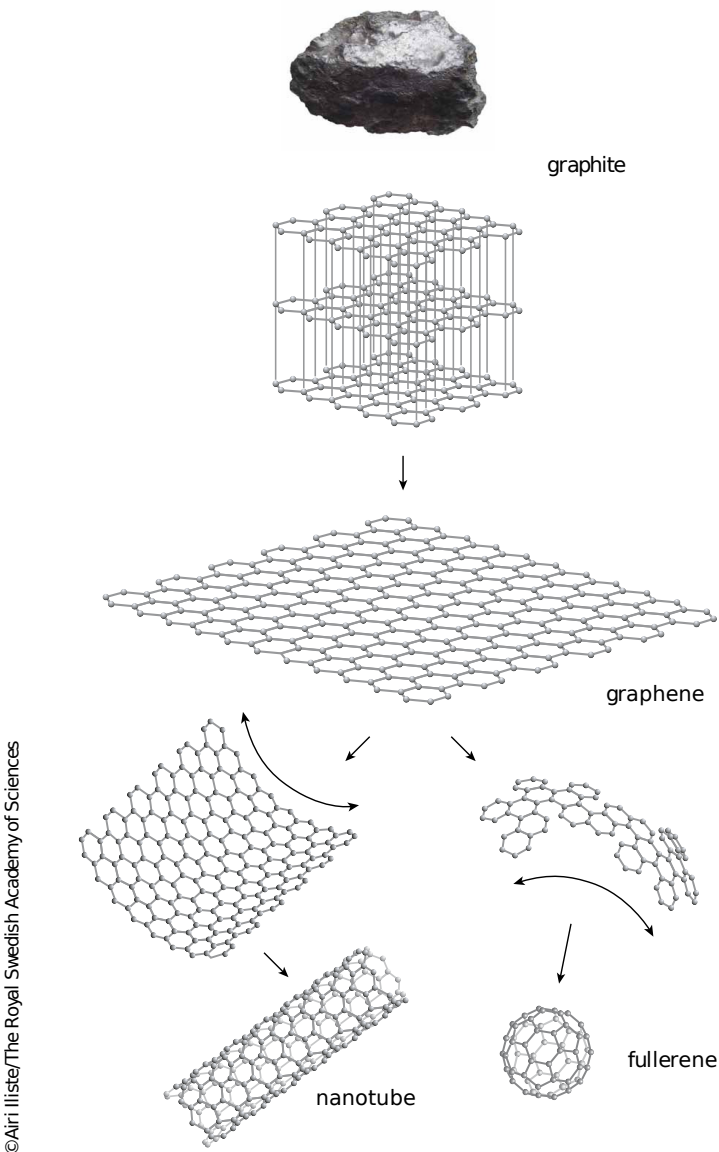


Fig. 1.2 Relation of graphite, graphene, fullerene and nanotube. Image source: the Nobel prize in physics 2010 [4]

considered as a theoretical model. For example, Wallace [13] was the first one to study the band structure of graphene [14], and found some of the interesting properties, like a semimetallic band structure.

Although not in the form of graphene, the single atomic layer of graphite has been already seen and studied in the other forms, e.g. fullerenes and nanotubes, see Fig. 1.2. These materials usually contain certain types of characteristic defects that make it different from graphene. Fullerene has a quasi-spherical hollow ball shape. It is composed of both six- and five-folded C rings, where the latter give positive curvature and made the closed surface possible. The resulting shape resembles a football[15, 16]. The Nobel prize in chemistry of 1996 was award to Harold W. Kroto, Robert F. Curl and Richard E. Smalley for their discovery of fullerene. Another important type of carbon allotrope is carbon nanotubes[17], and it was discovered by using the arc-discharge method[16] which was originally designed to produce a large quantity of fullerenes. Despite sharing similar production method, carbon nanotubes are actually more close to graphene than fullerene due to the absence of pentagonal C rings in the former two. A carbon nanotube can be constructed by rolling up a graphene sheet into a hollow tube as its name suggest. Carbon nanotubes are typically observed to have micrometer in lengths and nanometer in diameter and having either metallic or semiconducting nature depending on the way they are rolled up. They possess superior mechanical properties. For example, individual nanotube has a Young's modulus of 0.64 TPa and it is 56 times stronger than steel wire[18].

In 2004, the situation has changed completely for graphene with the successful isolation of a single layer of graphene from graphite by A. K. Geim and K. S. Novoselov at Manchester University using a simple micromechanical cleavage method. Except for a more sophisticated experimental control, the key ingredient for their success, as compared to the previous failures[6, 7], is that the Si wafer underneath the graphene made it easier to identify graphene[3]. The synthesis of graphene itself already is a ground-breaking achievement, however, what excited the researcher the most is the extraordinary properties that graphene has. In the following section, I will summarize some of them to illustrate this point.

### 1.1.2 Physical properties

As mentioned previously, graphene is a single atomic layer of graphite. It has an interesting structure with high symmetry which many of its properties are attributed to. Each C atom has three neighbors to which it is chemically bonded. Because of this, C atoms are arranged in a honeycomb lattice<sup>2</sup>, or a hexagonal Bravais lattice with two atoms per site, see (a) in Fig. 1.3. Graphene has a uniform bond length of 1.42Å and uniform bond angles of 120°. The band structure which characterizes the electronic properties of graphene has been calculated by P. R. Wallace in 1947 [13]. He discovered that graphene is a semimetal with conduction band minimum (CBM) and valence band maximum (VBM) touch each other at the K and K' points in the first Brillouin zone as shown in (b) and (c) in Fig. 1.3. The energy-momentum dispersion is approximately linear in the vicinity of the K and K' points. Due to this, the electron and the hole in those states behave differently as they do in a quadratic band. This has several consequences. First of all, considering the linear energy momentum relation, particles can be regarded as zero-mass Dirac particles and they are governed by relativistic Dirac equation[19], and they travel at a constant speed of  $10^6$ m/s. Hence, the K and K' points are referred as Dirac points, their vicinities are called Dirac cones. Secondly, the carrier concentration can be tuned continuously from electron to hole with a perpendicular electric field[3]. Thirdly, the carrier in graphene can tunnel through a finite height potential without reflection if it normally incident to the barrier — Klein tunnelling[20]. Fourthly, under a particular magnetic field, a zero energy Landau level appears, and the large energy interval between the zero and the first level made it possible to observe the quantum Hall effect at room temperature [21], etc.

Graphene delivers more than just interesting electronic properties. For example, evidencing the extraordinary mechanical properties, graphene has a Young modulus of 1Tpa and intrinsic strength of 130 Gpa[23]. This makes graphene the strongest material ever measured. More than 300 times stronger than steel and four times harder than diamond. High carrier mobility is another exciting feature that has more applicative importance in electronic devices. Free standing graphene without substrate attached has been reported to has carrier mobility

---

<sup>2</sup>Honeycomb lattice is not a Bravais lattice.

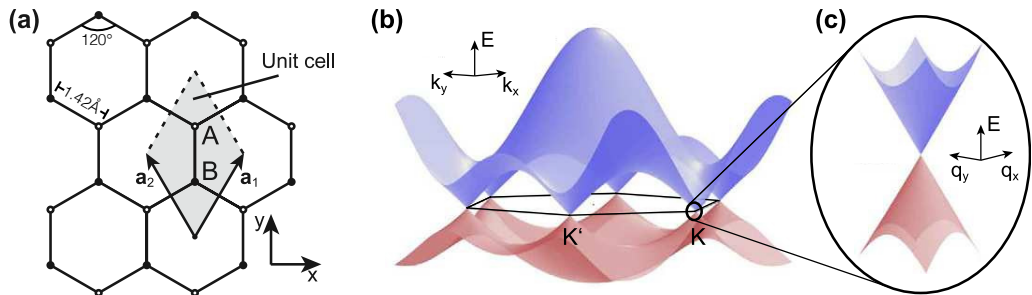


Fig. 1.3 (a) Graphene honeycomb lattice composed of A and B hexagonal Bravais sublattices. (b) Band structure of graphene where CBM and VBM touch each other only at the K and K' points. (c) Approximately linear dispersion around the K and K' points. Image source: Ref. [22]

of  $230,000 \text{ cm}^2/\text{Vs}$  at low temperature[24] and  $120,000 \text{ cm}^2/\text{Vs}$  at 240 Kelvin, the latter value is higher than that of any known semiconductor[25]. In addition, the thermal conductivity of graphene can reach up to  $5000 \text{ W/mK}$  at room temperature, which is 20 times higher than that of copper[26]. Despite these, having a zero band gap strongly suppressed the potential of graphene in digital logic gates applications. This is because the current controlled by the gate bias can not be turned off completely in graphene. To overcome this, efforts to opening a band gap in graphene have been made through substrate induction[27, 28], bilayer graphene[29, 30], chemical adsorption[31, 32], chemical doping[33] and quantum confinements[34, 35]. Doping and adsorption usually come with a price of reducing mobility by introducing scattering centres, chemically pure. In contrast, bilayer graphene and nanoribbon are thought to be promising approaches to open a band gap as well as, to a great extent, preserve graphene's superior intrinsic properties.

## 1.2 Post-graphene materials and their general properties

Excitements of the exploration of graphene have driven the force to discover more types of 2D materials. Researchers have taken different approaches to this end. On the one hand, aiming to open a band gap in graphene, chemical functionalizations on graphene have been carried out with chemical adsorption

of hydrogen, fluorine and oxygen, and resulting in graphane, fluorographene and graphene oxide, respectively. On the other hand, inspired by graphite's layer structure, other layered materials are brought to the attention and efforts were undertaken to isolate a single layer of it. In this section, I will introduce some of these early post-graphene materials and their physical properties in general.

### 1.2.1 Functionalized graphene

#### Graphane

The full hydrogenation of graphene gives a 2-D hydrocarbon called graphane. It can be synthesized either by reduction of graphite and then hydrogenation of the left product (graphene, carbon nanotubes or graphite oxide) with liquid-based[36] or gas-based[37] environments. It can be also grown by chemical vapour deposition[38].

Graphane is not flat as graphene. In fact, the bonding character changed from  $sp^2$  hybridization to  $sp^3$ , which results into a buckled structure, see Fig. 1.4. Neighbouring H atoms located at the different sides of the graphane plane. Among different phases of graphane, the chair structure was found to be the ground state. Others phases are metastable like boat, twist-boat and twist-boat-chair[39]. The C-C bond length in the chair structure is 1.52 Å and thus larger than that in graphene. Graphane is a semiconductor with 3.5 eV band gap in the chair form. The band gap was reported to scale almost linearly with the hydrogen coverage[40]. The 2D Young's modulus of graphane is estimated 245 N/m[41] and thus smaller than 340 N/m of graphene. The incomplete coverage of H atoms on graphene gives hydrogenated graphene. It has a ferromagnetic magnetic state[42], tunable band gap[43] and reversible hydrogenation[31].

#### Fluorographene

Stronger binding between an external atom and a C atom can be realized using fluorine atom for adsorption. A fully fluorinated graphene is called fluorographene, and it can be regarded as a single layer of graphite fluoride. In fact, sonochemical exfoliation of fluorographene from graphite fluoride is one of the ways to synthesis it, see Fig. 1.5[46]. Fluorographene has a similar structure as

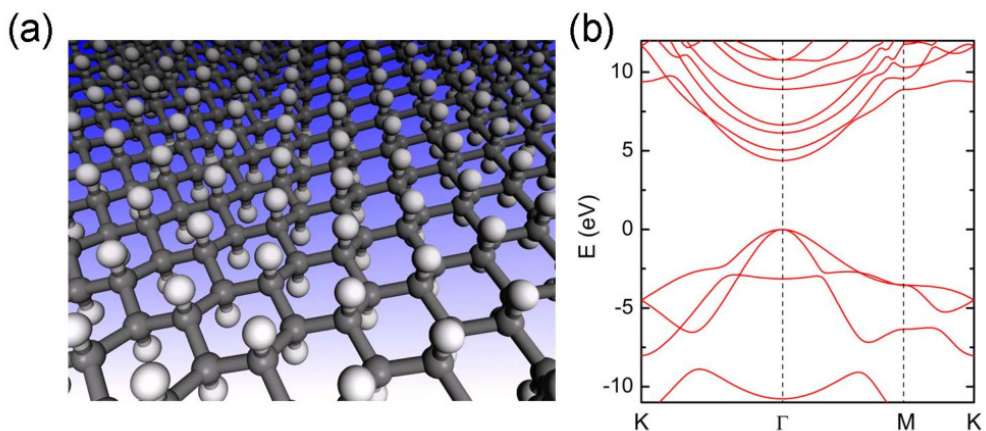


Fig. 1.4 (a)The chair structure of graphane. The white balls are the H atoms and the grey ones are the C atoms. Image source: Ref. [44] (b) Band structure of chair graphane. Image source: Ref. [45]

graphane due to the same  $sp^3$  hybridization, and it also has different isomers where again the chair type is the ground state configuration[47]. The unit cell of fluorographene is around 1% larger than that of graphene[48]. The formation energy of fluorographene is about 0.5 eV per fluorine atom lower than that of graphane per hydrogen atom[32]. The band gap of fluorographene is larger than 3 eV from optical measurement[32, 48], and the band structure is similar to that of graphane with a band gap at the  $\Gamma$  k-point. The 2D Young's modulus of fluorographene is 100 N/m and the intrinsic strength is about 15 N/m. Both are more than two times less than those for graphene due to the weaker  $sp^3$  bonds in fluorographene[48].



Fig. 1.5 Graphite fluoride to fluorographene. Image source: Ref. [46]

### 1.2.2 Group IV 2D materials

Analogues to graphene, 2D materials made of only single elements from the other members of group IV elements have been also proposed and synthesized. These are silicene, germanene, stanene which are made of silicon (Si), germanium (Ge) and tin (Sn) atoms, respectively. They generally suffer from less stability as compared to graphene. The free standing form of these materials are difficult to make, instead, they usually need ordered substrates to support them. Therefore, the measurements that have done on these type of systems can not exclusively speak for the target material, the influence of the substrate is not negligible[49]. This will, in turn, hinder the accurate determination of their properties. Despite of these experimental difficulties, theoretical studies have more freedom to investigate their physical properties. One of the most important differences of these materials as compared to graphene is their not-flat buckled structure, see Fig. 1.6. The buckling parameters  $\delta$  is defined as the interlayer distance of layers at different 2D atomic planes. According to calculations,  $\delta$  is 0.45 Å for silicene, 0.69 Å for germanene and 0.85 Å for stanene[50]. This change corresponds to a more  $sp^3$ -like character in the orbitals, and it increases with the atomic radius.

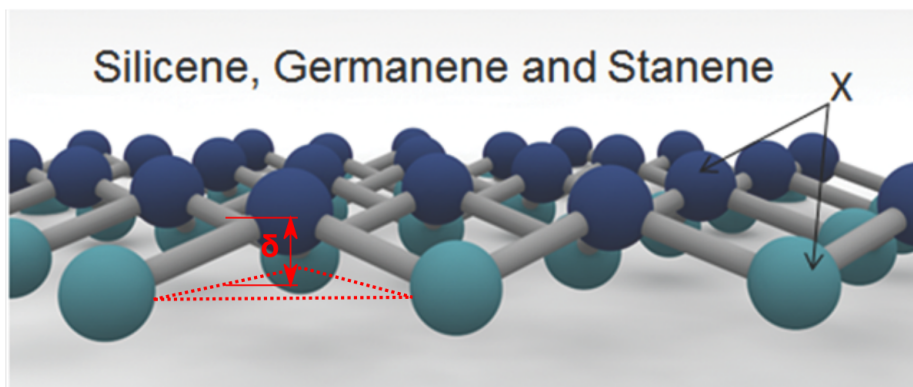


Fig. 1.6 Buckled hexagonal crystal structures of group IV 2D materials ( $X = Si, Ge,$  and  $Sn$ ). Different colors represent different 2D atomic planes and their distance is the buckling parameter  $\delta$ . Image is adapted from Ref. [51].

Although having a buckled structure, these materials also possess Dirac points with linear energy momentum dispersion around them[52]. However, as stated before, the substrate that supports these materials will induce symmetry break-

ing which leads to the loss of the Dirac character of the electrons/holes[49] in these materials. Moreover, spin-orbit coupling (SOC) in these materials are predicted to be larger than that in graphene due to larger atomic weights. With the inclusion of SOC, this corresponds to 1.9 meV band gap in silicene and 101 meV of that in stanene[50]. The mechanical stiffness and strength are lowered as compared to graphene and has a reducing trend with increasing atomic number in this group. This is partially due to the fact that the bond angle deformation in the buckled structure is less costly in energy than bond stretching in a flat structure[53]. For example, silicene has a 2D Young's modulus around 62 N/m, that is four times smaller than graphene. Another important difference of these materials from graphene regards the realization of a monolayer. The lack of layered bulk counterpart of these materials made the mechanical exfoliation inapplicable, which is believed to produce the highest quality sample. Therefore, methods used in this case are either bottom-up decomposition techniques onto highly ordered substrates[54, 55], or top-down methods like chemical exfoliation to isolate grown target monolayer from substrate[56, 57].

### 1.2.3 2D from layered materials

The layered structure of graphite contributes the most to the isolation of graphene. If the interlayer bonding were not the weak vdW interaction but rather a covalent type, even the concept of layers can not stand let alone to break the bonds only in one direction and keep others in the other two directions. Therefore, a reasonable way to explore other 2D materials is through other layered materials, e.g. hexagonal boron nitrides, transition metal dichalcogenides. In this section, I will discuss the general physical properties of these two materials as examples for 2D materials from layered materials.

#### Boron Nitride

Among the multiple structural phases of Boron Nitride, the layered hexagonal phase (h-BN) is the most stable one, see Fig. 1.7 for the structure. A single layer extracted from h-BN gives 2D h-BN. Because of its structural similarity to graphene and its wide band gap it is often referred as white graphene[58]. 2D h-BN has a band gap of 6.1 eV according to calculations. An intuitive tight bind-

ing analysis reveals the band gap, in the case of 2D h-BN, to be proportional to the difference of  $p_z$  orbitals from B and N atoms. For silicene and graphene, this difference is zero thus so is the band gap. Moreover, as a result of different electronegativity, i.e. 2.0 for B and 3.0 for N, ionic character develops which further enlarges the band gap[59]. Several interesting features of this material are reported: strong mechanical stiffness and strength close to graphene[60], a good thermal conductivity of  $100\text{--}270 \text{ W m}^{-1} \text{ K}^{-1}$  for few-layer h-BN[61] as an electrical insulator, a high oxidation resistance up to  $700^\circ\text{C}$  in contrast to  $400^\circ\text{C}$  for graphene[62], etc. Benefiting from its compatible bond length, i.e.  $1.446 \text{ \AA}$ , with graphene ( $1.42$ ), it is a perfect partner for graphene to form heterostructure electronic devices and to serve as a dielectric substrate[63]. Resulting system gives a larger mobility for graphene as compared to  $\text{SiO}_2$  substrate[64] for instance.

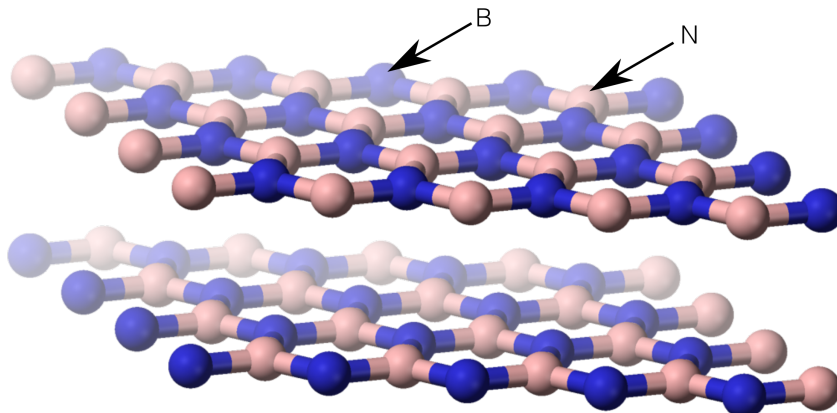


Fig. 1.7 Layered hexagonal crystal structures of h-BN. Image is adapted from Ref. [65].

### Transition Metal Dichalcogenides

Transition metal dichalcogenides (TMDs) have a general formula of  $\text{MX}_2$ , where M stands for the group 4-7 elements in the transition metal series in the periodic table, and X is the group VI element. This is another type of layered materials, and the single layer of some of them have been experimentally realized. These materials typically exist in three different structural phases as shown in Fig. 1.8, which at monolayer level can be either H or T phase. One of the most important

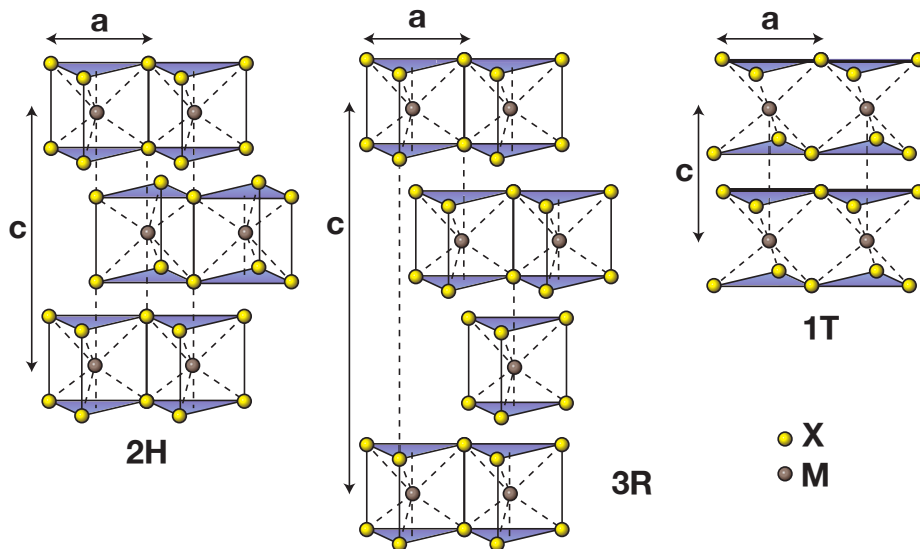


Fig. 1.8 Layered structures of TMDs. 2H: two layers per unit cell with hexagonal symmetry; 3R: three layers per unit cell with rhombohedral symmetry; 1T: one layer per unit cell with tetragonal symmetry.  $a$  is the in-plane lattice constant with a range from 3.1 to 3.7 Å in TMDs.  $c$  is the vertical lattice constant. The interlayer distance has a typical length of 6.5 Å. Image source: Ref. [66]

differences in these two phases is the lack of inversion symmetry in H phase in contrast to the T phase. Therefore, spin orbit coupling (SOC) becomes more important in H and induces spin-splitting. For instance, 456 meV electron spin states splitting in WSe<sub>2</sub>[67] has been reported. Note that, inversion symmetry is recovered in the layered bulk form hence suppresses SOC. Another important consequence of reducing dimensionality is the indirect-to-direct band gap transition from layered TMDs to its 2D counterpart, see for example Fig. 1.9. 2D-TMDs have a broad range of potential applications. Electrocatalysis[68, 69] benefits from adequate active sites, electronic devices[70, 71] benefit from typical band gap of 1-2 eV, Li or Na batteries[72, 73] benefit from high surface-to-volume ratio and short diffusion path, photocatalysis benefits from high stability under extreme light intensity[74, 75], and biomedicine benefits from enhancement of the physiological stability and biocompatibility of polymers on 2D-TMDs[76, 77].

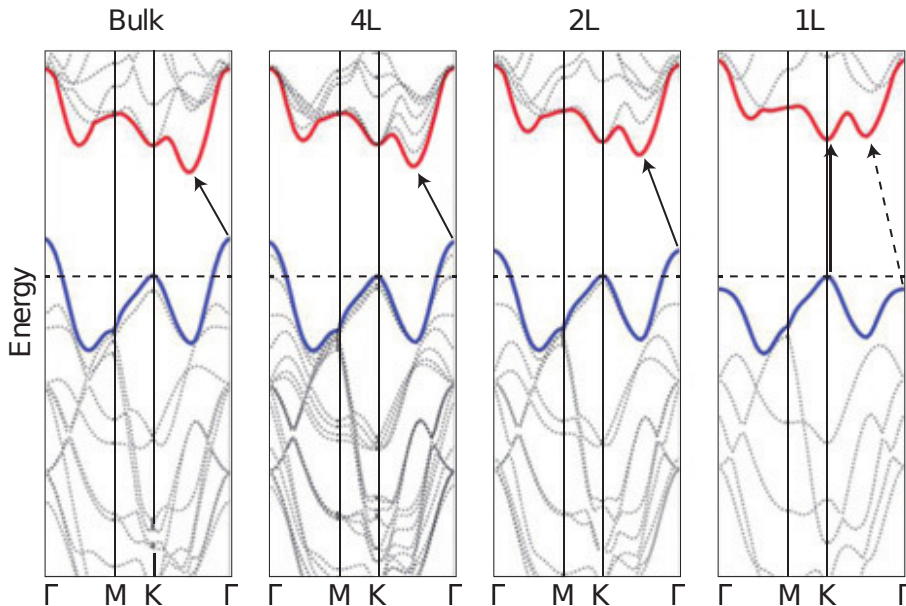


Fig. 1.9 Band structure evolution of MoS<sub>2</sub> from bulk to single layer. Image source: Ref. [78]

### 1.3 1D from 2D: nanotubes and nanoribbons

The reduction of materials dimensions did not stop at the 2D level. Further lowering it will result in 1D nanotubes or nanoribbons. A nanoribbon is a strip of a 2D sheet with nanoscale width and microscale length and it is still flat. Whereas nanotubes are the rolling up of nanoribbons into a tube structure. Each nanotube, as well as each nanoribbon but with different definition, is associated with a chiral vector that uniquely defines its structure parameters except for the length which is considered to be infinite in theory. In Fig. 1.10,  $\vec{a}_1$  and  $\vec{a}_2$  are the unit lattice vectors in graphene. Chiral vector,  $\vec{C}$ , is the superposition of these two unit vectors with indices pair  $(n,m)$ . Zigzag edge always has a  $(n,0)$  form and  $(n,n)$  is always an armchair edge. Everything else is called chiral type edge. This finite-length chiral vector also defines the radius of the tube. Nanoribbons, on the other hand, have these three types of edges as well, however, in this case, edges have infinite length.

Having confinements from other directions, physical properties of these systems are expected to be different than that for their higher dimension counterparts. For example, graphene nanoribbons have a finite band gap in contrast

to the zero band gap of graphene[79]. Moreover, control of this confinement will give tunable physical properties. For example, the band gap in graphene nanoribbon has a overall inverse relation with the width of the nanoribbon[80]. The zigzag edges in graphene nanoribbon form spin-polarized magnetic states and give ferromagnetic ordering along the edge and anti-ferromagnetic ordering across the edges[81]. For nanotubes, those having the same edges belong to the same class of chirality and have the same electronic structure. For instance, armchair carbon nanotubes are metallic, other types are semiconducting. But small radius tubes can be exceptional due to the large curvature[82]. The strong mechanical strength and high thermal conductivity of a graphene nanoribbons and nanotubes are similar to those in graphene.

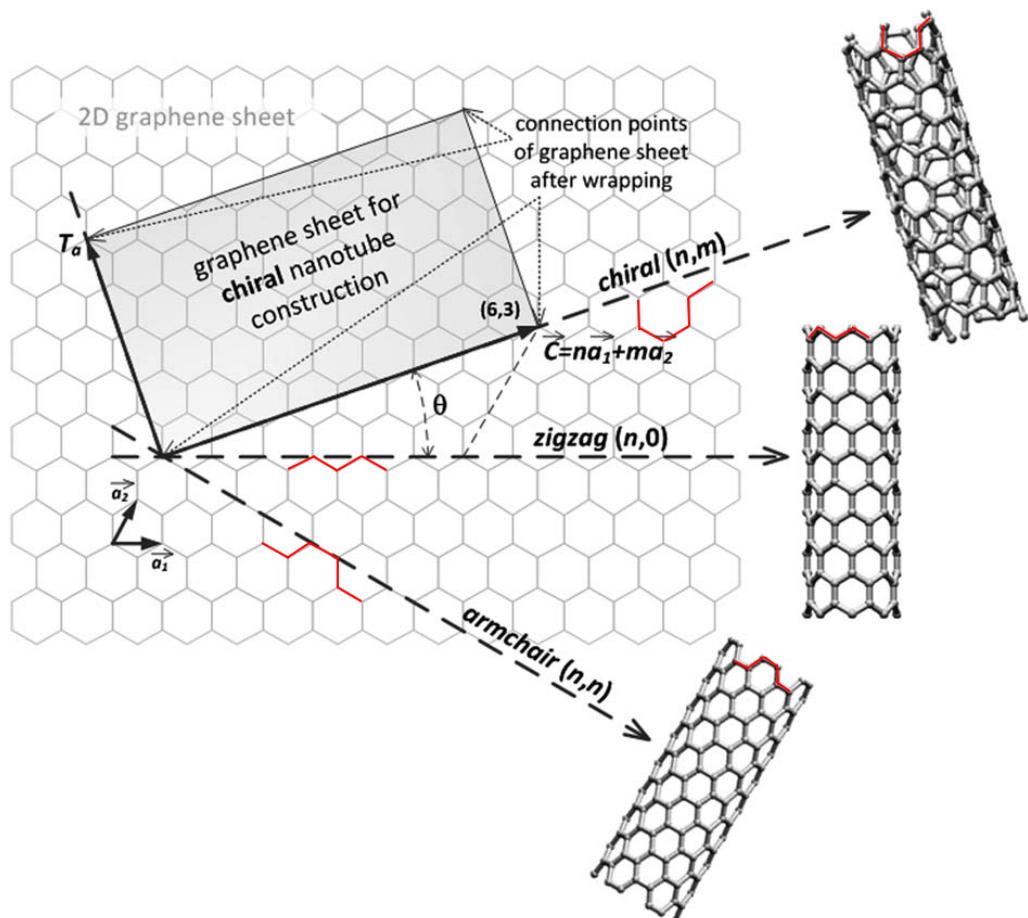


Fig. 1.10 Chiral vector and different types of nanotubes as obtained by rolling them up in different directions. Image is adapted from Ref. [83].

## 1.4 Synthesis methods

In this last section, I will briefly discuss some of the well-known synthesis methods for 2D materials. In Fig. 1.11, an overview of graphene production methods is displayed.

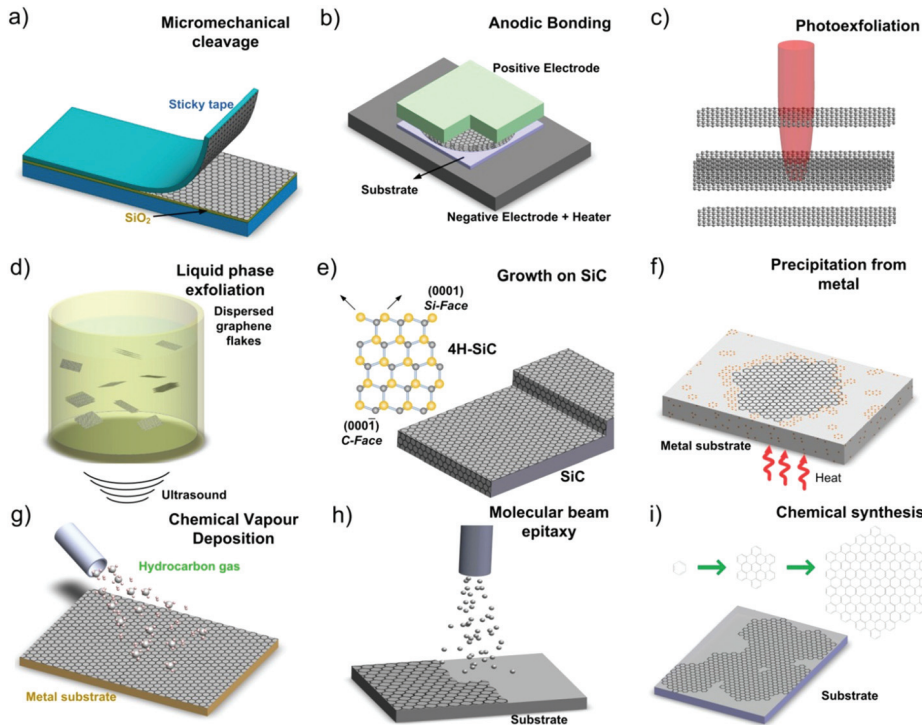


Fig. 1.11 Graphene production setups. Image source: Ref. [84]

### Micromechanical cleavage

Micromechanical cleavage is also known as mechanical exfoliation, which was the method used to the first successful isolation of graphene in 2004 using an adhesive tape[2]. It involves separating layers in layered materials by mechanical, electrostatic, or electromagnetic forces. This method gives high-quality product and is suitable for laboratory-scale sample that is ideal for fundamental studies. Large scale productions are impractical through this method. Room temperature mobility was measured up to  $20,000 \text{ cm}^2 \text{V}^{-1} \text{s}^{-1}$ [85] on graphene prepared with this method.

### Liquid phase exfoliation

Liquid phase exfoliation is the extraction of layers in a proper solvent using ultrasonics. The cavitation-induced bubbles collapse around the graphite will generate a compressive stress wave. As a primary result, this will cause a reflective tensile wave whose strength is proportional to the number of such bubbles. Intensive tensile stress is enough to break graphite into graphite flakes. Additionally, as a secondary effect, shear effect can be developed from the unbalanced lateral stress and separates two adjacent layers. Liquid phase exfoliation is a promising method to synthesis cheap and scalable samples.

### Growth on SiC

The growth of graphene on SiC involves SiC sample annealing at high temperature ( $> 1400^{\circ}\text{C}$ ) in a vacuum or under an atmospheric pressure. The sublimation of silicon atoms leaves behind carbon atoms on the surface which will rearrange to form a graphitic layer[86], see Fig. 1.12. Apart from having high reproducibility and the ability to grow homogeneous large-area sample, this method has the advantage that graphene is available on a semiconducting substrate already for a layered electronic device integration.

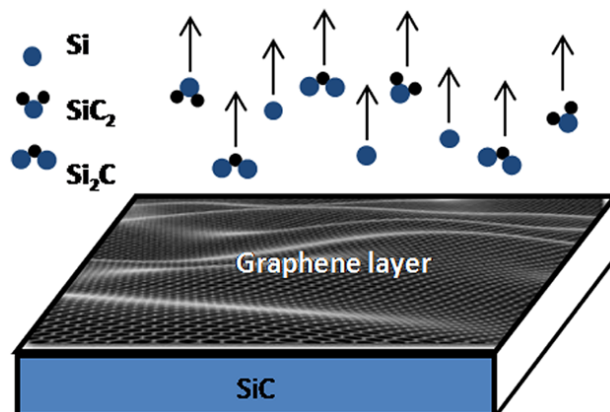


Fig. 1.12 The growth of graphene on SiC wafer. Image source: Ref. [86]

### Chemical vapor deposition

Chemical vapor deposition (CVD) is a popular method to grow amorphous or crystalline thin film from solid, gaseous or liquid precursors. It is a direct deposition of vaporized desired material onto a particular substrate. Various CVD methods exist depending on their operating pressure, types of vaporization and whether it is plasma-assisted or not etc. Graphene grown on transition metals usually is of high quality. Carbon atoms from organic sources in the gas phase are deposited on a metal (Ni, Ru, Ir etc.) and convert to graphene at high temperature. Then, for the characterization, graphene is transferred to a proper substrate. Typical mobility of such type of sample is around  $1000\text{-}25000 \text{ cm}^2\text{V}^{-1}\text{s}^{-1}$ [87]. A 30-inch graphene film has been produced from roll-to-roll production through CVD methods by Bae *et al.* [88], see Fig. 1.13. The product was measured to be a better electrode than commercially available indium tin oxides.

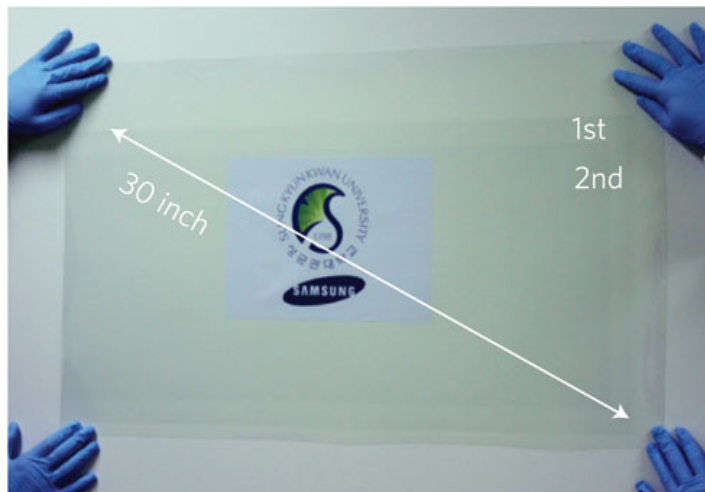


Fig. 1.13 An ultra-large-area graphene film. Image source: Ref. [88]

# **Chapter 2**

## **Computational methods**

Theories behind the calculations are the core component in the material properties determination process. Its correctness, accuracy and implementation directly influence the quality of its predictions. In this chapter, I will introduce relevant theoretical models, approximations and their implementations in commonly used software packages.

### **2.1 Theory**

#### **2.1.1 Density Functional Theory**

Density functional theory (DFT) is one of the most widely used quantum mechanical methods to calculate the properties of materials. Its applicable length and time scales are in nanometre and picoseconds, respectively. These scales are longer than that for quantum Monte Carlo simulations but lower than that for semi- or full-empirical methods. This is also true in the accuracy verse size-of-the-system plot in Fig. 2.1. However, the accuracy of the different methods can be higher than what is shown in the figure, this is because a large part of the error can be attributed to the uncertainty of the experimental results that these methods are compared to[89]. As I will discuss in the later section, if a DFT method is compared with a highly accurate theoretical benchmark method, DFT would have a precision around 1 meV/atom. Particularly, for bulk or nanostructures, DFT can be used to even quantitatively predict the properties of materials. Since DFT is based on Hohenberg-Kohn theorems[90] and Kohn-Sham

equations[91], here I will briefly give an overview of these two methods without putting too much stress on their derivations which have been extensively documented in textbooks. Materials are made from atoms that contain electrons

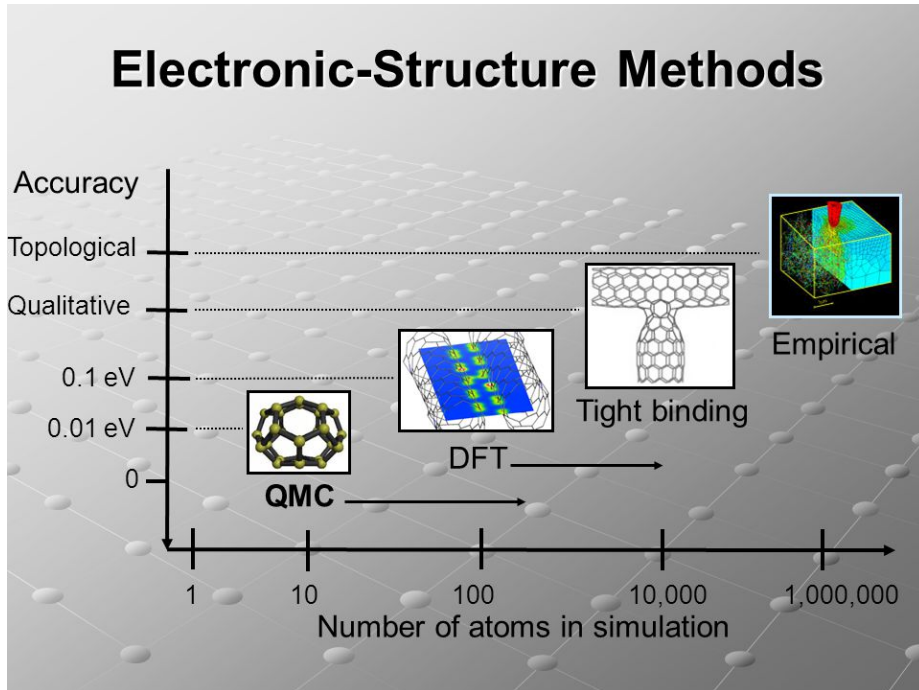


Fig. 2.1 Comparison of the accuracy and the size of different electronic structure calculation methods. Image source: Ref. [92]

and nuclei. The type of the nuclei and the interactions between these give rise to various materials and their properties. The interactions are mainly electrostatic or Coulombic. While electrons must be described with quantum mechanics, the nuclei can be treated as classical particles. The equation governing the electron

behaviour is the Schrödinger equation. It can be written as follows:<sup>1</sup>

$$\begin{aligned}
 \hat{H}\psi_\alpha(\vec{r}_1\sigma_1, \dots, \vec{r}_N\sigma_N) &= \left[ -\frac{1}{2} \sum_{i=1}^N \nabla_i^2 + \sum_{i=1}^N v(\vec{r}_i) + \frac{1}{2} \sum_{i=1} \sum_{j \neq i} \frac{1}{|\vec{r}_i - \vec{r}_j|} \right] \psi_\alpha(\vec{r}_1\sigma_1, \dots, \vec{r}_N\sigma_N) \\
 &= (\hat{T} + \hat{V}_{\text{ext}} + \hat{V}_{\text{ee}}) \psi_\alpha(\vec{r}_1\sigma_1, \dots, \vec{r}_N\sigma_N) \\
 &= E_\alpha \psi_\alpha(\vec{r}_1\sigma_1, \dots, \vec{r}_N\sigma_N).
 \end{aligned} \tag{2.1}$$

In the above equation,  $\hat{H}$  is the total Hamiltonian,  $\hat{T}$  is the kinetic energy,  $\hat{V}_{\text{ext}}$  is the interaction between electrons and nuclei. Here we already started with the first approximation: Born–Oppenheimer approximation[93]. This approximation neglects the dynamics of nuclei, thus electrons are considered moving in a static potential generated by their interaction with all nuclei.  $\hat{V}_{\text{ee}}$  is the interaction between electrons. The first two terms sum over all  $N$ -electrons, and the last one sums over all pairs of  $N$ -electrons.  $\vec{r}$  is the electron position,  $\sigma$  is the z-component of the electron spin ( $+\frac{1}{2}, -\frac{1}{2}$ ).  $\psi$  is the  $N$ -electron wave function, which should be antisymmetric under the interchange of the orbital and the spin coordinates of two electrons (i.e. fermionic character for electrons) and it should also satisfy the boundary condition of the system (e.g. quantum confinement in a low-dimensional system).  $E$  is the total energy, and  $\alpha$  is the complete set of  $N$ -electron quantum numbers.

Following the constrained search algorithm introduced by M. Levy[94], the ground-state energy  $E$  can be found by minimizing the expectation value of the total Hamiltonian with respect to the wave function:

$$E = \min_{\psi} \langle \psi | \hat{H} | \psi \rangle. \tag{2.2}$$

Here we take two steps for the minimization. For the first step, we minimize with respect to all wave functions that give the same density  $n(\vec{r})$ :

$$E = \min_{\psi \rightarrow n} \langle \psi | \hat{T} + \hat{V}_{\text{ee}} | \psi \rangle + \int d\vec{r}^3 v(\vec{r}) n(\vec{r}). \tag{2.3}$$

---

<sup>1</sup>Equations in this chapter are written in cgs form: length, mass, time and energy are in the units of centimetre, gram, second and erg, respectively. Additionally, fundamental constants  $\hbar$ ,  $e^2$  and  $m$  are set to unity.

Then with the resulting wave function  $\psi_n^{min}$  that yields the minimum energy  $E$  and is associated with the density  $n(\vec{r})$ , we can construct the universal functional  $F[n(\vec{r})]$ :

$$\min_{\psi \rightarrow n} \langle \psi | \hat{T} + \hat{V}_{ee} | \psi \rangle = \langle \psi_n^{min} | \hat{T} + \hat{V}_{ee} | \psi_n^{min} \rangle = F[n(\vec{r})]. \quad (2.4)$$

As can be seen in this equation, a functional is a function of a function. For the second step, we minimize with respect to all densities  $n(\vec{r})$ :

$$E = \min_n \left\{ F[n(\vec{r})] + \int dr^3 v(\vec{r}) n(\vec{r}) \right\}, \quad (2.5)$$

where  $v(\vec{r})$  is kept fixed during the minimization. The resulting density is the ground-state density that gives the lowest ground state energy. This is known as the density variational principle, which is also the main idea of the Hohenberg-Kohn theorems. For the completeness, the theorems are present in the following:

**Theorem 1** *The external potential,  $V_{ext}(\vec{r})$ , of any system of interacting particles is uniquely determined (up to a constant) by the particle density,  $n_0(\vec{r})$ , of the ground state.*

**Theorem 2** *The ground state energy of a system with an external potential  $V_{ext}(\vec{r})$  is given by the minimum value of the energy functional  $E_{HK}[n]$  and the density for which this minimum is reached corresponds with the ground state density  $n_0(\vec{r})$ .*

Now, the main problem is to find an approximated expression of  $F[n(\vec{r})]$ . Kohn-Sham equation is a elegant way to do this. It aims to construct a non-interacting system where kinetic energy can be calculated exactly, then add a local external potential  $V_{KS}(\vec{r})$ . The  $F[n]$  decomposes into the following, where  $E_{XC}[n]$  is the exchange-correlation (XC) energy:

$$F[n] = T_s[n] + E_H[n] + E_{XC}[n], \quad (2.6)$$

where  $T_s[n]$  is the non-interacting kinetic energy functional, and  $E_H[n]$  is the Hartree energy functional:

$$E_H[n] = \frac{1}{2} \int d^3r \int d^3r' \frac{n(\vec{r})n(\vec{r}')}{|\vec{r} - \vec{r}'|}. \quad (2.7)$$

Apart from the last term,  $E_{XC}[n]$ , everything else can be exactly calculated for a non-interacting system for given density. By imposing a normalisation constraint on the electron density,  $\int n(\vec{r})d\vec{r} = N$ , we have

$$\frac{\delta F[n]}{\delta n(\vec{r})} = -v(\vec{r}). \quad (2.8)$$

Therefore, the effective local potential  $V_{KS}(\vec{r})$  will be

$$V_{KS}(\vec{r}) = v(\vec{r}) + \frac{\delta E_H[n]}{\delta n(\vec{r})} + \frac{\delta E_{XC}[n]}{\delta n(\vec{r})}, \quad (2.9)$$

and the Kohn-Sham equation reads

$$\left[ -\frac{1}{2} \nabla_i^2 + v(\vec{r}) + \frac{\delta E_H[n]}{\delta n(\vec{r})} + \frac{\delta E_{XC}[n]}{\delta n(\vec{r})} \right] \psi_\alpha(\vec{r}\sigma) = \epsilon_\alpha \psi_\alpha(\vec{r}\sigma), \quad (2.10)$$

and ground-state density is

$$n(\vec{r}) = \sum_{\alpha}^{\text{occ.}} \sum_{\sigma} |\psi_\alpha(\vec{r}\sigma)|^2. \quad (2.11)$$

This can be solved self-consistently. An initial guess of the density  $n(\vec{r})$  determines the effective potential  $V_{KS}(\vec{r})$ , then the wave functions  $\psi_\alpha(\vec{r}\sigma)$  can be calculated from equation (2.10), a new density is calculated through equation (2.11). This procedure is repeated until self-consistency is reached.

## 2.1.2 Exchange-correlation functional

The XC energy functional is not known exactly and therefore needs to be approximated. The choice of it directly influences the accuracy of the results. This is because, although it is often a small fraction of the total energy, its contribution to the chemical bonding and the formation energy is relatively important.

For the XC approximation, the generalized gradient approximation (GGA) has become popular in solid state calculations. It is a further upgrade of its previous version, the local density approximation (LDA). The LDA has the following form:

$$E_{XC}^{LDA}[n] = \int n(\vec{r}) \epsilon_{XC}[n(\vec{r})] d\vec{r}. \quad (2.12)$$

$\epsilon_{XC}[n(\vec{r})]$  is the XC energy for an homogeneous electron gas having density  $n$ , and it is usually taken from quantum Monte Carlo calculations. Whereas the GGA further includes the derivative of density,  $\nabla n(\vec{r})$ , as an argument for  $\epsilon_{XC}$ , thus it reads

$$E_{XC}^{GGA}[n] = \int \epsilon_{XC}[n(\vec{r}), \nabla n(\vec{r})] d\vec{r}. \quad (2.13)$$

In contrast to LDA, there is no unique input for  $\epsilon_{XC}[n(\vec{r}), \nabla n(\vec{r})]$ . Different constructions for GGA usually named with the corresponding authors, e.g. PW91-GGA stands for Perdew and Wang's GGA construction in 1991[95, 96] and PBE-GGA stands for Perdew *et al.* [97]'s construction. They are the most popular GGA approximations for solid state systems.

### Jacob's ladder

Jacob's ladder is a ladder connecting earth and heaven that biblical Patriarch Jacob dreamed about. Professor John P. Perdew, who is known for profound contribution to DFT and XC functionals, used it analogously to describe the hierarchy of density functional approximations in terms of their accuracies, see Fig. 2.2. Each rung is a level of approximation constructed with different formalisms. From LDA and GGA as mentioned before to meta-GGA which includes the Kohn-Sham kinetic energy density. Next method higher in the ladder is the hybrid functionals which incorporates a part of the exact exchange from Hartree-Fock (HF) theory. For example, the PBE0 functional[99] has the following definition:

$$E_{XC}^{PBE0} = \frac{1}{4} E_X^{HF} + \frac{3}{4} E_X^{PBE} + E_C^{PBE}, \quad (2.14)$$

and the HSE06 (Heyd-Scuseria-Ernzerhof)[100] takes into account the screened Coulomb potential for the exact part:

$$E_{XC}^{HSE} = \beta E_X^{HF,SR}(\omega) + (1 - \beta) E_X^{PBE,SR}(\omega) + E_X^{PBE,LR}(\omega) + E_C^{PBE}, \quad (2.15)$$

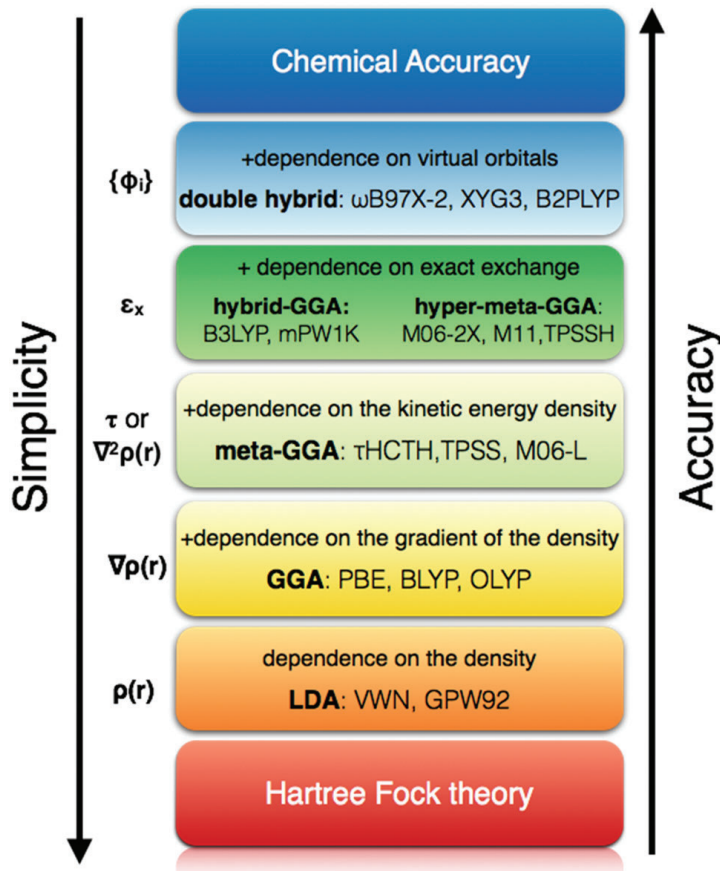


Fig. 2.2 Jacob's ladder for DFT approximations. Image source: Ref. [98]

where  $\beta$  is the mixing parameter and  $\omega$  is the parameter to control the screening range which defines the short-range, SR, and long-range, LR, parts. The values of  $\beta = 1/4$  and  $\omega = 0.2$  corresponding to HSE06 functional which gives accurate band gaps and lattice constants, see the mean absolute error (MAE) of different functionals in Fig. 2.3. The highest ranked functional is the double hybrid which in-

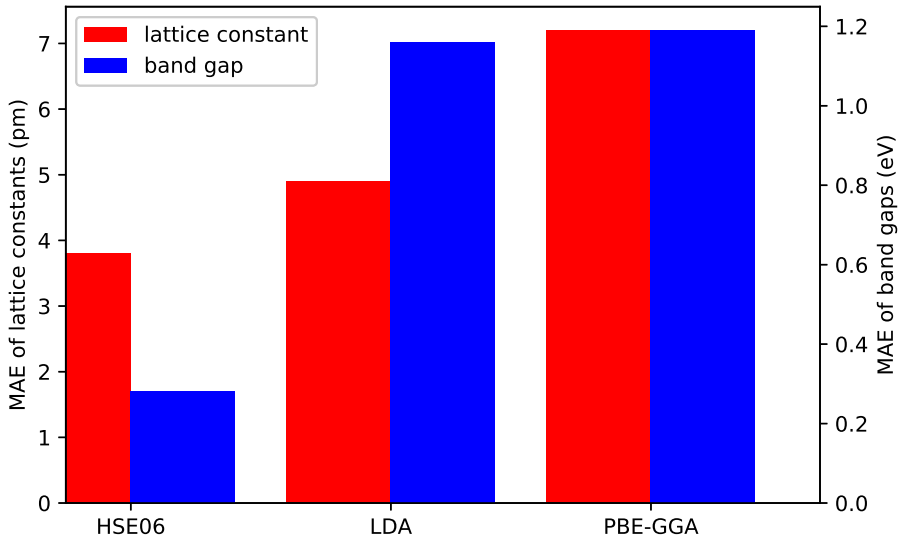


Fig. 2.3 MAE of the equilibrium lattice constants and band gaps of different functionals on SC40 solid test set<sup>1</sup>. Data source: [101]

cludes the unoccupied orbitals as well, e.g. Random Phase Approximation[102].

### Band gap problem

As shown in Fig. 2.3, band gap estimated in LDA and GGA is quite poor. This can be attributed to the highly non-analytical and non-local behaviours of the XC energy functional. To understand this, let's look at the definition of the band gap  $E_g$ :

$$E_g = I - A = \varepsilon_{N+1}^{KS,HOMO} - \varepsilon_N^{KS,HOMO}, \quad (2.16)$$

where  $I$  is the ionization energy, which is the energy change by removing one valence electron.  $A$  is the electron affinity, which is the energy change by adding

---

<sup>1</sup>The SC40 test set is a collections of 40 elementary and binary solid compounds of various structures with a wide range of band gaps

one electron to a neutral system.  $\varepsilon_N^{KS}$  is the Kohn-Sham orbital energy for N-electron system. *HOMO* and *LUMO* stand for the highest and the lowest occupied molecular orbital, respectively. For a non-interacting Kohn-Sham system,  $E_g^{KS}$  can be calculated as follows:

$$E_g^{KS} = \varepsilon_N^{KS,LUMO} - \varepsilon_N^{KS,HOMO}. \quad (2.17)$$

This leads to

$$E_g = E_g^{KS} + \Delta_{XC}, \quad (2.18)$$

where  $\Delta_{XC}$  is the orbital shift caused by adding an extra electron:  $\varepsilon_{N+1}^{KS,HOMO} - \varepsilon_N^{KS,LUMO}$ . The  $\Delta_{XC}$  exclusively depends on the non-analyticity of the XC po-

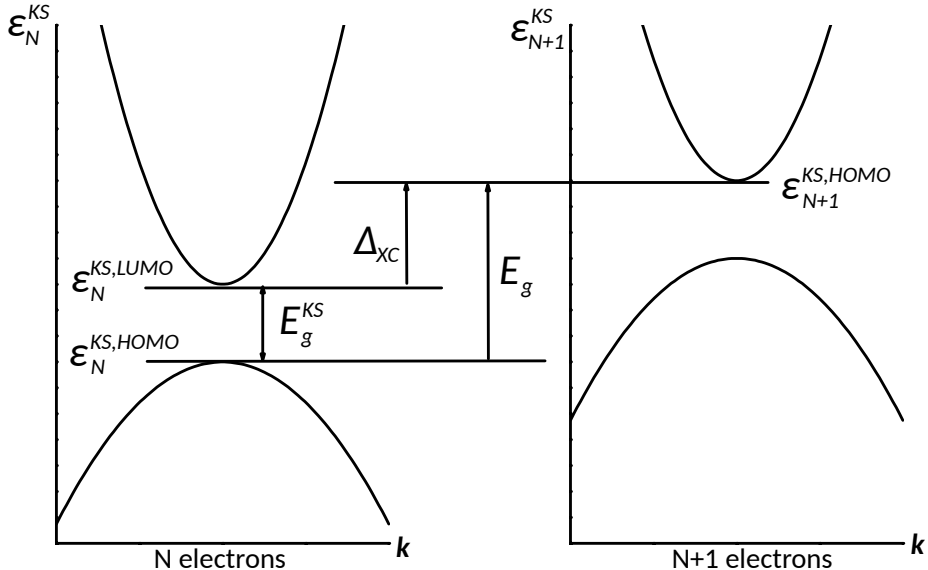


Fig. 2.4 Schematic illustration of the relation between  $E_g$  and  $E_g^{KS}$ . Image is adapted from Ref. [103].

tential  $\frac{\delta E_{XC}[n]}{\delta n(r)}$ , since the Hartree potential explicitly depends on the density. In other words, it means the energy increase by adding an extra electron in the extended system is of the order of 1 eV, even though, it is an infinitesimal density change. If the XC energy functional were analytic, the infinitesimal density variation would not introduce a large potential change, hence  $\Delta_{XC}$  is small or equals to zero, and  $E_g \approx E_g^{KS}$ . The accuracy of the band gap, when compared to experiment measurement, would be only limited by the error that is inherent

to different functionals. However,  $\Delta_{XC}$  usually is not zero and it is responsible for the 80% of the LDA band gap error[104].

## 2.2 Implementation

The implementations of the theory in the last section are crucial and not always straightforward. Many of the quantities are represented with technically easily-implemented functions, and they have to be finite in size or quantity. A question will rise on how large the size or the resolution has to be. This is equivalent to the computational convergence. Here we review two of the most important convergence parameters:  $\mathbf{k}$  points and cut-off energy of the basis set.

### **k** points

According to Bloch's theorem, the solution of the Schrödinger equation for a periodic system, e.g. a crystal with a well-defined unit cell, can be expressed through the following:

$$\phi_{\mathbf{k}}(\mathbf{r}) = e^{i\mathbf{k}\cdot\mathbf{r}} u_{\mathbf{k}}(\mathbf{r}), \quad (2.19)$$

where  $\phi$  is the wave function,  $u$  is a function having the same periodicity as the crystal. The vector  $\mathbf{r}$  and  $\mathbf{k}$  are associated with the real and the reciprocal space ( $\mathbf{k}$  space), respectively. Particularly, each point in  $\mathbf{k}$  space is associated with a unique  $\mathbf{k}$  vector and is usually called a  $\mathbf{k}$  point. Making use of the symmetry of the system, all inequivalent  $\mathbf{k}$  points are contained inside a finite subspace of  $\mathbf{k}$  space, called the first Brillouin zone (FBZ). Quantity evaluations are mostly done through the integration of wave functions, or other functions having  $\mathbf{k}$  dependence, over the FBZ. This integration has to be done numerically since the explicit relation of  $\phi$  and  $\mathbf{k}$  is unknown. In practice, the FBZ is discretized into a grid defined by the mesh of the  $\mathbf{k}$ -points. This mesh has to be large enough for the accurate sampling of FBZ, yet it should be small enough to reduce the computational time and resource. This is one of the convergence tests that need to be done in order to obtain reliable results. Usually, metals need more  $\mathbf{k}$ -points than semiconductors. This is because the highest occupied valence band crosses the Fermi energy in metals, hence the integration for all occupied states is done for a discontinuous function that excludes unoccupied states. Whereas for a semicon-

ductor or insulator, the highest occupied valence band is completely occupied, therefore the integration is for a continuous function. Smearing is one of the ways to transform a discontinuous function in metal into a continuous one by smearing out the edge using a smearing function, such as Fermi-Dirac function. The range of smearing has to compromise between the computation efficiency and correctness: Too large will give wrong integration results of the total energy, while too small become useless therefore one again needs more k-points.

### Basis set, cut-off energy

Now let us look back at equation (2.19). There we can identify  $e^{i\mathbf{k}\cdot\mathbf{r}}$  as a plane wave,  $u_{\mathbf{k}}(\mathbf{r})$  is periodic in space and it can be expanded in terms of a set of plane waves as well:

$$u_{\mathbf{k}}(\mathbf{r}) = \sum_{\mathbf{G}} c_{\mathbf{G}} e^{i\mathbf{G}\cdot\mathbf{r}}, \quad (2.20)$$

where  $c_{\mathbf{G}}$  is the coefficient that determines the magnitude of the plane wave  $e^{i\mathbf{G}\cdot\mathbf{r}}$ . equation (2.19) can now exclusively be represented with plane waves:

$$\phi_{\mathbf{k}}(\mathbf{r}) = \sum_{\mathbf{G}} c_{\mathbf{k}+\mathbf{G}} e^{i\mathbf{k}+\mathbf{G}\cdot\mathbf{r}}. \quad (2.21)$$

The summation in the above equation, for practical reasons, has to be truncated. The truncation is usually done for the kinetic energy:

$$E = \frac{1}{2} |\mathbf{k} + \mathbf{G}|^2. \quad (2.22)$$

The maximum kinetic energy,  $E_{cut}$ , is associated with a  $\mathbf{G}$  vector and define the limit the summations. Here we arrived at another convergence parameter: the plane wave cut-off energy. Similar to the  $\mathbf{k}$  points, it has to be large enough for the total energy to be converged in an acceptable precision range. While too large will cost more computational resources without additional benefits.

### Pseudopotentials and projected augmented-wave method

Considering the chemical inertness of the core electrons and their highly oscillating wave functions, their impact on the valence electrons is generally approximated by pseudopotentials in order to optimize the computational efficiency.

It is a smooth function and has the ability to reconstruct the original core electron properties. Transferability of a pseudopotential is one of the most important factors that determine the performance of the potentials. In practice, a pseudopotential is usually constructed for one isolated atom of one element, while being used in complex multi-elements system, the potentials with higher transferability can simulate what a real atom will react to these different environments. Ultrasoft [105] and projected augmented-wave (PAW) [106, 107] are two types of the most popular pseudopotentials-based methods used in materials simulations. They are well-balanced between accuracy and computational cost. In this thesis, the PAW method is exclusively used for all calculations. This method combines the ideas of pseudopotentials method and all-electron methods. Same as in the case of pseudopotential, in PAW, the true wave function  $|\Psi_n\rangle$  that are obtained from all-electron methods can be transformed into a smooth auxiliary function  $|\tilde{\Psi}_n\rangle$  by a linear transformation operator  $\mathcal{T}$ . The partial waves  $|\phi_i\rangle$  is the complete basis set that expands the wave function and it can be also related to auxiliary partial waves  $|\tilde{\phi}_i\rangle$ :

$$|\phi_i\rangle = \mathcal{T} |\tilde{\phi}_i\rangle, \quad (2.23)$$

where  $i$  is a complete set of quantum numbers. The true and the auxiliary wave functions are identical outside the cur-off radius  $r_c$ :

$$\phi_i(\mathbf{r}) = \tilde{\phi}_i(\mathbf{r}), \text{ for } |\mathbf{r} - \mathbf{R}| > r_c, \quad (2.24)$$

where  $\mathbf{R}$  is the position of the atom. The transformation operator  $\mathcal{T}$  takes the following form:

$$\mathcal{T} = 1 + \sum_i (|\phi_i\rangle - |\tilde{\phi}_i\rangle) \langle \tilde{\rho}_i |, \quad (2.25)$$

where  $\tilde{\rho}_i$  is the projector functions that capture the character of true wave function within a radius of  $r_c$ . Now the all-electron wave functions can be reconstructed through the smooth auxiliary functions and projector functions :

$$|\Psi_n\rangle = |\tilde{\Psi}_n\rangle + \sum_i (|\phi_i\rangle - |\tilde{\phi}_i\rangle) \langle \tilde{\rho}_i | \tilde{\Psi}_n \rangle. \quad (2.26)$$

The PAW method expresses the true all-electron wave functions with smooth functions that can be easily implemented and perform more efficiently as compared to the all-electron wave functions, moreover the accuracy of the calculations are comparable to that for the all-electron ones.

### 2.2.1 Software Packages

There are more than 70 different software packages capable of performing density functional theory calculations according to Wikipedia[108]. They mainly differ in the type of pseudopotentials if there is any, the type of basis set is used to expand the wave function, in which programming language it is written and whether or not it is free or commercial etc. Lejaeghere *et al.* [109] have compared 40 different implementations and their accuracy by comparing their results to a highly accurate all-electron method. They concluded that all codes or methods yield generally consistent results. The accuracy of the codes which were developed in the recent years is higher than the earlier ones. The Vienna *Ab initio* Simulation Package (VASP) [110, 111] with its PAW method is one of the most accurate codes those are concluded from this study. Its well-optimized performance on supercomputers gives good results in less time as compared with the others. This code will be used as the main tool for all the calculations done in this thesis.



# **Chapter 3**

## **General physical properties of 2D materials**

In this thesis, the properties of materials are divided into a preliminary and an advanced category, where the latter will be presented in the next chapter as the main results of this thesis. In this chapter, I will focus on the preliminary properties of 2D materials, namely structural, electronic, vibrational and mechanical properties. These properties can be used to test the methodology and form the foundation upon which the advanced properties are calculated. They are composed both of my original calculations and results from literature. An emphasis will be on the characteristic properties of 2D materials that are different from 3D materials.

### **3.1 Structural properties**

#### **3.1.1 Layered structure: from multi- to monolayer**

As discussed in chapter 1, layered bulk materials are closely related to 2D materials. A single layer of a layered bulk material is a 2D material. This anisotropic nature is attributed to the weak interlayer bonds and the strong intralayer bonds. Van der Waals (vdW) interaction [112] is the main source of the weak interlayer bonds. vdW interactions consist of the attraction and the repulsion between atomic or molecular entities caused by dipole-dipole, dipole-induced dipole and instantaneous induced dipole-induced dipole forces. The definition is sometimes

extended to include all dispersion forces between molecules. For 2D materials, the vdW interaction becomes important as the number of layers is larger than one; that is few-layer materials having typically less than ten layers. They also belong to the family of 2D materials since the thickness of the materials is still small and quantum confinement effects are very important. As in its layered bulk counterpart, a few-layer system is a stack of monolayers hold together through vdW forces. When no other bonding types are present, interlayer vdW interaction determines all the change when going from a single layer to multi-layer, and its impact on the electronic structure can be significant. For example, from monolayer to bilayer, the low energy linear dispersion relation of energy  $E$  as a function of  $k$  around the K point evolves into a parabolic-like spectrum[113, 114].

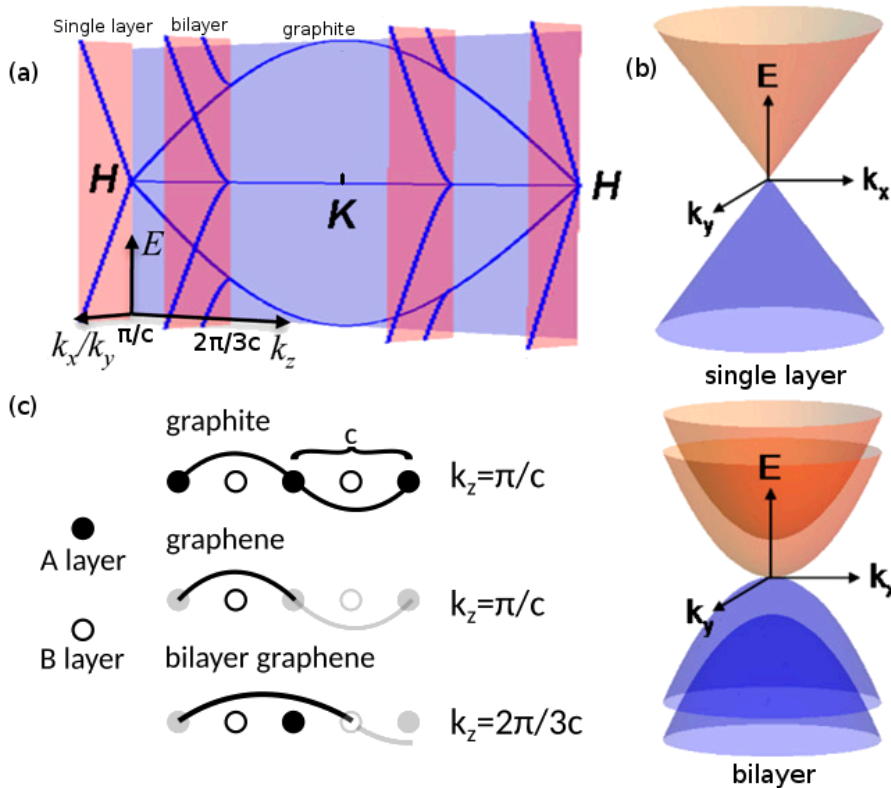


Fig. 3.1 (a) Energy-momentum dispersion relations of single layer and bilayer graphene as approximated by plane intersections of 3D graphite dispersion relation and (b) their 3D dispersion relations around the K point. (c) Matching of the wavelength in graphite to that in single layer and bilayer graphene. Image is adapted from Ref. [114].

In Fig. 3.1 (a), the dispersion relation of graphite along the z direction, that is the HKH line in the Brillouin zone, is shown on the blue plane. This direction is perpendicular to the graphite layers. Because of quantum confinement in a few-layer system, standing waves are presented with a finite number of wave vectors. If only the intralayer and interlayer interactions between the nearest neighbour atoms were considered, the dispersion relation in few-layer graphene can be approximated as those on the cross-section of virtual planes (the red planes in Fig. 3.1 (a)) with the 3D graphite dispersion relation. These planes are perpendicular to the z direction and intersect with the HKH line at limited points. This is called the quantization<sup>1</sup> of dispersion relations[115]. These points are illustrated in Fig. 3.1 (c). Quantum confinement in a few-layer system requires that the wave functions vanish at the imaginary layer right outside the surface of the system, the systems will have well-defined wave vectors. Then, the dispersion relations of graphene and bilayer graphene will be on the red planes that intersect the HKH line at  $k_z = \pi/c$  and at  $k_z = 2(\pi/3c)$ , respectively, where  $c$  is the lattice constant of graphite that is vertical to the graphite plane. Having the knowledge of the 3D band structure of graphite, one can approximate the dispersion relation of few-layer systems in this way. As shown in the red plane in Fig. 3.1 (a) and the 3D version in Fig. 3.1 (b), graphene has a linear dispersion relation and bilayer graphene has two parabolic-like bands. Moreover, the bilayer structure will never pass through the H point where graphene has passed to have a linear dispersion relation. This is because the standing waves in a bilayer will have a wave vector  $k = 2(n\pi/3c)$ , where  $n$  is a positive integer: 1, 2, ..., n. This will never be equal to  $\pi/c$  for any integer number of  $n$ . More generally, systems with an even number of layers will not have a linear dispersion relation, and vice versa for systems that have an odd number of layers. Further, if other interactions were considered, an overlap of those bands touching each other would have occurred[113]. This overlap increases with the number of layers. Eventually, maximum overlap is reached in graphite.

Another example of the importance of interlayer interactions in few-layer 2D materials is seen for MoS<sub>2</sub>. As mentioned in chapter 1, as going from layered bulk to monolayer, MoS<sub>2</sub> transforms from an indirect band gap to a direct one. Here again, we can make use of the quantization scheme to approximate the band

---

<sup>1</sup>Sometimes it is also referred as zone-folding.

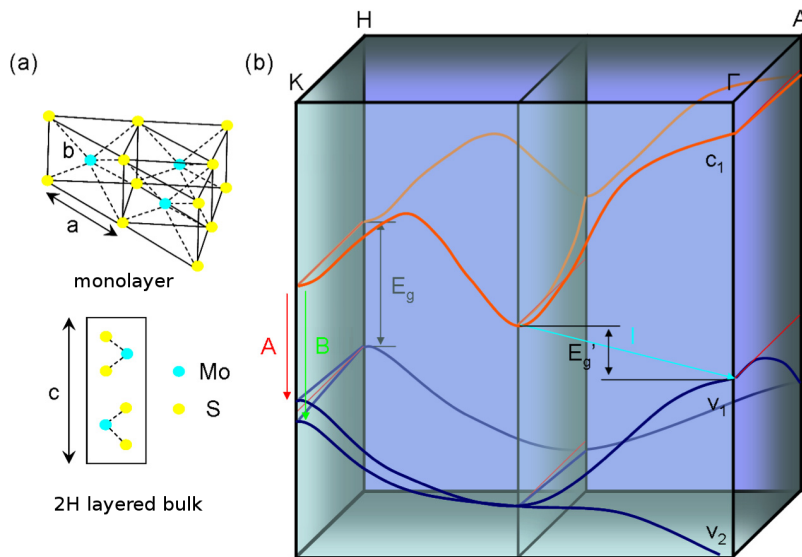


Fig. 3.2 (a) The atomic structures of monolayer and layered bulk MoS<sub>2</sub>. (b) The energy-momentum dispersion relation of monolayer MoS<sub>2</sub> as a plane intersection of the 3D dispersion relation. Image is adapted from Ref. [116].

structure of the monolayer from that of its layered bulk. The monolayer and the layered bulk structure of the 2H phase are shown in Fig. 3.2 (a). In Fig. 3.2 (b), let us focus on the planes parallel to the page that pass through the KΓ line and the HA line (simply call them KΓ plane and HA plane below). Similar to the previously discussed graphite, 2H layered bulk MoS<sub>2</sub> has two layers per unit cell. Therefore, according to the standing wave arguments that we have used for the graphene case above, HA plane represents the monolayer.  $E_g$  and  $E_{lg}$  are the band gaps of the monolayer and the layered bulk structures. Here, not only the magnitude of the band gap is increased as going from layered bulk to monolayer, the character of the band gap has changed as well. It is clearly shown that this is due to the shifting of the band edges. VBM at Γ and CBM at the middle of the KΓ line are brought closer as they go from monolayer to layered bulk. This corresponds to the widening of the band width and it is coming from the splitting of the VB and CB when more and more layers interact with each other through the interlayer interactions. Therefore, the band gap in the layered bulk is defined by these two band edges, which in the monolayer was defined by the band edges at K. In contrast to this, the band edges at the K point are not affected too much by the interlayer interaction. So why do the band edges react differently

to the interlayer interactions? If we look into the orbital composition of the band edges, we will find the ones that have widened the most, i.e. VBM at  $\Gamma$ , have the largest contribution from S  $p_z$  and Mo  $d_{z^2}$  orbitals. These out-of-plane orbitals are orientated vertically to the plane and thus have maximum overlap with the others from an adjacent layer. Therefore, band splitting is more profound for these band edges and causing the increase of their band width. In contrast, both the CBM and VBM at K are largely composed of S  $p_x$  and  $p_y$  orbitals and Mo  $d_{xy}$  and  $d_{x^2-y^2}$  orbitals. All of them are in-plane orientated orbitals and thus have limited effect from the interlayer interaction[117].

### 3.1.2 $sp^n$ hybridization

After discussing layered structures and the importance of interlayer interaction, let us look into some detail of the in-plane structure and how  $sp^n$  hybridization gives rise to various structures for 2D materials, where  $n$  is the hybridization index that will be discuss in the following. When atoms come together to form bonds, the orientation of bonding orbitals are decisive for the final structure. The hybridization of s and p orbitals is a good example of this. It mainly exists in three different variants:  $sp$ ,  $sp^2$  and  $sp^3$ , see Fig. 3.3. The hybridization index  $n$  in  $sp^n$  stands for the relative amount of p character in the resulting hybridized orbital. For example,  $sp^2$  has 1/3 s character and 2/3 p character. Hybridized orbitals tend to maximize their distance to reduce the energy raised by the repulsion of electrons. As shown in Fig. 3.3, this results in tetrahedral structure of  $sp^3$  orbitals, as in diamond, trigonal planar structure of  $sp^2$  orbitals, as in graphene or graphite and linear structure of sp orbitals, as in ethyne molecules. This is, for example, useful to explain the buckled structure of graphane and fluorographene. Because  $sp^3$  character is induced when the fourth electron is bonded with H or F atoms, and as a result buckling appears in these systems.

Coulson & Moffitt [119] generalized the relation of bond angle with  $n$  as follows:

$$1 = -\sqrt{n_1 n_2} \cos\theta_{12}, \quad (3.1)$$

where  $\theta_{12}$  is the bond angle between orbital 1 and 2. If orbital 1 and 2 have different  $n_1$  and  $n_2$ , we still need one more constraint to solve the equation (3.1) for the hybridization indices  $n$ . This constraint is that, in the case of carbon atoms, the

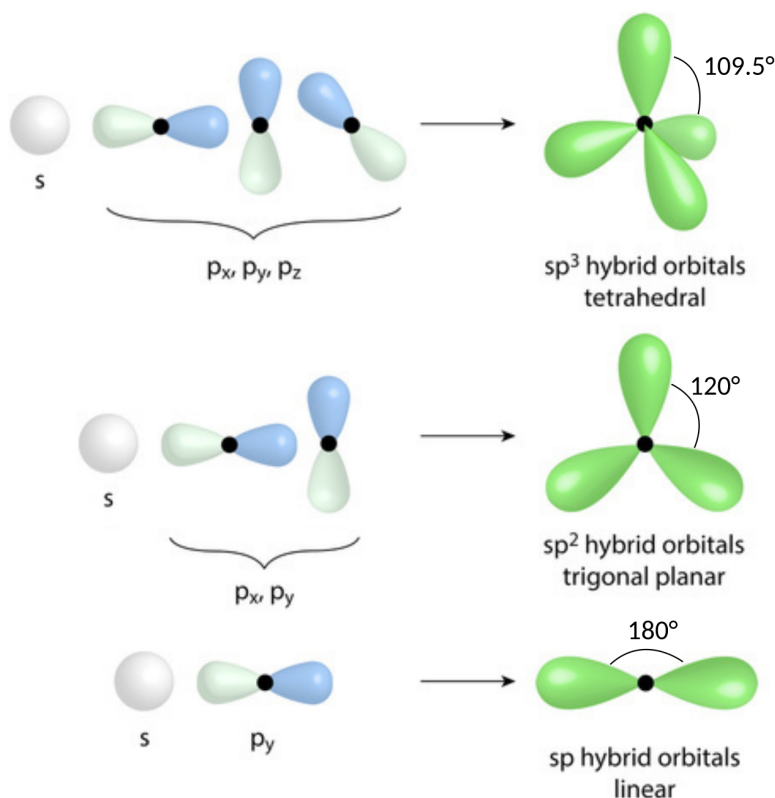


Fig. 3.3 Three types of  $sp$  hybridized orbitals. Image is adapted from Ref. [118].

total portion of  $s$  orbitals should equal to 1, while it should be 3 for the  $p$  orbitals. With these pieces of knowledge, equation (3.1) can be solved, and each orbital from one atom can be assigned with  $n$ . This formula is useful to determine the  $s$  and  $p$  fractions of the bonds. For example,  $\theta_{12} = 90^\circ$  gives  $n \rightarrow \infty$ , which means it is a pure  $p$  orbital;  $\theta_{12} = 120^\circ$  gives  $n = 2$ , that is a  $sp^2$  hybridized orbital. Generally, the wider the bond angle, the larger the  $s$  contribution. Accordingly, bond angles are ordered as  $sp > sp^2 > sp^3$ . Of course, equation (3.1) is more useful when the bond angle takes values other than those three types of hybridized orbitals mentioned, then it can be used to explain the resulting geometry.

## 3.2 Electronic properties

The electronic properties are among the first features we would like to know of new materials, not only because semiconductors and metals play different roles in applications, but also because details of the electronic structure set the direction for further exploration. One example from my experience is that by monitoring electronic structure variations under strain, we can predict how the mobility of the carriers can be tuned. This will be discussed in later chapters. Therefore, it is important to understand this property of a new material to fully reveal its potential. Electronic properties are usually characterized by the band structure (BS) and the density of states (DOS). These calculations are standard calculations in common first-principles codes from where all subsequent calculations start. After solving the Kohn-Sham equation with properly defined cut-off energy,  $k$  points etc., we will have the eigenenergy of each state, indexed by a  $k$  point in the Brillouin zone and a band number. The DOS counts such states at a specific energy. The BS is the plot of the eigenenergies along lines in the Brillouin zone that connect high symmetry  $k$  points. 2D materials have a vast variation of electronic properties, from semimetallic graphene to semiconducting MoS<sub>2</sub> and insulating BN. I will briefly discuss this at the end of this section. The purpose of this section is to point out some of the interesting electronic properties of some 2D materials. We will start with a brief introduction of the electronic properties of graphene.

### 3.2.1 Graphene

As mentioned before, the orbitals of the C atoms in graphene are sp<sup>2</sup> hybridized. Each one of these sp<sup>2</sup> orbitals, coloured in green in Fig. 3.4, is composed of s, p<sub>x</sub> and p<sub>y</sub> orbitals, whereas the p<sub>z</sub> orbital, coloured in yellow in the figure, is left unchanged. One sp<sup>2</sup> hybridized orbital with the one from an adjacent atom forms a strong  $\sigma$  bond, while p<sub>z</sub> orbitals form  $\pi$  bonds. It may look like alternative single and double bonds between atoms, however, according to Clar's theory, the bond order, i.e. the number of chemical bonds between a pair of atoms, in graphene is 4/3 and is uniform[120]. This has to do with the high symmetry of the graphene lattice.

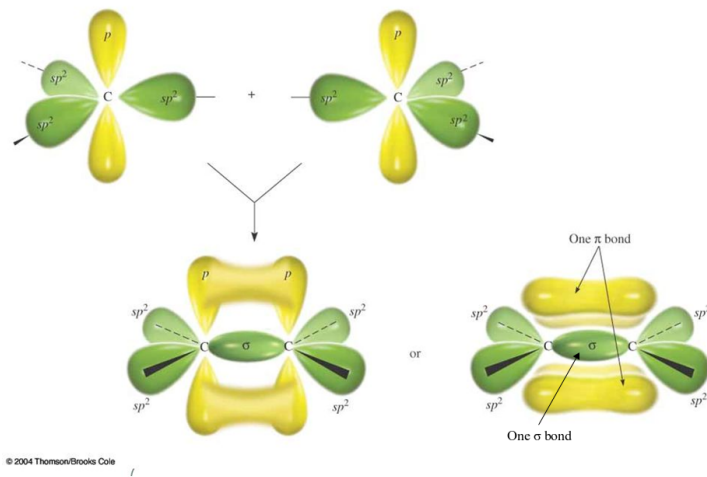


Fig. 3.4 The formation of  $sp^2 \sigma$  and  $p_z \pi$  double bond. Image source: Ref. [121]

Every C atom has the same local environment in graphene. However, adjacent atoms are not equivalent from a symmetry point of view. They belong to different hexagonal sublattices, A and B, as indicated with blue and yellow colors in Fig. 3.5.  $a_1$  and  $a_2$  are the basis vectors in real space connecting equivalent lattice sites. On the left,  $b_1$  and  $b_2$  are the basis vectors in reciprocal space connecting equivalent  $k$  points. The hexagon in reciprocal space is the first Brillouin zone where all inequivalent  $k$  points are contained. These  $k$  points correspond to different parallel lines of atoms and thus their directions in reciprocal space are associated with different directions in real space. The  $k$  wave vectors near the  $\Gamma$  point have longer wave length than those away from it. While those at the boundary of the first Brillouin zone have wave lengths that are twice the unit cell dimension in the direction specified by the  $k$  points. For example, the most interesting  $k$  points for graphene are the K and K' points. These directions correspond to the  $a_1$  and  $a_2$  directions in real space. It is only at these  $k$  points in the Brioulloin zone that the antibonding and the bonding  $\pi$  bands touch each other.

In contrast to  $\pi$  bonds, the  $\sigma$  bonds originate from a strong overlap of  $sp^2$  orbitals. The interaction is so strong that the splitting of bonding and antibonding orbitals is large. This makes the  $\sigma$  bonding orbitals having large negative energies, or in other words, makes the  $\sigma$  bond strong and difficult to break. This fea-

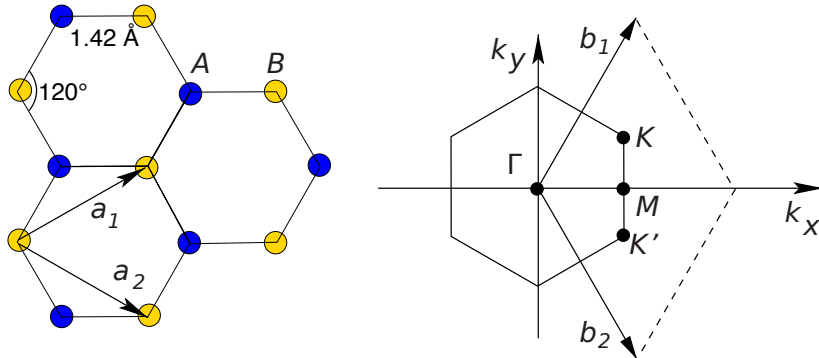


Fig. 3.5 Graphene lattice and its Brillouin zone. Image source: Ref. [14]

ture contributes the most to the mechanical strength of graphene. On the other hand,  $p_z$  orbitals are less overlapping. This makes the  $\pi$  bond energy close to the Fermi level, i.e. the highest occupied state. Therefore, they contribute the most to the electronic properties of graphene.

### 3.2.2 Dirac cone and symmetry

We have seen that graphene, silicene and germanene have an interesting electronic structure: forming Dirac cones. We also have listed the consequences of having such a feature: high mobility, massless carriers etc. In this section, we will discuss the symmetry condition for the existence of Dirac cones. This knowledge can be used to discover more materials exhibiting a Dirac cone. According

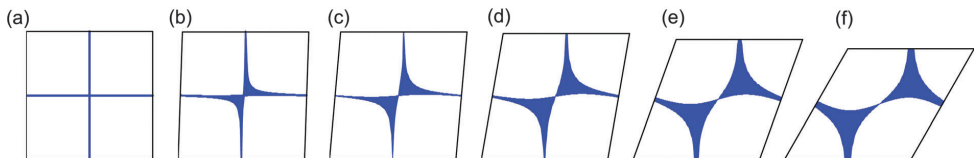


Fig. 3.6 Possible positions for the second atom (blue area) in order to guarantee the existence of Dirac cones as going from (a) square lattice to (f) hexagonal lattice. The first atom is located at the corners of the unit cell. Image source: Ref. [122]

to the von Neumann-Wigner theorem<sup>2</sup>, the space-time inversion symmetry is crucial for the existence and protection of Dirac cones[123]. It is a combination

<sup>2</sup>This theorem describes the probability of a finite-dimensional matrix to have degenerated eigenvalues.

of space inversion and time reversal symmetries. These two are equally important and have to act simultaneously for the possible formation of Dirac cones. A more restrictive condition that guarantees the existence of Dirac cones has to deal with relations of hopping integrals[122, 124]. A study by Liu *et al.* [122] revealed that the hexagonal lattice has the most favourable structure to form Dirac cones. The probability decreases as one goes from a hexagonal lattice to a square lattice, as shown in Fig. 3.6. Therefore, since most of the 2D materials have hexagonal symmetry, there will be a higher chance of finding materials with Dirac cones in this category.

### 3.2.3 Examples: 2D-h-BN, 2D-MoS<sub>2</sub> and graphene

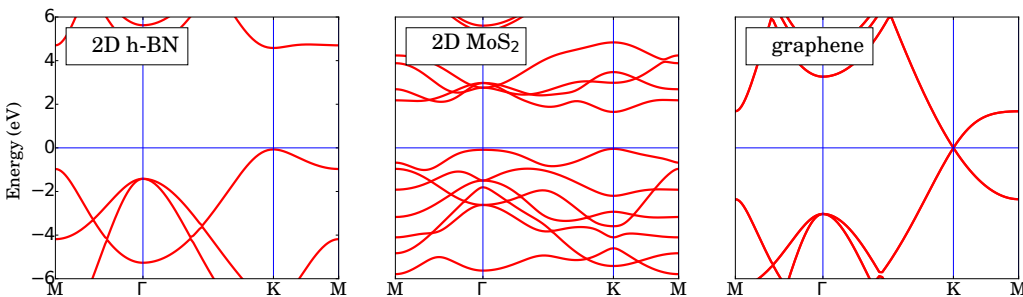


Fig. 3.7 Electronic band structures of 2D-hBN, 2D-MoS<sub>2</sub> and graphene calculated with PBE-GGA functional.

Three typical examples of the band structure of 2D materials are shown in Fig. 3.7. The 2D h-BN is an insulator due to a large band gap in the ultraviolet range, therefore it is suitable to serve as a dielectric layer in an electronic device. The 2D TMDs have a band gap ranging from 1.0-2.5 eV which is in the visible and the near infrared range of light, therefore, they are suitable for optoelectronic device applications. Furthermore, as we compare the dispersion curves along the M $\Gamma$  and K $\Gamma$  directions, we can see that the electronic structure is generally the same along these paths which correspond to different crystallographic directions. This means that these materials are highly isotropic, thus we would expect the same for their physical properties. In the result chapters of this thesis, we will investigate some new 2D materials that are highly anisotropic. Their discoveries enrich the features of the physical properties of 2D materials.

### 3.3 Vibrational properties

The vibrational properties form an important aspect of materials, especially at finite temperature. Thermal expansion, thermal conductivity and electron mobility are all vibrational related topics. Therefore, it is crucial to understand the characterization of this in computational modelling. The force  $\vec{F}_I$  on the atom  $I$  at the position  $\vec{R}$  can be calculated from the wave functions  $\Psi_0$  evaluated from DFT thanks to the Hellmann-Feynman theorem as showing in the following:

$$-\vec{F}_I = \langle \Psi_0(\vec{R}) | \nabla_I H(\vec{R}) | \Psi_0(\vec{R}) \rangle. \quad (3.2)$$

When searching for the equilibrium geometry of the materials, one basically tries different positions of atoms to find a geometry that minimizes all the forces. This usually is the first thing to do for new materials, since different codes, implementations and, more importantly, different functionals will give different results. Despite the fact that the difference is usually small, an unrelaxed geometry will have residual forces on the atoms. This is particularly important when vibrational properties are concerned. Vibrational properties are characterized through the energy (usually expressed in terms of frequency) versus vibrational wave vector dispersion relation. In crystals, all atoms vibrate around their equilibrium positions. The vibrational modes are quantized into phonons. Each phonon represents a periodic, collective vibration with a well-defined vibrational mode and wave vector. The forces ( $F$ ) that restore the atoms when they deviate from their equilibrium positions can be calculated from DFT either by introducing small displacements or from perturbation theory. Then, the force constants,  $\Phi$ , can be constructed by monitoring the change in forces through the displacements,  $u$ , of atoms in the following way:

$$\Phi_{i\alpha,j\beta} = \frac{\partial F_{j\beta}}{\partial u_{i\alpha}}, \quad (3.3)$$

where the  $i, j$  indices are the labels for atoms,  $\alpha, \beta$  are the Cartesian directions:  $x, y$  and  $z$ . The Fourier transformation of the force constants at wave vector  $\mathbf{q}$  is the dynamical matrix  $D(\mathbf{q})$  that is related to the frequency of the phonon through the eigenvalue problem:

$$\omega^2(\mathbf{q}, n)\mathbf{e}(\mathbf{q}, n) = D(\mathbf{q})\mathbf{e}(\mathbf{q}, n), \quad (3.4)$$

where  $\omega(\mathbf{q}, n)$  is the frequency of the phonon in mode  $n$  having wave vector  $\mathbf{q}$ , and  $\mathbf{e}(\mathbf{q}, n)$  is the corresponding eigenvector[125, 126]. Depending on whether atoms in the unit cell are vibrating in-phase or out-of-phase, phonon modes are categorized into acoustic and optical, respectively. For polar materials, charged atoms that vibrate with respect to each other can interact with light, which is the reason that these types of vibrations are called optical modes. Further, considering the respective directions of the wave ( $\mathbf{e}$ ) and vibration ( $\mathbf{q}$ ), the modes are subcategorized into transverse optical (TO) modes and transvers acoustic (TA) modes, where  $\mathbf{q} \perp \mathbf{e}$ , and longitudinal optical (LO) and longitudinal acoustic (LA) modes, where  $\mathbf{q} \parallel \mathbf{e}$ . These modes are all in-plane vibrations for 2D materials. For 2D materials, another direction is different from those in-plane ones, namely the  $\mathbf{c}$  lattice vector direction perpendicular to the 2D plane. Special modes exist: out-of-plane transverse optical (ZO) and out-of-plane transverse acoustic (ZA) ( $\mathbf{q} \perp \mathbf{e}$  and  $\mathbf{q} \parallel c$ ). The total number of acoustic modes is three, that of optical modes is  $3N-3$ , where  $N$  is the total number of atoms in the unit cell.

### 3.3.1 Example: 2D-MoS<sub>2</sub>

Let us now take layered bulk and monolayer MoS<sub>2</sub> as examples to highlight some of the important details of phonon dispersion relations. A comparison of vibrational modes between layered bulk and monolayer MoS<sub>2</sub> is presented in Fig. 3.8 (a). First of all, the number of atoms in the unit cell reduces from six to three from layered bulk to monolayer. Therefore, the number of optical modes will be reduced as well from 15 in layered bulk to six in the monolayer. In Fig. 3.8 (a) it is shown, as the material is transformed to the monolayer, that several modes merge with others that only differ by whether the vibration in different layers is in-phase or out-of-phase. Secondly, a characteristic feature of phonon dispersions for layered bulk and 2D materials has appeared, namely the quadratic ZA mode (flexural mode). It is usually linear in 3D bulk materials because of strong interlayer interactions. Because in layered bulk, the interlayer interactions are weak and absent in 2D materials, therefore, it will cost less energy

for the out-of-plane vibration and a quadratic dispersion will appear[127]. This feature is closely related to the formation of the intrinsic ripples in 2D materials, e.g. graphene[128] and MoS<sub>2</sub>[129]. As shown in Fig. 3.8 (b), phonons with longer wave lengths, i.e. around  $\Gamma$ , in ZA mode have smaller frequencies or energies. This means this mode is more easily excited at low temperature and forms ripples which can be often observed in 2D materials. The formation of ripples is crucial for the stability of 2D materials at finite temperature. Lastly, in the projected DOS, the projections of mode eigenvectors to in-plane (XY) and out-of-plane (Z) components are shown. The modes with Z components, i.e. ZO<sub>1</sub>, ZO<sub>2</sub> and ZA, contribute the most to the Z projections, and vice versa for the longitudinal and acoustic modes to the XY projection.

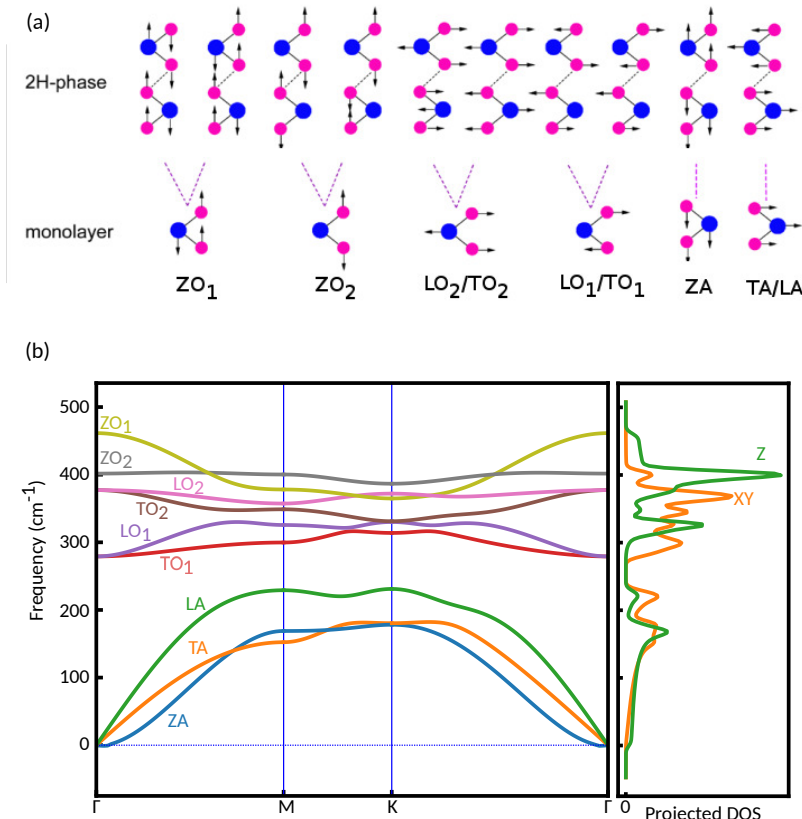


Fig. 3.8 (a) Phonon modes of layered bulk (first row) and monolayer (second row) MoS<sub>2</sub> at the  $\Gamma$  point. (b) Phonon dispersion and projected DOS of monolayer MoS<sub>2</sub>.

### 3.3.2 Dynamic stability from phonon dispersion

One of the most useful features of the phonon dispersion is the possibility to check the dynamical stability of the structure. An unstable structure is usually indicated by the presence of imaginary frequencies in the phonon spectrum in some part of the Brillouin zone, see Fig. 3.9 for example.

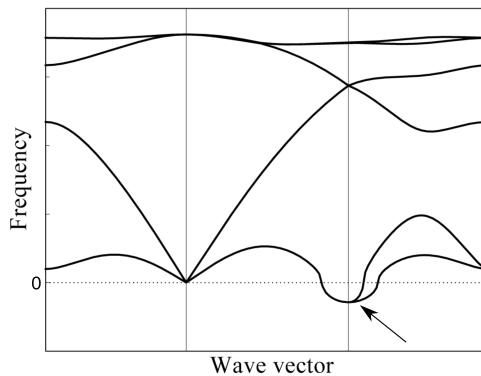


Fig. 3.9 Imaginary frequencies are shown as negative frequencies in a phonon dispersion plot.

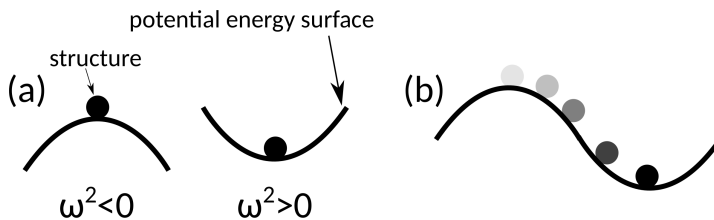


Fig. 3.10 (a) A structure at the convex (left) and the concave (right) of the PES. (b) Searching for a stable structure (phase transition).

Now let us try to understand this and make use of it to convert an unstable to a stable structure. Consider a relaxed structure in which the forces on all atoms have vanished. This could be locally at the maximum or the minimum of the potential energy surface (PES), see Fig. 3.10. Note that, in both situations, the forces, the derivative of the PES curves, are zero. Therefore, both situations can occur when the structure is relaxed by only following the forces. In the case of a convex PES, the dynamical matrix  $D(\mathbf{q})$  will have negative components because the direction of the force is the same as the displacement. We have seen from equation (3.4) that  $D(\mathbf{q})$  is related to the square of the frequency  $\omega$ , hence

imaginary frequencies are the only solutions. However, a structure with imaginary frequencies near  $\Gamma$  point does not necessarily mean it is not stable. Since a large supercell consisting of multiples of the unit cell is typically used to do phonon calculations, it may be that the size of the supercell is not large enough to correctly describe long wavelength phonons. In contrast to this, a structure with imaginary frequencies that appear around other  $q$  points than the  $\Gamma$  point would imply a structure instability or a structural phase transition. The lowering of the energy with some vibrational modes means that the structure prefers a modulation as induced by the vibration, therefore if we calculate the energy of the modulated structure we will have a lower energy structure. With advanced techniques in phonon software[e.g. 130], it is possible to perturb such a structure based on the vibration mode which has an imaginary frequency to find a lower energy state and stabilize the structure, as schematically illustrated in Fig. 3.10 (b).

## 3.4 Mechanical properties

In chapter 1, we have discussed the stiffness and strength of some of the 2D materials. These are some of the mechanical properties of materials. The force on the atoms or the stress  $\sigma$  on the the unit cells under a finite strain  $\epsilon$  are typical outputs from common first-principles codes. Within the elastic regime of the stress-strain relation, they can be related through the elastic constant  $C$ :  $\sigma = C\epsilon$ , this is Hook's law.  $C$  is a  $6 \times 6$  matrix with matrix elements  $C_{ij}$ . The elements measure the resistance of a material in the  $i$  direction to a deformation in the  $j$  direction, where  $i$  and  $j$  are the index of stress and strain tensors, respectively. With the Voigt notations, the indices have the following correspondence: 1→xx, 2→yy, 3→zz, 4→yz, 5→zx, 6→xy. The elastic constants can be simplified if the crystal symmetry and dimension are taken into account. For example, for 2D hexagonal lattice symmetry, Hook's law reads:

$$\begin{pmatrix} \sigma_1 \\ \sigma_2 \\ \sigma_6 \end{pmatrix} = \begin{pmatrix} C_{11} & C_{12} & 0 \\ C_{12} & C_{11} & 0 \\ 0 & 0 & (C_{11} - C_{12})/2 \end{pmatrix} \begin{pmatrix} \epsilon_1 \\ \epsilon_2 \\ \epsilon_6 \end{pmatrix}. \quad (3.5)$$

In this way, all elastic constants can be extracted from stress-strain data using first-principles calculations. Generally, it is more convenient to have a single quantity to describe a particular aspect of the mechanical properties of the material. This is where the Young's modulus  $Y$ , shear modulus  $G$  and Poisson's ratio  $\nu$  become useful. Following previous notations, they are defined as

$$Y_\alpha = \frac{1}{S_{\alpha\alpha}}, \quad \alpha = 1, 2, 3 . \quad (3.6)$$

$$\nu_{\alpha\beta} = -Y_\beta S_{\alpha\beta}, \quad \alpha, \beta = 1, 2, 3 \quad (\alpha \neq \beta) . \quad (3.7)$$

$$G_{\gamma\gamma} = \frac{1}{S_{\gamma\gamma}}, \quad \gamma = 4, 5, 6 , \quad (3.8)$$

where  $\mathbf{S} = \mathbf{C}^{-1}$  is the compliance matrix [e.g. 131]. The Young's modulus and shear modulus give the stiffness of the material when it responds to a stretching and shearing deformation in particular directions and they stand for the hardness of the material. Their unit in 2D is  $J/m^2$  or  $N/m$ . To make them comparable with conventional 3D materials, 2D moduli usually are converted into 3D ones by dividing the former by the thickness of the sheet. Poisson's ratio gives the ratio of the transverse to the axial strain. It represents how easy it is to change the shape of the material with respect to changing the volume. Liquid and rubber have a Poisson's ratio close to 0.5, which is the theoretical upper limit of this quantity and making them the easiest materials to change shape over volume. In contrast, a cork has a Poisson's ratio close to zero, meaning zero lateral expansion when compressed in other directions. The breaking strength/strain is a measure of the maximum load limit that a material can withstand and it is used to characterize the strength of a material. This quantity is usually obtained by continuously deforming the material until they break and recording the maximum stress/strain. This can be done both experimentally and through simulations.

### 3.4.1 Examples: graphene, 2D-BN and 2D-MoS<sub>2</sub>

In table 3.1, the mechanical properties of several 2D materials are listed, as well as that of steel for comparison. As mentioned, graphene is the strongest ma-

terial ever measured. This is due to its strong  $\sigma$  bonding. With similar bonding in BN, it shows comparable results to graphene. MoS<sub>2</sub> has lower stiffness and strength than the previous two due to weaker bonding, nevertheless, it is still much stronger than steel. The Poisson's ratio has an inverse relation with Young's modulus. This means graphene acts more like cork than rubber as compared to MoS<sub>2</sub>.

Table 3.1 Mechanical properties of graphene, BN and MoS<sub>2</sub>

material	Young's modulus TPa	Breaking strength GPa	Poisson's ratio
graphene[23]	1.0±0.1	130±10	0.149[132]
2D-BN [133]	0.71–0.97	120–165	0.210
2D-MoS <sub>2</sub> [134]	0.27± 0.10	23	0.29 [135]
A36 steel[136]	0.2	0.4–0.55	0.26

### 3.4.2 Mechanical stability: Born stability criteria

Mechanical stability is a criterion for unstressed crystal stability, which is additional to dynamical stability. It was first pointed out by Born [137] in the 1940's., and is therefore often called "Born stability criteria". Its core concept is that the elastic energy should be positive for any non-zero strains. The elastic energy  $U$  is related to the elastic constants  $C_{ij}$  in the following way:

$$U = U_0 + \frac{1}{2} V_0 \sum_{i,j=1}^6 C_{ij} \epsilon_i \epsilon_j, \quad (3.9)$$

where  $U_0$  is the equilibrium energy and  $V_0$  is equilibrium volume. According to Born's paper[137], the necessary and sufficient stability conditions are: 1)  $|\mathbf{C}| > 0$ ; 2) all eigenvalues of  $\mathbf{C}$  are positive; 3) Sylvester's criterion: the determinants of the upper-left  $k$  by  $k$  sub-matrices are positive; (4) an arbitrary set of minors of  $\mathbf{C}$  are positive. Mouhat & Coudert [138] formulated closed form expressions of this criteria for different crystal systems. Taking into account the symmetry of these systems, the number of criteria reduces, and becomes very useful to check the mechanical stability of a new crystal system. For example, for a 2D hexagonal crystal, the criteria become:

$$C_{11} > |C_{22}|, C_{66} > 0. \quad (3.10)$$

# **Chapter 4**

## **Results of Physical Properties Calculations in Novel 2D Materials**

In this and the next chapter, the main results of the thesis will be presented. In the chapter 1, I have reviewed some of the early post-graphene 2D materials, and their physical properties in chapter 3. As it has been defined, the properties discussed before belong to the basic property category. In this chapter, I will present my works on the determination of some of the advanced properties, namely thermal properties, piezoelectric properties, carrier mobility, magnetic properties and Li battery related properties. In addition, along with these new properties I will also introduce several new 2D materials on which the property determinations were carried out. They are phosphorene, monolayer Titanium trisulfide, penta-hexa-graphene and MXenes. Each of the sections below comes from one publication.

### **4.1 Thermal properties of phosphorene<sup>1</sup>**

#### **4.1.1 Introduction: Phosphorene**

Black phosphorene (black P) is a single atomic layer of layered material black phosphorus and has been successfully exfoliated [139, 140]. Similar to the multiphase structures in phosphorus, there have been at least six different possi-

---

<sup>1</sup>This work is published in: P2.

ble stable two dimensional allotropes of phosphorene were proposed[141–143]. This multi-phase nature is because that in contrast to the C atoms of graphene, the P atoms in phosphorene have  $sp^3$ -hybridized orbitals. This is mainly caused by the extra valence electron of P atom in comparison to carbon. Indeed, if this extra electron is placed in a  $sp^2$ -hybridized structure, they would occupy the energetically unfavourable (antibonding)  $\pi^*$  band. However, with  $sp^3$ -hybridization, a  $\sigma$ -bond network can be formed with three  $sp^3$  orbitals and the other  $sp^3$  orbital is used to host the remaining electron pair. This leads to an essentially tetragonal coordination of the P atoms and results in a buckled nature of  $sp^3$ -hybridized sheets, see Fig. 4.1 for the structures. The out-of-plane positions of the atoms in  $sp^3$ -hybridized sheets give rise to various possible structural phases which are absent in  $sp^2$ -hybridized systems. Among those, black P, also referred as the  $\alpha$  phase, is the most stable allotrope. However, the cohesive energy of blue phosphorene (blue P), or the  $\beta$  phase, is only a few meV higher than that of black P, while other crystal structures are much less favourable with energy at least by  $\sim 80$  meV/atom higher.

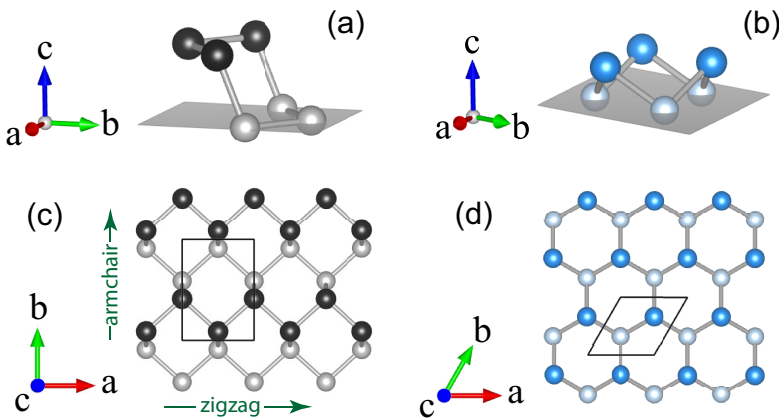


Fig. 4.1 (a) and (b) are the one hexagonal rings of black P and blue P, their top viewed structures are shown in (c) and (d), respectively. Atoms are coloured in accordance with the names of the structures. Lighter coloured atoms mean they are lower in vertical position. Black boxes in top views are the primitive unit cell used in our calculations.

Triggered by its realization, various physical properties of phosphorene have been explored. Electronically, black P is a semiconductor with a direct band

gap at the  $\Gamma$  point[141, 144]. Experimentally, photoluminescence excitation spectroscopy measured a quasi-particle band gap of 2.2 eV[145], which is larger than its bulk band gap, i.e. 0.31-0.33 eV[146, 147]. Due to its electronic structure, black P has been proposed as a potential novel material in nanoelectronics and optoelectronics, especially in the infrared regime. High performance black P based transistors with a mobility up to  $1000 \text{ cm}^2/\text{V}\cdot\text{s}$  and an on/off ratio up to  $10^4$  at room temperature have been reported[139, 140]. Similar to black P, blue P was predicted to be a semiconductor material with an indirect band gap around 2.00 eV[141]. Therefore, it can be potentially used for field-effect transistor applications. The high mobility and tunable finite band gap of phosphorene, among other promising properties[148–152], make it an interesting new member of the 2D materials. Despite the mentioned studies that aimed to explore the physical properties of phosphorene, a more comprehensive knowledge of finite temperature effects on their properties haven't been reported. Given the fact that this knowledge could contribute to the acceleration in the progress towards its proposed applications, this study[P2] is urgently needed. To this end, here we explore the thermal properties of black p and blue p, their temperature-dependent lattice constant, thermal expansion coefficients, free energy and specific heat.

#### 4.1.2 Thermal expansion and Quasi-harmonic approximation

The thermal expansion is the expansion of material's volume at finite temperature. As shown in Fig. 4.2, it is directly related to the asymmetric of interatomic potential where the equilibrium position shift towards the flatter side of the potential energy profile and stay far away from the steeper side as the temperature increases. In below we will see how we can include this anharmonic potential using an approximation. The thermal expansion coefficient  $\alpha(T)$  are defined through the following formula:

$$\alpha(T) = \frac{1}{a_0(T)} \frac{da_0(T)}{dT}, \quad (4.1)$$

where  $T$  is the temperature,  $a_0(T)$  is the equilibrium lattice parameter corresponding to the minimum of the Helmholtz free energy.

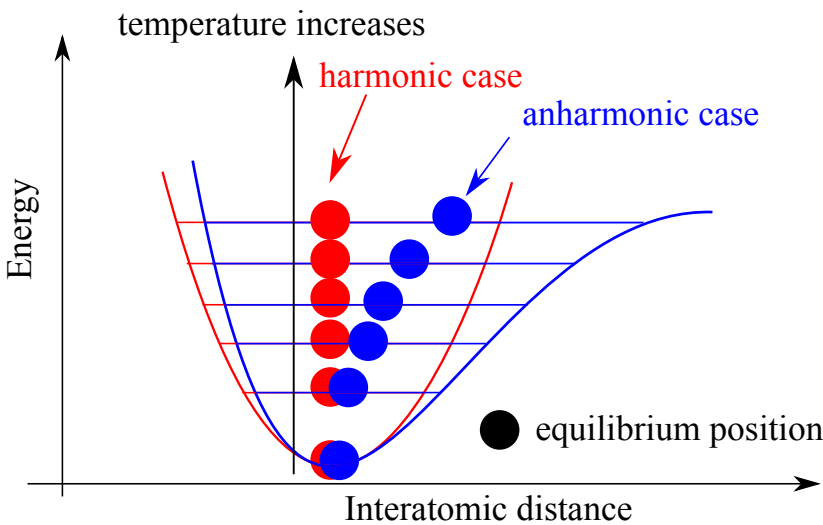


Fig. 4.2 Schematic illustration of the relation between asymmetric interatomic potential and thermal expansion.

In order to describe the thermal expansion within DFT, one needs to go beyond the harmonic approximation that is used to calculate the phonon frequency as we discussed in chapter 3. Harmonic approximation gives infinite thermal conductivity, infinite phonon lifetimes and temperature-independent vibrational and elastic properties, which are contradicted to experiment. Quasi-harmonic approximation (QHA)[153–156] is a way to include the approximated anharmonic effect through volume-dependent frequency within non-interacting phonons approximation. Although it is an implicitly inclusion of anharmonic effect, its dominant role in the thermal properties, that is two orders of magnitude larger than explicit anharmonic effect, make sure it can correctly describe the thermal properties up to melting point. Beyond this temperature, anharmonic effect will become important. QHA has been applied to a various compounds from semiconductors to metals and to Earth materials under extreme conditions[153, 157–159]. In Fig. 4.3, the applications of QHA for graphite and graphene are shown. The agreement between experiment and QHA is good in a wide range of temperature up to 2000 K. Another interesting point is that the negative thermal expansion, where the  $\alpha(T)$  is negative, is presented in both materials, especially, graphene persists such a feature up to 2000 K. This is a common character of layered materials where layers are weakly bonded. The origin of this related to the ZA mode in layered materials as discussed in chapter 3. At low temperature,

ZA mode will be excited and this out-of-plane vibration effectively shrinks the in-plane dimension of the materials thus gives negative thermal expansion.

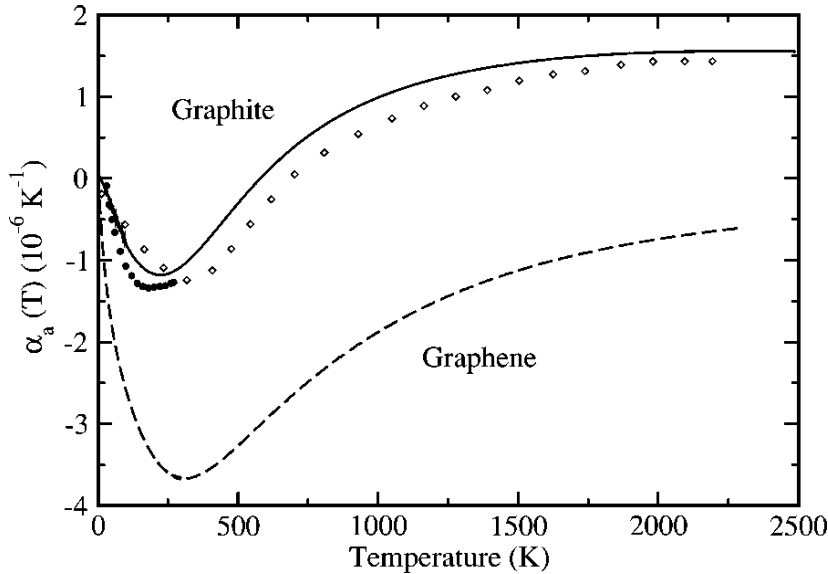


Fig. 4.3 Thermal expansion coefficients of graphite and graphene calculated using QHA (continuous line) and experimental result for graphite (points). Image source: [153]

Equilibrium lattice constants at any temperature  $a_0(T)$  are calculated by direct minimization of the Helmholtz free energy  $F(a, T)$  with respect to its independent lattice vector, i.e. in this case, **a** and **b** for black P, and **a** for blue P. For the minimization process,  $F(a, T)$  is obtained by fitting the discrete data points of  $F(a_i, T)$  to the third-order Birch-Murnaghan equation of state, where  $i$  is the label for different lattice constants or equivalently different strains. The  $F(a_i, T)$  is constructed from  $\omega_{\mathbf{q},j}^i$  and  $E[a_i]$  through the following formula[153, 160]:

$$F(a_i, T) = E[a_i] + \sum_{\mathbf{q},j} \frac{\hbar\omega_{\mathbf{q},j}^i}{2} + k_B T \sum_{\mathbf{q},j} \ln \left( 1 - \exp \left[ -\frac{\hbar\omega_{\mathbf{q},j}^i}{k_B T} \right] \right). \quad (4.2)$$

Here,  $T$  is the temperature,  $k_B$  is the Boltzmann constant,  $E[a_i]$  is the DFT ground state energy.  $\omega_{\mathbf{q},j}^i$  is the phonon frequency at the  $\mathbf{q}$  point  $\mathbf{q}$  with band index  $j$ . The sums run over all  $\mathbf{q}$  points and all bands of the whole Brillouin zone. Since the structural instabilities arise especially for the armchair direction when under compressive strain values larger than 4%, the calculation of phonon dispersions

for both structures are performed under small strains, namely  $\pm 2\%$ , in order to evaluate  $\omega_{q,j}^i$  and  $E[a_i]$ . Considering two independent lattice vectors **a** and **b** of black P two uniaxial strains are applied for these directions. While for blue P, only biaxial strain is applied to keep its hexagonal symmetry unchanged. The whole calculation process was carried out using phonopy-qha script[161].

#### 4.1.3 Computational details

**Simulation program:** VASP and Phonopy[162]

**Energy cut-off:** 500 eV

**Pseudopotentials:** PBE-GGA(PAW)

**k points (Monkhorst-Pack):**  $15 \times 11 \times 1$  and  $15 \times 15 \times 1$  for black P and blue P, respectively

**Vacuum:** 25 Å

**Energy and force convergence criterion:**  $10^{-5}$  eV and  $10^{-7}$  eV/Å, respectively

**Supercell for phonon calculation:**  $7 \times 3 \times 1$  and  $5 \times 5 \times 1$  for black P and blue P, respectively

**q points for phonon calculation:**  $200 \times 200 \times 1$

#### 4.1.4 Phonon modes and dispersion

Different from a pure planar graphene, black P and blue P have a buckled non-planar structure due to the  $sp^3$  hybridization, yet all three structures share the same hexagonal lattice base. Given an almost identical local environment in the unit cell, see Fig. 4.1, it is not surprising that blue P and black P having similar total energy. Only significant difference is the plane, marked as grey shown in Fig. 4.1, on which the system extends to form an infinite 2D crystal. Therefore, thermal expansion on these different planes are expected to be different and will carry insight information on the different finite temperature properties. The primitive unit cell of black P is a rectangular lattice with a four-atom basis and a space group of  $D_{2h}^7$ , and that of blue P is a hexagonal lattice with a two-atom basis and a space group of  $D_{3d}^3$ . Therefore, besides the three acoustic modes with the in-phase vibrations of atoms, there are nine and three optical modes for black P and blue P, respectively.

The calculated phonon dispersions along the high symmetric q lines corresponding to these modes are depicted in Fig. 4.4(a) and (b) for both structures. Parallel with the previous calculations [163, 164], the calculated phonon dispersions are free from imaginary frequencies, which ensures the structural stability

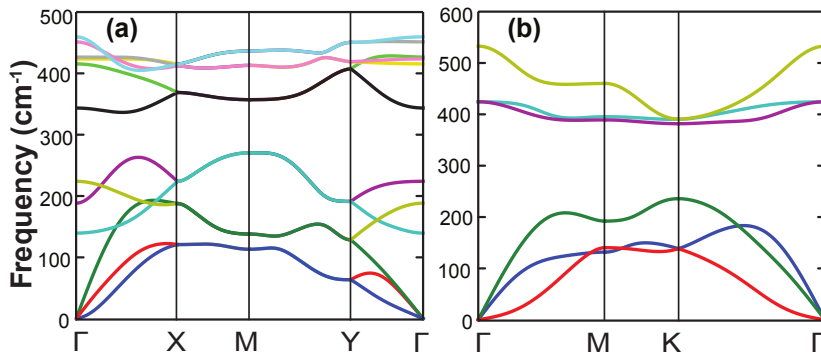


Fig. 4.4 Calculated phonon dispersions for pristine (a) black and (b) blue P. (c) Optical phonon modes together with their frequencies (in units of  $\text{cm}^{-1}$ ) at the  $\Gamma$  point and irreducible representations for black P and blue P.

of the materials. Lowest acoustic mode ZA displays a  $q^2$  relation as we discussed in chapter 3. The other two acoustic modes LA and TA still have a linear dependence with respect to the  $q$  wavevector since the situation is the same here as in the bulk. The total frequency range of the phonon dispersion is larger by an amount of about  $100 \text{ cm}^{-1}$  in blue P as compared to black P. We will discuss more about the vibrational character of these phonon modes in the later chapters where we investigate the effect of strain on the frequency of the vibration.

#### 4.1.5 Results of temperature-dependent thermal properties

The equilibrium lattice constants at zero K,  $a_0$  and  $b_0$  of black P and  $a_0$  of blue P, are predicted as  $a_0 = 3.298 \text{ \AA}$ ,  $b_0 = 4.625 \text{ \AA}$ , and  $a_0 = 3.277 \text{ \AA}$ , respectively, in good agreement with previously reported results ( $a_0 = 3.297 \text{ \AA}$ ,  $b_0 = 4.640 \text{ \AA}$  for black P[144, 165], and  $a_0 = 3.330 \text{ \AA}$  for blue P[141]). The expansion of these lattice parameters due to zero-point vibration is around 0.2% at 0 K, which is smaller than that of other well-known two dimensional materials like graphene and *h*-BN, but it is comparable with that of MoS<sub>2</sub> and MoSe<sub>2</sub>. This result is reasonable due to the difference in the maximum phonon frequency between these materials: that of graphene and *h*-BN is around  $1600 \text{ cm}^{-1}$  and that of MoS<sub>2</sub>, MoSe<sub>2</sub>, black P and  $a_0$  of blue P is around  $600 \text{ cm}^{-1}$ .

The temperature dependence of the lattice constants  $a_0(T)$ ,  $b_0(T)$  and thermal expansion coefficients (TEC)  $\alpha(T)$  of both structures are shown in Fig. 4.5. Anisotropic nature of the structure of black P leads to different lattice constant

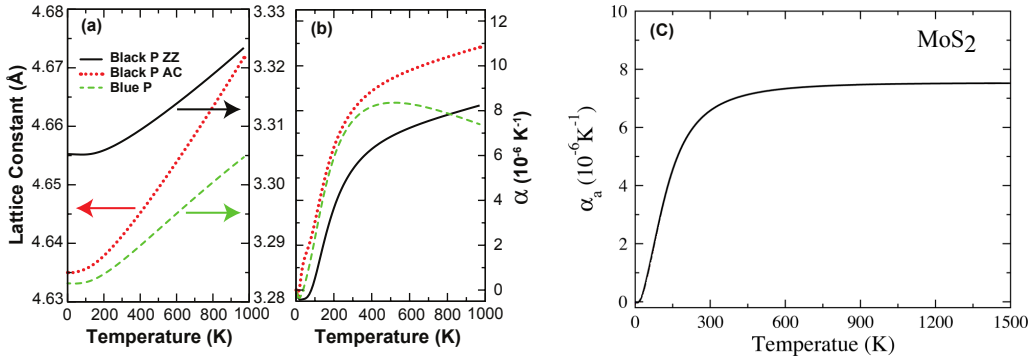


Fig. 4.5 (a) Lattice constants and (b) TEC as a function of temperature. Here, ZZ and AC are denoted for the zigzag and armchair directions, respectively. (c) TEC of monolayer MoS<sub>2</sub> for comparison from Ref. [155].

expansion rates. A faster thermal expansion along the armchair direction (i.e. **b**) is found, see Fig. 4.5(a). While a small negative TEC appears for all structures in all directions at temperatures lower than 100 K, black P along the zigzag direction has a more apparent negative expansion. The lattice constant of both phases varies linearly when  $T > 200$  K, see Fig. 4.5(a). The TEC increases rapidly with temperature up to 300 K. After that, all TECs changes slowly with temperature starting from around 400 K in agreement with predictions for two-dimensional transition metal dichalcogenides [154, 155], for example see Fig. 4.5(c) for monolayer MoS<sub>2</sub>. Different from MoS<sub>2</sub>, we do not observe any saturation of the TEC for black P at high temperatures. While black P expands at most 0.02 Å along the zigzag direction as T approaches 1000 K, it expands 0.04 Å along the armchair direction. As is clear from Fig. 4.1, an uniaxial expansion along the armchair direction may result in a structural phase transition from black P to blue P because of the similar hexagonal arrangement of P atoms[166].

In Fig. 4.6, the variation of the cohesive energy as a function of strain at 0 K (a) and the variation of the Helmholtz free energy (F(T)) as a function of temperature (b) are presented. In Fig. 4.6(b), we also show  $\Delta F(T)$  which is defined as  $\Delta F(T)=F_{blueP}(T) - F_{blackP}(T)$ . Here,  $F_{blueP}(T)$  and  $F_{blackP}(T)$  are the Helmholtz free energy of black P and blue P, respectively. As the zero-point energy continuously decreases with strain from minus to plus, the variation of the zero-point energy results in an asymmetric behaviour in cohesive energy with strain. In addition, the curvature of this total energy gives the in-plane stiff-

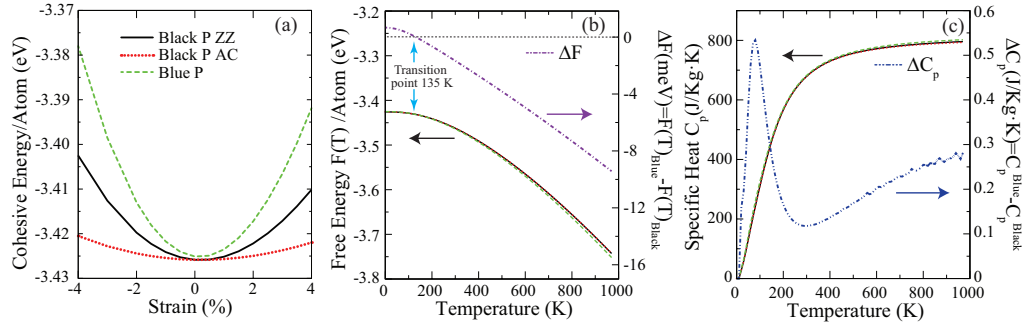


Fig. 4.6 (a) Cohesive energy, including zero point energy, as a function of applied strain at  $T = 0$  K and (b) Helmholtz free energy ( $F(T)$ ) as a function of temperature. Here, ZZ and AC are used for the zigzag and armchair directions, respectively.  $\Delta F(T)$  is the difference between  $F(T)$  of black P and blue P. The blue arrow (b) denotes the transition point, after which blue P becomes thermodynamically more stable over black P. The specific heat at constant pressure ( $C_p$ ) and the difference ( $\Delta C_p$ ) between  $C_p$  of black P and blue P are shown in (c).

ness of the material as a measure of the response to mechanical deformation. It is clear that blue P is a stiffer material as compared to black P. Moreover, the deformation along the zigzag direction of black P is harder than that along the armchair direction at 0 K, and this is consistent with the finite temperature behaviour as we conclude from previous section in connection with Fig. 4.5(a).

The  $F(T)$  decreases as temperature increases due to the entropy term (the last term in equation (4.2)). Inclusion of the zero-point energy gives rise to a slightly higher ground state energy for blue P over black P since its optical phonon modes have larger frequencies. However, as temperature increases, a crossing of the free energy curves around 135 K occurs, which makes the blue P energetically more favorable at high temperatures, see Fig. 4.6(b). The free energy difference between the two phases is of the order of 4 meV at room temperature, meaning that the two phases can coexist. In addition, it is possible to observe a phase transition driven by temperature from black P to blue P or visa versa at  $T=135$  K.

In Fig. 4.6(c), we present constant pressure heat capacity,  $C_p$ , results for both structures, which is generally few percent differ from constant volume heat capacity in similar structures[153]. The  $C_p$  difference ( $\Delta C_p$ ) between two phases is significantly small for all temperature range as represented with blue dash dot line in Fig. 4.6(c), which states essentially very similar Debye temperature for

these two different phases. At high temperatures,  $C_p$  approaches its classical value of  $12 k_B$ . When  $T=300$  K,  $C_p$  already reaches about 80 % of its classical value, meaning that the most of the phonon modes are activated at this temperature.

#### 4.1.6 Summary

In summary, we systematically investigate the lattice thermal properties of black and blue P. Similar to its electronic properties, black P has direction dependent mechanical and thermal properties. The calculated thermal expansion coefficients demonstrate that a much larger expansion along the armchair direction with temperature is observed for black P. While black P is thermodynamically more stable than blue P, the latter becomes more stable when  $T > 135$  K, yet their free energy difference is small due to their structural similarities. It is possible to observe a structural phase transition from black P to blue P by increasing temperature beyond 135 K, and therefore the coexistence of these two phases is possible.

### 4.2 Piezoelectric properties of 2D-TMDs and 2D-TMDOs<sup>2</sup>

#### 4.2.1 Introduction

We have seen the general properties of 2D-TMDs in chapter 1 and vibrational and electronic properties of their one member: 2D-MoS<sub>2</sub> in chapter 3. When the S atom is replaced with O, TMDs become transition metal dioxides (TMDOs), whose monolayer have similar properties as 2D-TMDs. For the consistency with the paper, here in this section we refer to the 2D-TMDs as 2D-TMDCs. Although 2D-TMDOs proven to be stable, they have not been synthesis yet. Sharing similar electronic strucutre, 2D-TMDCs and 2D-TMDOs already demonstrating various of potential applications, such as nanoelectronic and nanophotonic devices for their direct finite band gaps[66, 167]. In addition to these exciting applications, 2D-TMDCs in the noncentrosymmetric 2H crystal structure with  $D_{3h}$  symmetry have also been shown to have remarkable piezoelectric properties that can be

---

<sup>2</sup>This work is published in: P3.

then use in pressure sensors, transducers, high voltage generators, nonlinear energy harvesters, energy conversion and piezotronic applications. Many layered materials have a centrosymmetry which suppresses the piezoelectricity. However, this symmetry will be broken when it searches the monolayer level, and then the piezoelectricity is recovered. For example, graphene preserves the centrosymmetry as in graphite, or inversion symmetry, due to its non-polar nature thus it does not display piezoelectricity; Whereas 2D-BN and 2D-TMDs break such symmetry and become noncentrosymmetric system where piezoelectric effect can manifest themselves.

Duerloo *et al.* [168] calculated the piezoelectric properties of single layer of BN, MoS<sub>2</sub>, MoSe<sub>2</sub>, MoTe<sub>2</sub>, WS<sub>2</sub>, WSe<sub>2</sub>, and WTe<sub>2</sub> by using first principle calculations. They reported that piezoelectricity of the 2D-TMDC monolayers in H phase are comparable or even better than that of conventional bulk piezoelectric materials. Zhu *et al.* [169] reported experimental evidence of piezoelectricity in free-standing MoS<sub>2</sub> and they found that this material exhibits piezoelectricity for an odd number of layers in which case inversion symmetry is broken. Their measured piezoelectric coefficient is  $2.9 \times 10^{-10}$  C/m, which agrees well with previous theoretical calculations[168]. Similarly, by using DFT based theoretical calculations, it has been predicted that group III monodichalcogenides, namely GaS, GaSe and InSe, have piezoelectric stress coefficients of  $1.34 \times 10^{-10}$ ,  $1.34 \times 10^{-10}$  and  $1.47 \times 10^{-10}$  C/m, respectively[170]. In addition, reducing the dimensionality has been shown to enhance piezoelectricity in ZnO[171]. These studies indicate that TMDCs are promising candidates as low dimensional piezoelectric materials.

Since previous calculations and experiments were only focused on Mo and W based TMDs, the potential of other 2D-TMDCs and 2D-TMDOs for piezoelectric device applications have remained an open question so far. To reveal such potential, first principles calculations are performed in order to systematically investigate the piezoelectric properties of single layer 2H-MX<sub>2</sub> compounds, where M= Cr, Mo, W, Ti, Zr, Hf, Sn and X=O, S, Se, Te. Lattice parameters, atomic positions, electronic band-gap values, elastic stiffness constants ( $C_{11}$  and  $C_{12}$ ), Young modulus ( $Y$ ), Poisson's ratios ( $\nu$ ), piezoelectric stress coefficients ( $e_{11}$ ) and piezoelectric strain coefficients ( $d_{11}$ ) are calculated.

### 4.2.2 Piezoelectric constants

Piezoelectricity is the ability of some materials to generate internal electric field in response to applied mechanical stress. Two types of piezoelectric phenomena can be observed for piezoelectric materials: 1) direct piezoelectric effect: separation of opposite charge due to stress and 2) converse piezoelectric effect: occurrences of stress and strain under external electric field. In Fig. 4.7, the mechanism of direct piezoelectric effect is shown.

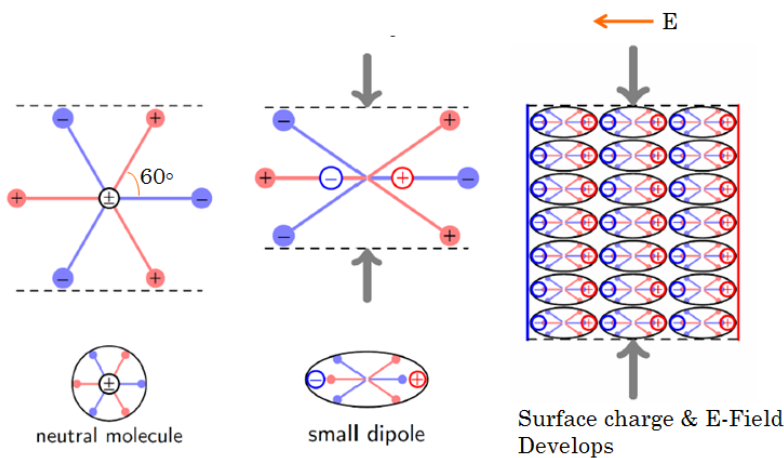


Fig. 4.7 Mechanism of direct piezoelectric effect. Image source: [172]

To investigate the piezoelectric properties, we follow the same theoretical approach of Ref. [168]. The piezoelectric tensor[173, 174],  $e_{ij}$ , can be defined in terms of the induced polarization in the direction  $i$  due to a strain ( $\varepsilon_j$ ) change along the direction  $j$  as follows

$$e_{ij} = \partial P_i / \partial \varepsilon_j = \partial P_i / \partial \varepsilon_j |_u + \sum_k (\partial P_i / \partial u_{ik}) (\partial u_{ik} / \partial \varepsilon_j). \quad (4.3)$$

where  $P_i$  is the induced polarization along the direction  $i$  as a result of an applied strain  $\varepsilon_j$  along the direction  $j$ . The  $P_i$  is calculated using the Berry Phase approach[175] as implemented in the VASP package with applied uniform strain, ranging from 0.01 % to -0.01 % in steps of 0.005 %, along the armchair side of the rectangular cell. At this point, in order to apply strain in a desired direction, the hexagonal primitive cell structure of each material is transformed to a tetragonal one composed of two hexagonal primitive cells[168], see Fig. 4.8. The first

term in equation (4.3) is the clamped-ion or homogeneous strain contribution to the piezoelectric tensor and it mainly arises from the electronic contribution. The second term represents the contribution from the internal relaxation of ions. Here,  $u_{ik}$  is the fractional coordinate of the  $k^{th}$  atom along the  $i$  direction of the unit cell.

Since TMDCs and TMOs compounds have a non-centrosymmetric crystal structure, the inclusion of internal relaxation becomes essential in order to obtain realistic piezoelectric properties. In addition, it is clear that the relaxed-ion piezoelectric coefficients are experimentally relevant quantities that can be measured. From the theoretical point of view, since the relaxed-ion piezoelectric coefficients include both electronic and relaxation effects, the calculation of the clamped-ion piezoelectric coefficients helps to separate the electronic and relaxation contributions from the relaxed-ion piezoelectric coefficients. The number of independent piezoelectric tensor coefficient is deduced from the symmetry of the crystal. For TMDCs and TMOs, we only need to calculate the  $e_{11}$  component of the piezoelectric stress tensor.  $e_{11}$  relates in-plane strain to in-plane electrical polarization. The piezoelectric coefficient  $e_{31}$  is zero due to the presence of an inversion centre between the two layers of chalcogenides. However, it is found to be non-zero for the unsymmetrical H and F co-decorated graphene[176, 177].

The corresponding piezoelectric strain tensor ( $d_{11}$ ) of each material is predicted from the following relation[168]:

$$d_{11} = e_{11}/(C_{11} - C_{12}). \quad (4.4)$$

For each applied strain, the ions are kept in their strained positions or allowed to relax to their new equilibrium positions, and consequently the clamped-ion or relaxed-ion piezoelectric properties are calculated, respectively.

### 4.2.3 Computational details

**Simulation program:** VASP

**Energy cut-off:** 600 eV

**Pseudopotentials:** PBE-GGA(PAW), HSE06

**k points (Monkhorst-Pack):**  $26 \times 26 \times 1$

**Vacuum:** 15 Å

**Energy and force convergence criterion:**  $10^{-3}$  eV and  $10^{-7}$  eV/Å, respectively

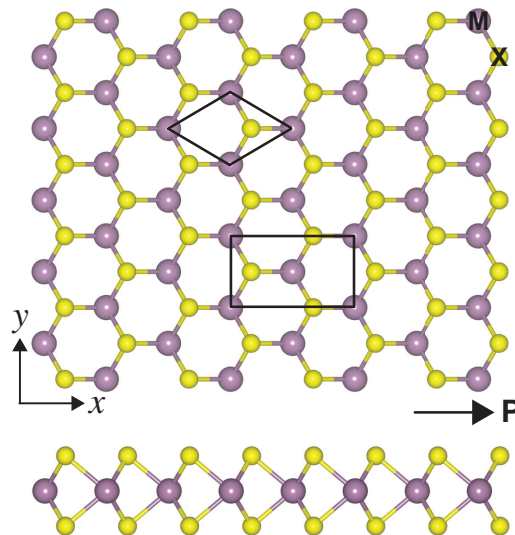


Fig. 4.8 Top and side views of  $\text{MX}_2$  where  $\text{M} = \text{Cr}, \text{Mo}, \text{W}, \text{Ti}, \text{Zr}, \text{Hf}, \text{Sn}$  and  $\text{X} = \text{O}, \text{S}, \text{Se}, \text{Te}$ .  $\text{P}$  denotes the direction of the polarization. Piezoelectric calculations are done in a rectangular cell.

**strain applied:** 1% to -1% in steps of 0.5%

**stress and force:** finite displacement method

**polarization:** Berry Phase expression [175] in VASP

#### 4.2.4 Accurate band gaps from HSE06 hybrid functional

It is mandatory that a piezoelectric material has to be an insulator or semiconductor with a sufficiently wide band gap to avoid current leakage. Thus, we first calculate the electronic properties of twenty eight single layer  $\text{MX}_2$  compounds, where  $\text{M} = \text{Cr}, \text{Mo}, \text{W}, \text{Ti}, \text{Zr}, \text{Hf}, \text{Sn}$  and  $\text{X} = \text{O}, \text{S}, \text{Se}, \text{Te}$ . We discard the metallic structures, namely  $\text{SnSe}_2$ ,  $\text{SnTe}_2$ , and  $\text{TiTe}_2$ . Actually,  $\text{G}_0\text{W}_0$  calculations predicted that 2H-TiTe<sub>2</sub> is a small band gap semiconductor material[178]. Since semi-local functionals are used in the Berry's phase calculations, 2H-TiTe<sub>2</sub> is excluded. For electronic structure calculations, we also applied the HSE06 hybrid functionals in order to obtain realistic electronic band gap values for TMDCs and TMDOs. Fig. 4.9 shows the calculated PBE-GGA and HSE06 band gap values  $E_{gap}$ . The materials, except Cr, Mo, and W based TMDCs, have indirect band gaps and the predicted values and trends are in good agreement with previous theoreti-

cal calculations[168, 179, 180]. Generally, the band gap increases when moving upwards in the chalcogens family from Te to S and with increasing atomic number in the transition metals. However, the latter trend is partially valid when the compounds with O are included. The difference is that within the same row of the transition metals, TMDOs with a larger atomic number tend to have smaller band gaps which is in contrast to the TMDCs case.

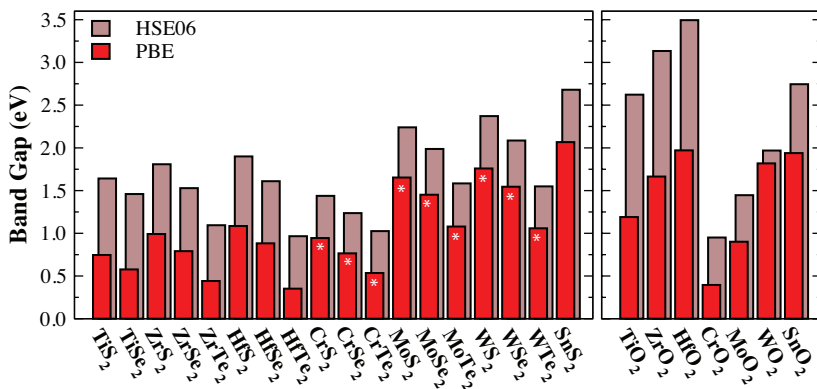


Fig. 4.9 The calculated PBE-GGA and HSE06  $E_{gap}$  values for TMDCs and TMDOs. Here, white \* sign indicates that it is a direct band gap material.

#### 4.2.5 Elastic constants

As previously mentioned, we need to calculate the elastic constants in order to obtain the piezoelectric strain,  $d_{11}$  coefficients, see equation (4.4). Therefore, the relaxed-ion and clamped-ion elastic stiffness coefficients ( $C_{11}$  and  $C_{12}$ ), Young modulus ( $Y = (C_{11}^2 - C_{12}^2)/C_{11}$ ) and Poisson's ratios ( $\nu = C_{12}/C_{11}$ ) for all 2D-TMDC and 2D-TMDO materials considered in this study are obtained and are listed in table 4.1. Our results are in good agreement with available data[135, 168, 181, 182]. The first observation from table 4.1 is that  $C_{11}$ ,  $C_{12}$  and  $Y$  decreases with increase of the row number of the chalcogenide atom. Except Zr, in each chalcogenide group, the  $MX_2$  monolayer becomes stiffer with increase of the row number of the metal atom. Structures considered in this study are found to be less stiff when compared to graphene ( $Y=341$  N/m)[154] and single layer *h*-BN ( $Y=275.9$  N/m)[154]. Also it should be noticed that the calculated elastic constants are positive and satisfy the Born stability criteria for crystals having hexagonal symmetry[131, 183]. Note that the relaxed-ion elastic constants, i.e.  $C_{11}$  and  $C_{12}$ , are

Table 4.1 Calculated clamped and relaxed-ion elastic constants (in units of N/m), Young modulus Y (in units of N/m) and Poisson's ratio  $\nu$ .

Material	Clamped Ion				Relaxed Ion			
	$C_{11}$	$C_{12}$	$Y$	$\nu$	$C_{11}$	$C_{12}$	$Y$	$\nu$
TiS <sub>2</sub>	100.3	34.2	88.6	0.34	89.9	28.6	80.8	0.32
TiSe <sub>2</sub>	84.8	29.3	74.7	0.35	74.4	24.4	66.4	0.33
ZrS <sub>2</sub>	96.3	37.7	81.5	0.39	84.2	31.8	72.2	0.38
ZrSe <sub>2</sub>	83.3	31.0	71.8	0.37	71.4	26.0	61.9	0.36
ZrTe <sub>2</sub>	66.2	22.8	58.35	0.34	53.1	18.6	46.6	0.35
HfS <sub>2</sub>	104.4	39.1	89.8	0.37	92.8	33.8	80.5	0.36
HfSe <sub>2</sub>	89.7	32.2	78.1	0.36	78.8	27.8	69.0	0.35
HfTe <sub>2</sub>	71.0	23.5	63.2	0.33	59.3	19.7	52.8	0.33
CrS <sub>2</sub>	136.9	42.6	123.6	0.31	120.6	32.3	111.9	0.27
CrSe <sub>2</sub>	111.3	37.5	98.7	0.34	96.6	28.9	87.9	0.30
CrTe <sub>2</sub>	86.5	32.7	74.1	0.38	73.0	25.8	63.9	0.30
MoS <sub>2</sub>	157.2	50.1	141.2	0.32	132.7	33.0	124.5	0.25
MoSe <sub>2</sub>	133.2	40.8	120.7	0.31	106.9	25.6	100.8	0.24
MoTe <sub>2</sub>	106.3	32.8	96.2	0.31	84.1	19.8	79.4	0.24
WS <sub>2</sub>	174.7	51.9	159.3	0.30	146.5	31.8	139.6	0.22
WSe <sub>2</sub>	147.4	41.1	135.9	0.28	102.4	23.1	115.9	0.23
WTe <sub>2</sub>	115.4	31.6	106.8	0.27	89.2	15.7	86.4	0.18
SnS <sub>2</sub>	92.8	23.1	87.1	0.25	91.0	22.2	85.6	0.24
TiO <sub>2</sub>	178.9	80.9	142.3	0.45	173.7	75.7	141.7	0.44
ZrO <sub>2</sub>	163.5	83.0	121.5	0.51	157.4	77.5	119.2	0.49
HfO <sub>2</sub>	181.7	86.7	140.3	0.48	174.2	81.5	136.1	0.47
CrO <sub>2</sub>	233.8	87.4	201.1	0.37	218.6	74.4	193.3	0.34
MoO <sub>2</sub>	253.3	104.0	210.6	0.41	230.2	84.5	199.2	0.37
WO <sub>2</sub>	286.2	109.0	244.7	0.38	261.2	87.8	231.7	0.34
SnO <sub>2</sub>	165.7	52.4	149.1	0.32	160.2	53.3	142.5	0.33

always smaller than the clamped-ion ones since the internal relaxation of ions allows to release some of the stress in the former, see table 4.1.

#### 4.2.6 Piezoelectric stress/strain coefficients

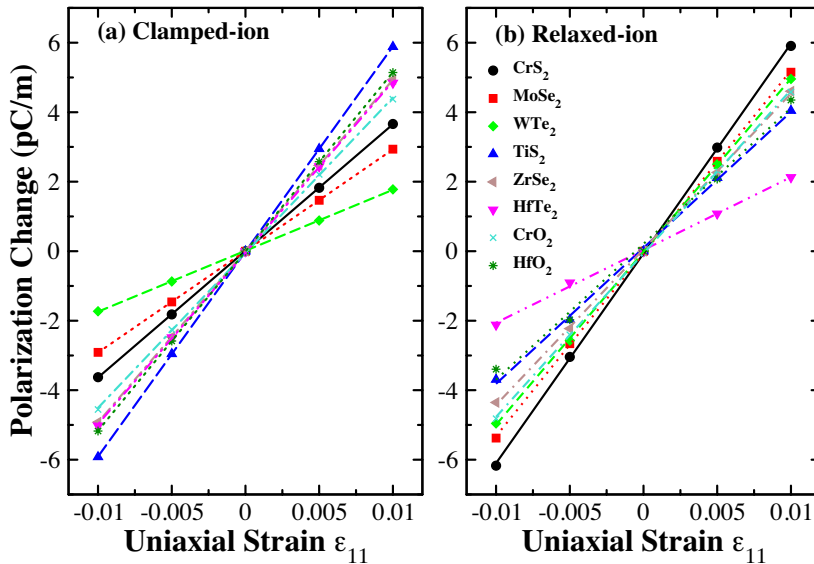


Fig. 4.10 (a) Clamped-ion and (b) relaxed-ion polarization change under applied uniaxial strain ( $\epsilon_{11}$ ) along the x direction for the selected 2D-TMDCs and 2D-TMOs structures. Piezoelectric coefficient is determined from the slope of the curves.

Piezoelectric coefficients ( $e_{11}$ ) are derived from the slope of the polarization change in Fig. 4.10 with applied uniform strain, ranging from 0.01 % to -0.01 % in steps of 0.005 %, along the armchair side of the rectangular cell via Berry's Phase approximation[175]. The clamped-ion and relaxed-ion  $d_{11}$  coefficients are obtained by using the calculated  $e_{11}$  coefficients, and the elastic constants ( $C_{11}$  and  $C_{12}$ ) via equation (4.4). Fig. 4.11 shows the calculated  $e_{11}$  and  $d_{11}$  coefficients for both TMDCs and TMOs. The materials are ordered along the x-axis by considering the period and group number of the transition metal element in the periodic table. The predicted relaxed-ion  $e_{11}$  and  $d_{11}$  coefficients are consistent with the available reference data[168, 184], see results for Cr, Mo and W based TMDCs, which are comparable with the piezoelectric properties of single layer and bulk h-BN[168, 185–187]. In addition, the relaxed-ion  $e_{11}$  coefficient of

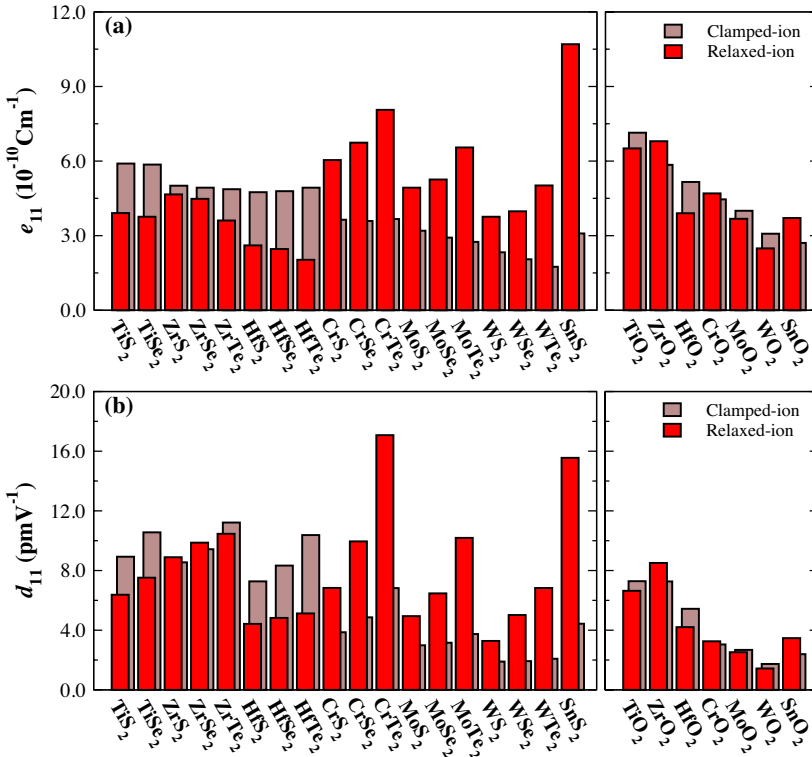


Fig. 4.11 The calculated clamped and relaxed-ion (a) piezoelectric stress ( $e_{11}$ ) and (b) piezoelectric strain ( $d_{11}$ ) coefficients.

single layer MoS<sub>2</sub> ( $4.91 \times 10^{-10}$  C/m) is comparable with the experimentally measured piezoelectric coefficient of  $2.90 \times 10^{-10}$  C/m[169] and agrees well with the reported value of  $3.64 \times 10^{-10}$  C/m.[168]. In addition, the trends found for the  $e_{11}$  and  $d_{11}$  coefficients of Mo and W based TMDCs are consistent with those found in Ref.[168]. The difference between our calculated piezoelectric coefficients and previous calculations is likely due to the use of different pseudopotentials, small differences in elastic constants, and other computational parameters (for instance  $k$ -mesh).

SnS<sub>2</sub> has the highest  $e_{11}$  coefficient for the relaxed-ion ( $10.7 \times 10^{-10}$  C/m) calculation. WO<sub>2</sub> has the smallest relaxed-ion piezoelectric stress coefficient ( $2.49 \times 10^{-10}$  C/m) among TMDOs and WTe<sub>2</sub> has the smallest clamped-ion piezoelectric stress coefficient ( $1.75 \times 10^{-10}$  C/m). From Fig. 4.11, we predict several periodic trends in clamped-ion  $e_{11}$  and  $d_{11}$  coefficients for TMDC and TMDO monolayers. The clamped-ion  $e_{11}$  coefficients of TMDCs usually increase when moving

from right to left in the periodic table (i.e., from  $\text{CrX}_2$  to  $\text{TiX}_2$ ) and upward in an individual group of both transition metal and chalcogen atoms. This trend is nearly the same for TMDOs. However, for TMDCs, the trend (i.e., the increase in the calculated clamped-ion  $e_{11}$  coefficients when moving upward in the group of chalcogen elements) becomes reversed for the relaxed-ion calculations of group VI elements as clearly seen in Fig. 4.11(a). The clamped and relaxed ion  $d_{11}$  coefficients increase when moving downward in the group of chalcogen elements (i.e. from S to Te) in each metal group. This trend can be correlated to the polarizability of chalcogen atoms since the atoms are easily polarized when going downward in a specific group of the periodic table. We notice that the chalcogenide atoms have a much larger impact on the  $d_{11}$  coefficients as compared to the metal atoms. Especially in group VI, the  $d_{11}$  coefficient is maximized if one uses a smaller metal atom and a larger chalcogen atom. In group IV, Zr does not exhibit the same trend that is found for the group VI elements. This is partially because the  $C_{11}$  elastic constant of Zr based TMDCs for a particular chalcogen atom is smaller than that of Ti and Hf based TMDCs. Since TMDOs pose larger elastic constants, they usually have smaller  $d_{11}$  coefficients as compared to TMDCs. In other words, the stronger the material the smaller the  $d_{11}$  coefficient.

Among the group VI elements (i.e., Cr, Mo and W), Cr based TMDCs and TMDOs are found to have much better piezoelectric properties in each chalcogenide group and  $\text{CrTe}_2$  possesses the largest relaxed-ion  $e_{11}$  ( $8.06 \times 10^{-10} \text{ C/m}$ ) and  $d_{11}$  (17.1 pm/V) coefficients. On the other hand, the relaxed-ion  $e_{11}$  and  $d_{11}$  coefficients of  $\text{SnS}_2$  are almost the same as those of  $\text{CrTe}_2$ . The predicted relaxed-ion  $e_{11}$  values are much larger than the values previously predicted for surface decorated graphene structures[188]. Furthermore, when the piezoelectric coefficients of the extensively used bulk piezoelectric materials, namely 2.3 pm/V for  $\alpha$ -quartz[189], 3.1 pm/V for wurtzite GaN[190] and 5.1 pm/V for AlN[190], are considered, we predict that TMDCs and TMDOs have comparable or even larger relaxed-ion piezoelectric coefficients.

#### 4.2.7 Importance of internal relaxation

It is essential to discuss the effect of the internal relaxation on the piezoelectric properties of TMDCs and TMDOs. Relaxing the ion positions after applying strain

significantly reduces (increases) the polarization of the Ti, Zr and Hf (Cr, Mo and W) based TMDCs. As a result, the clamped-ion piezoelectric coefficients of the Ti, Zr and Hf (Cr, Mo and W) based TMDCs monolayers are much larger (smaller) than that of the relaxed-ion coefficients. This means that the electronic contribution, i.e. the first term in equation (4.3), and strain contribution, i.e. the second term in equation (4.3), have opposite (the same) sign for the Ti, Zr and Hf (Cr, Mo and W) based TMDCs. The calculated elastic constants suggest that Ti, Zr and Hf based TMDCs are more brittle materials that are expected to exhibit larger response to an applied strain, thereby giving rise to higher clamped-ion piezoelectric constants. For TMDOs, the contribution of internal relaxation to the  $e_{11}$  coefficient decrease when moving downward in an individual metal group. However, in each chalcogen group, the internal relaxation becomes generally less important when going from Te to S. This can be attributed to the large strain-induced ionic motion in response of an applied strain. In other words, after applying strain, the amount of the internal relaxation of the chalcogen atoms increases from S to Te, giving rise to a larger internal relaxation contribution to the piezoelectric coefficients in Te based TMDCs. Since Te is the most easily polarizable atom among the chalcogenide atoms (due to its larger size), the polarization effects (and hence electronic contribution to the  $e_{11}$  coefficient) are found to be large in Te based TMDCs as compared to S and Se counterparts. However, the increase in piezoelectricity effects competes with the degradation of stability.

#### 4.2.8 Summary

In summary, we presented a detailed theoretical investigation of the piezoelectric properties of semiconductor TMDC and TMDO monolayers. Our calculations show that TMDC and TMDO structures are strong candidates for future atomically thin piezoelectric applications. We show that Ti, Zr, Sn and Cr based TMDCs and TMDOs have much better piezoelectric properties as compared to Mo and W based TMDCs and TMDOs and the well-known conventional bulk piezoelectric materials. The usage of these 2D piezoelectric materials in ultra sensitive sensors, low-power electronics and nanoscale electromechanical systems are expected to have an impact on the size reduction, weight and energy consumption of such devices.

## 4.3 Magnetic properties of penta-hexa-graphene<sup>3</sup>

### 4.3.1 Introduction

Magnetic material is a key ingredient for the unprecedented progress that has been made in the modern information technology over the recent decades. The exploration in this direction also includes the discovery of new materials and the invention of new devices. Considering the very low spin-orbit coupling and long spin relaxation time in graphene-related 2D systems, substantial effort has been devoted to the induction of magnetism in these metal-free materials with the aim for future spintronic devices[191, 192]. Intrinsic magnetism in graphene is absent, but extrinsic magnetism has been achieved by means of partial hydrogenation[42, 193], foreign atom substitution[194, 195] and the introduction of defects[196, 197].

Three types of orbital hybridization are usually found in carbon allotropes, namely  $sp$ ,  $sp^2$  and  $sp^3$ . While graphene is made of a network of  $sp^2$  hybridized atoms connected through  $\sigma$  and  $\pi$  bonds of  $p_z$  orbitals, diamond is exclusively held together by  $\sigma$  bonds between  $sp^3$  bonded atoms. Another class of carbon allotropes is formed by the graphynes and graphdiynes [198, 199]. These flat materials contain a mixture of  $sp$  and  $sp^2$  hybridized C atoms. Structures containing a mixture of  $sp^2$  and  $sp^3$  atoms, such as penta-graphene[200], have been studied[201–203] as well. This last structure contains a mixture of threefold and fourfold coordinated C atoms. This leads to a distorted structure with non-ideal bond angles that has higher formation energy than the non-distorted graphene and diamond crystals with their ideal planar and tetrahedral bonding geometry. Therefore, a system with a local bond structure resembling that of graphene or diamond will have lower energy.

None of the above mentioned materials are magnetic because they contain only paired electrons. Local magnetic moments usually originate from lone electrons that are not involved in chemical bonding. Single atomic defects such as vacancies break covalent bonds and create lone electrons that give rise to magnetism. It is interesting to investigate whether a structural modification with a proper mixing of three- and fourfold coordinated C atoms can lead to local mag-

---

<sup>3</sup>This work is published in: P4.

netic moments in a stable crystalline structure. In this work, we propose such a new type of 2D carbon allotrope with non-trivial magnetic properties. This structure is composed of a mixture of pentagonal and hexagonal rings of carbon atoms and will be called penta-hexa-graphene (ph-graphene), see Fig. 4.12. This new material has an antiferromagnetic (AFM) ground state that is higher in total energy as compared to the ferromagnetic (FM) state.

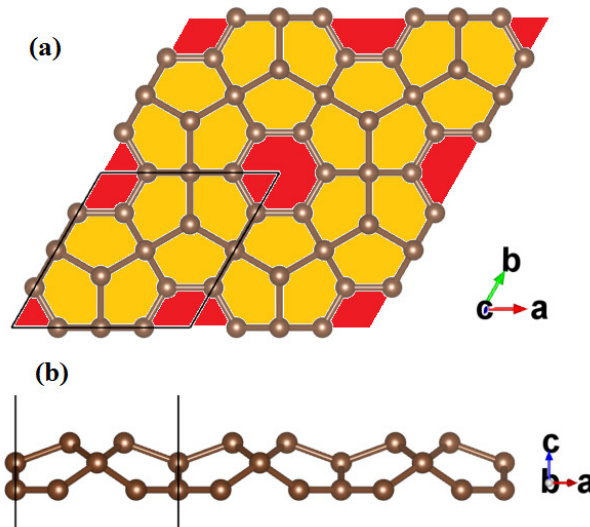


Fig. 4.12 Atomic structure of a  $2 \times 2$  supercell of monolayer ph-graphene. (a) Top view with hexagonal and pentagonal rings marked with red and yellow color, respectively; (b) Side view of the buckled structure. (Visualisation using VESTA [204])

### 4.3.2 Computational details

**Simulation program:** VASP

**Energy cut-off:** 500 eV

**Pseudopotentials:** PBE-GGA(PAW)

**$k$  points (Monkhorst-Pack):**  $15 \times 15 \times 1$

**Vacuum:** 25 Å

**Energy and force convergence criterion:**  $10^{-8}$  eV and  $10^{-7}$  eV/Å, respectively

**Supercell for phonon calculation:**  $3 \times 3 \times 1$

**phonon calculation:** density functional perturbation theory

### 4.3.3 Bond hybridization and magnetic moment

The structure of the proposed 2D material is schematically shown in Fig. 4.12. It consists of hexagonal rings of C atoms surrounded by six pentagonal rings which share one edge with the hexagon and four with other pentagons. These hexagonal and pentagonal rings are arranged in a hexagonal lattice to form an infinite monolayer sheet. Considering the complex structure of this system, it is important to understand the hybridization of the electronic orbitals. For this, we calculate the hybridization index of the three C atoms that have a unique local environment, namely C1, C2 and C3 in Fig. 4.13, through Coulson's theorem as discussed in subsection 3.1.2:  $1 + \sqrt{n_1 n_2} \cos\theta_{12} = 0$ , where  $\theta_{12}$  is the interorbital angle between orbital 1 and 2 (see Fig. 4.13) and  $n$  is the hybridization index.  $n$  corresponds to the index in the  $sp^n$  notation and determines the relative fraction of  $p$  orbitals with respect to the  $s$  orbital. The sum of the  $s$  fractions in all hybridized orbitals should equal 1, while it should be 3 for the sum of the  $p$  fractions.

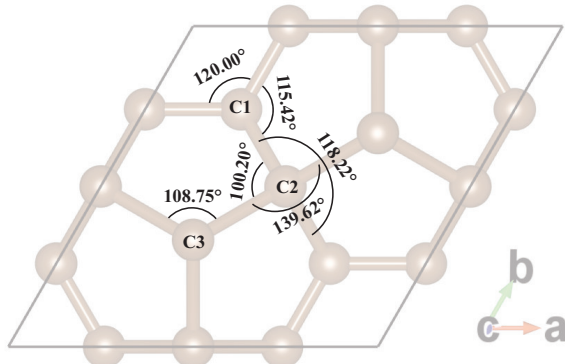


Fig. 4.13 Bond angles in the unit cell of monolayer ph-graphene.

Table 4.2 Orbital hybridization indices of the C atoms in ph-graphene.

Atom	$\varphi_1$	$\varphi_2$	$\varphi_3$	$\varphi_4$
C1	2.00	2.00	2.72	14.58
C3	3.11	3.11	3.11	2.70

In table 4.2, we list the hybridization indices of the C1 and C3 orbitals,  $\varphi$ . The C1 atom has two  $sp^2$  orbitals with 120° interorbital angle and one  $sp^{2.72}$ . The

latter gives rise to a partly buckled structure. The fourth C1 orbital has a large  $p$  contribution, indicating that it is close to a  $p_z$  orbital with little  $s$  contribution, and induces  $\pi$  bonding in the hexagonal rings. The C2 atoms have fourfold coordination and their hybridization should be close to  $sp^3$ . Due to geometric constraints, the bonds have strained angles[119]. Finally, the C3 atom has four quasi- $sp^3$  orbitals of which three are used for nearest-neighbor  $\sigma$  bonding. The electron in the fourth orbital remains unpaired and can give a local magnetic moment of  $1 \mu_B$  (Bohr magneton). There are two C3 atoms per unit cell which form a graphene-like subcrystal. The maximal magnetic moment per unit cell is therefore  $2\mu_B$  if the system is ferromagnetic. However, when we align these two magnetic moments antiparallel, the total energy is lowered by 12 meV per magnetic atom, which gives an AFM ground state.

In comparison to penta-graphene, ph-graphene has a 76 mev/atom lower formation energy. However, it is about 0.9 eV/atom higher than that of graphene. These results are consistent with the ones from Zhang *et al.* [205]. The relatively high formation energy of ph-graphene as compared to graphene can be mainly attributed to the “bent” bonds of the C2 atoms due to geometric constraints.

#### 4.3.4 Stability and electronic structure

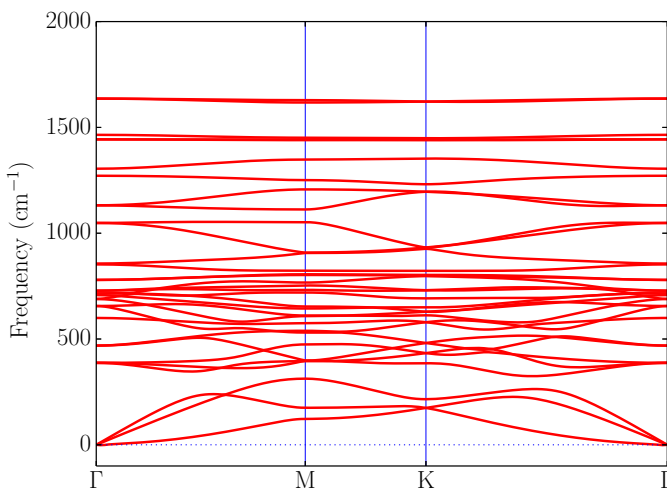


Fig. 4.14 Phonon dispersion relation of monolayer ph-graphene.

To check the dynamical stability of the ph-graphene structure we calculated its phonon spectrum (see Fig. 4.14). Since there are no imaginary frequencies, we can conclude that the structure is dynamically stable.

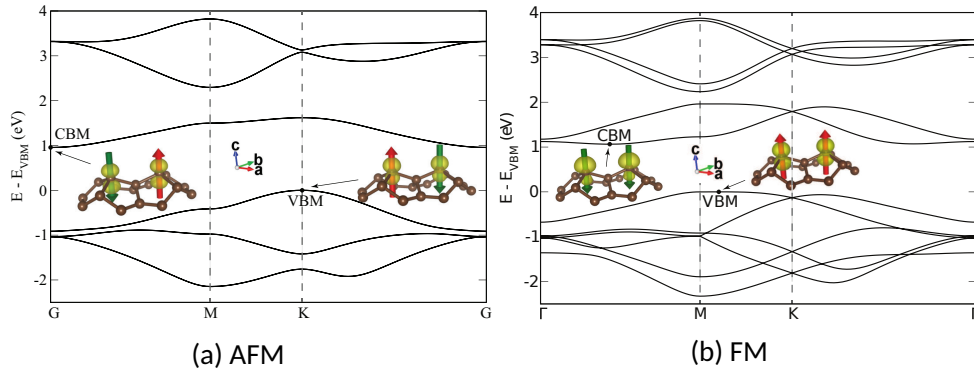


Fig. 4.15 Electronic band structure of monolayer ph-graphene. The charge densities at the VBM and CBM in the unit cell are shown as insets. The arrows on the atoms indicate the orientation of their magnetic moments.

The electronic band structure and the charge densities at the valence band maximum (VBM) and conduction band minimum (CBM) are shown in Fig. 4.15. Both the FM and AFM states exhibit indirect semiconducting character with a band gap (PBE) of 1.06 eV and 0.96 eV, respectively. The band edge states are mainly located on the magnetic atoms and the band gap separates states of opposite spin orientation. The hybridized  $\varphi_4$  states (see above) on these atoms form a  $\pi$  bonding network that resembles the  $p_z$   $\pi$  bonding in graphene. For the FM state, the typical graphene-like band structure that results from this can be observed for the valence and conduction bands. These bands are separated due to the ferromagnetic exchange splitting in spin-up and spin-down states with a large gap in between. Note that the splitting between bonding and anti-bonding states at the  $\Gamma$  point is strongly reduced with respect to graphene because of the larger interatomic distance separating the C3 atoms (3.1 Å in ph-graphene vs 1.4 Å in graphene). Due to this increased bonding distance, the exchange interaction exceeds the bonding interaction and the system is magnetic in stark contrast to graphene where the  $\pi$  bonding is much stronger.

### 4.3.5 Summary

In this work, we proposed a new type of stable monolayer carbon allotrope composed of pentagonal and hexagonal rings of carbon atoms. We explained the symmetry and the structure of the bonds that result in local magnetic moments. By comparing the total energy of the FM and AFM state, we conclude that the latter is the ground state. Our theoretical calculations give insight in the magnetic mechanism in this metal-free material, which can initiate further work on the exploration of magnetic properties of other 2D metal-free material. In the later chapter, we will see how strain can play an important role to modulate the magnetic ground state of this material.

## 4.4 Battery related properties of MXenes/graphene heterostructure<sup>4</sup>

### 4.4.1 Introduction

Lithium ion batteries (LIBs) are widely used for the electrochemical energy storage in electrical vehicles and portable electronic devices such as cell phones. In fact, the speed of the development in these state of the art products mostly hinges on the progress in battery technology. In current state, energy densities and rate capabilities of both LIBs and sodium ion batteries (NIBs) are insufficient to satisfy costumers' needs. Therefore, the demand for the metal based new generation batteries that have large reversible energy/power capacity, good cyclic stability and long life span is growing day by day. Recently, rechargeable batteries based on 2D materials have garnered great attention because of their promising potential as anode materials with enhanced gravimetric and volumetric energy densities which is a key challenge in current rechargeable ion battery technology. For instance Mo<sub>2</sub>C was shown to exhibit much better electrochemical properties in lithium-ion battery applications,[mo2c-ref8, mo2c-ref10]. Moreover, other 2D layered materials such as transition metal dichalcogenides,[mo2c-ref11, mo2c-ref12], black phosphorus[mo2c-ref18, mo2c-ref20], and MXenes (with M = Ti, V, Nb, Mo and X = C, N)[mo2c-ref13, mo2c-ref17] were also widely investi-

<sup>4</sup>This work will be published as: P9.

gated because of their high energy storage density and high rate capacity. However, experimental studies have shown that single type layered nanosheets inevitably restack during the cycling process, resulting in a rapid capacity fading and poor rate performance.

Therefore, current interest has been directed towards heterostructured[206, 207] 2D materials. A plausible design of vertical heterostructures from different 2D materials is expected to be beneficial for providing rapid electron transport and the acceleration of cation transport in the electrodes, and thus expected to improve the rate performance in current battery technology[207]. In addition, the negligible volumetric changes of in particular TMDCs and MXenes under lithiation/de-lithiation processes, such that there is only 5% in-plane lattice expansion in the  $\text{Mo}_2\text{C}$  lattice caused by Li intercalation[208], can minimize the intrinsic volumetric changes during charging/discharging processes and prolongs cycling lifetime of the rechargeable batteries. Also, combining different 2D materials is a promising way to adjust the interlayer distance to accommodate much larger ( $\text{Na}^+$ ) and more polarized ( $\text{Mg}^{2+}$ ) ions. For instance, lithium-ion capacity in excess of  $750 \text{ mAh g}^{-1}$ [209] has already been demonstrated for the batteries with MXene flakes electrodes, optimized with CNTs.

To this end, we systematically investigated Li intercalation in vertical (van der Waals) heterostructures of MXenes and graphene for rechargeable battery applications. We only considered functionalized MXenes with OH and O, since the experimentally synthesized MXenes are often functionalized with various radicals due to the mainly used chemical exfoliation process in synthesis. In addition, MXenes with low formula weights, such as  $\text{Ti}_2\text{C}$ ,  $\text{Nb}_2\text{C}$ ,  $\text{V}_2\text{C}$  and  $\text{Sc}_2\text{C}$  have been found to be most promising[210] materials for battery allocations due to their theoretically stated gravimetric capacity, which represents the amount of charge that can be stored per gram of material. Therefore, we considered only  $\text{M}_2\text{CX}_2$  (where M=Sc, Ti, V and X=OH, O) monolayers in this study.  $\text{V}_2\text{CX}_2$  is particularly important since it shows the highest  $\text{Li}^+$  capacity of all MXenes tested under similar conditions[211]. Another advantageous is that, compared to bilayer  $\text{M}_2\text{CX}_2$ ,  $\text{M}_2\text{CX}_2$ /graphene heterostructure has much smaller weight, offering much larger storage capacity.

We introduce the following nomenclatures in the following sections: M stands for the transition metal in MXenes; X stands for the functionalized group, i.e. OH

or O; Gr stands for graphene; Li is intercalated Li atom (unless the concentration is stated it means only single Li atom intercalation); Monolayer and bilayer are denoted with mono- or bi- prefixes; For instance: bi-Ti<sub>2</sub>CO<sub>2</sub>+Li stands for bilayer Ti<sub>2</sub>CO<sub>2</sub> with a single Li atom intercalation, and Ti<sub>2</sub>CO<sub>2</sub>+Gr+Li stands for heterostructure of Ti<sub>2</sub>CO<sub>2</sub> on graphene with a single Li atom intercalation.

#### 4.4.2 Computational details

The physical properties of the considered systems were obtained by Density Functional Theory based simulations as implemented in the Vienna *ab initio* Simulation Package (VASP) [110, 111, 212, 213]. In these simulations, a plane-wave basis set with a 500 eV energy cut-off, the projected augmented wave (PAW) potentials[PAW2, 106] with the generalized gradient approximation (GGA) within the Perdew-Burke-Ernzerhof (PBE) formulation [97, 214], and a  $7 \times 7 \times 1$  up to  $11 \times 11 \times 1$   $\mathbf{k}$ -points mesh were used depending on the size of the supercell. Since we dealt with weakly interacting systems, weak van der Waals interactions were taken into account using DFT-D3 method Grimme *et al.* [215] including Becke-Jonson damping. Lattice vectors perpendicular to the 2D plane were fixed as 30 Å for all the simulations. A  $10^{-5}$  eV energy and a  $10^{-3}$  eV/Å force convergence criteria were set to achieve the ground state structure and its energy. Charge transfer between Li atom and the host systems were calculated via Bader analysis [216–219].

We calculated diffusion barriers for Li ions using the climbing-image nudged elastic (cNEB) method as implemented in the VASP transition state tools[220, 221]. The cNEB method is an efficient method to determine the minimum energy diffusion path between two given positions. We used at least 7 images, including initial and final positions, for cNEB calculations. The atomic positions and energy of the images were then relaxed until the largest norm of the force orthogonal to the path is smaller than 0.01 eV/Å.

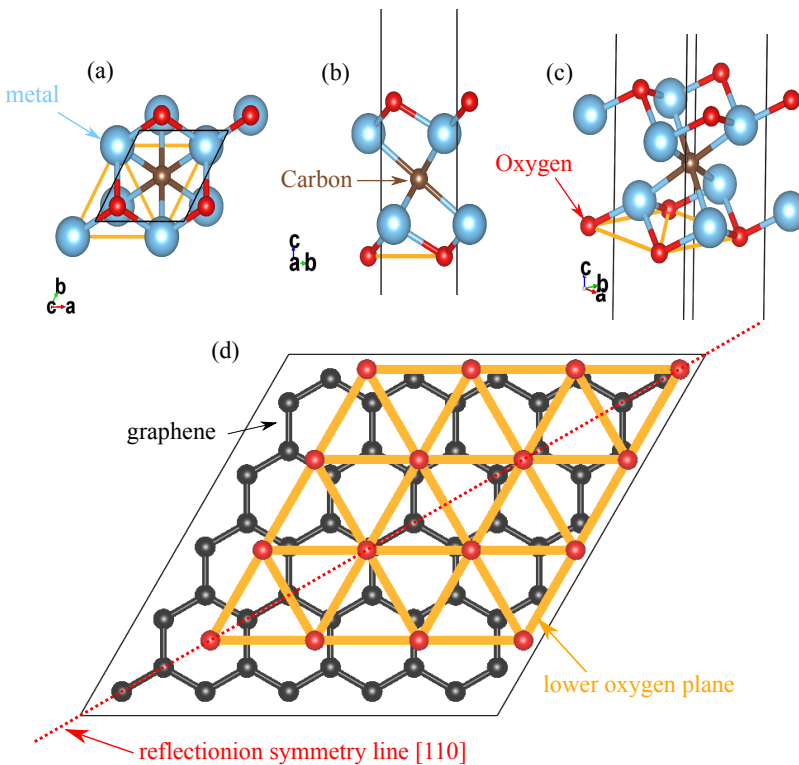


Fig. 4.16 An example structure of mono-Ti<sub>2</sub>CO<sub>2</sub> presenting in (a) top view, (b) side view and (c) tilted view. (d) Simplified example structure of M<sub>2</sub>CX<sub>2</sub>+Gr heterostructure in ground state stacking.

#### 4.4.3 Results

##### heterostructure stacking types

First of all, we need to construct the heterostructure. To minimize the lattice mismatch between layers, we constructed the heterostructures with a 3×3 supercell of Sc<sub>2</sub>CO<sub>2</sub> or Sc<sub>2</sub>C(OH)<sub>2</sub> with a 4×4 supercell of graphene, a 4×4 supercell of Ti<sub>2</sub>CO<sub>2</sub> or Ti<sub>2</sub>C(OH)<sub>2</sub> with a 5×5 supercell of graphene, and a 5×5 supercell of V<sub>2</sub>CO<sub>2</sub> or V<sub>2</sub>C(OH)<sub>2</sub> with a 6×6 supercell of graphene, see Fig. 4.16 as a representative example. In order to find out the ground state stacking type of M<sub>2</sub>CX<sub>2</sub>+Gr heterostructures, we calculated the binding energy of possible stacking configurations by shifting the M<sub>2</sub>CX<sub>2</sub> layer over the unit cell of graphene on a uniform mesh, see the supplementary materials<sup>†</sup> for details. In the course of these sim-

ulations, each layer in the heterostructure is regarded rigid where only the interlayer distance is allowed to relax. The regarded binding energy per atom,  $E_b$  was calculated as follows:

$$E_b = \frac{1}{N} [E(\text{M}_2\text{CX}_2 + \text{Gr}) - E(\text{M}_2\text{CX}_2) - E(\text{Gr})] \quad (4.5)$$

where  $E(\text{M}_2\text{CX}_2 + \text{Gr})$ ,  $E(\text{M}_2\text{CX}_2)$  and  $E(\text{Gr})$  are the total energies of  $\text{M}_2\text{CX}_2 + \text{Gr}$ , mono- $\text{M}_2\text{CX}_2$  and  $\text{Gr}$ , respectively.  $N$  is the total number of atoms in the system. In Table 4.3, the calculated  $E_b$  and the interlayer distance for  $\text{M}_2\text{CX}_2 + \text{Gr}$  are given, and they are system dependent. The results for graphene bilayer are also given for a reference. The interlayer binding energy and the distance of bilayer graphene are 20 meV/atom and 3.325 Å, respectively. Our calculations agree very well with a recent work in which quantum Monte Carlo simulations predicted a 17.8 meV/atom binding energy and 3.384 Å interlayer separation for bilayer graphene[222]. The calculated binding energies (i.e.  $E_b$ ) are negative for all the considered heterostructures, demonstrating the stability of each system against the phase separation. The magnitudes of the  $E_b$  for the ground states stacking in MXene oxides/graphene are comparable to that of bilayer graphene, whereas the hydroxides/graphene are slightly stronger bonded due to the extra hydrogen bonds. The differences in the binding energies among different MXenes that have the same functionalized group are negligible.

### Single Li intercalation and its binding energy

Having the ground state stacking types of all the  $\text{M}_2\text{CX}_2 + \text{Gr}$  heterostructures, we now investigate the Li intercalation in these systems. To uncover potential of  $\text{M}_2\text{CX}_2 + \text{Gr}$  heterostructures in battery applications, we also considered Li intercalation on mono- $\text{M}_2\text{CX}_2$ , within bi- $\text{M}_2\text{CX}_2$  and within bi- $\text{Gr}$  reference systems. These systems are considered the same dimensions, or equivalently the same Li atoms concentration, as in the corresponding heterostructures.

Previous studies[223–225] have pointed out that the strongest binding for the Li atoms intercalated happens between bilayer heterostructure and reported a non-binding character of Li atoms on the surface of few-layer graphene, therefore, in this study, we limited our study considering only the intercalation between  $\text{M}_2\text{CX}_2$  and graphene. In addition, inspired by the previous study[226] for

Table 4.3 A comparison of different MXenes systems: monolayer, bilayer, heterostructure.  $d$  is the interlayer distance and is defined as shown in Fig. 4.17.  $E_b$  is binding energy of the system with respect to its components, e.g bilayer with respect to monolayers. Only the ground state stacking of  $M_2CX_2+Gr$  is reported.

Material	Structure	$d$ Å	$E_b$ eV/atom
graphene	bi-Gr (AB)	3.277	-0.024
	bi-Gr (AA)	3.325	-0.020
$Sc_2CO_2$	bi- $Sc_2CO_2$	2.294	-0.029
	$Sc_2CO_2+Gr$	3.067	-0.022
$Sc_2C(OH)_2$	bi- $Sc_2C(OH)_2$	0.598	-0.025
	$Sc_2C(OH)_2+Gr$	2.191	-0.027
$Ti_2CO_2$	bi- $Ti_2CO_2$	2.396	-0.027
	$Ti_2CO_2+Gr$	3.000	-0.018
$Ti_2C(OH)_2$	bi- $Ti_2C(OH)_2$	0.399	-0.024
	$Ti_2C(OH)_2+Gr$	2.097	-0.034
$V_2CO_2$	bi- $V_2CO_2$	2.394	-0.025
	$V_2CO_2+Gr$	2.867	-0.022
$V_2C(OH)_2$	bi- $V_2C(OH)_2$	0.398	-0.011
	$V_2C(OH)_2+Gr$	2.779	-0.035

the Li absorption site in  $M_2CX_2$  multilayer system, we discovered that intercalated Li atom bound close to the  $M_2CX_2$  layer and far from graphene, and it resides itself between three O atoms, therefore each formula unit of  $M_2CX_2$  in heterostructure can accommodate one Li atom. Additional Li atoms occupy same positions in other unit cells, as shown in Fig. 4.18. Note that, because of resulted reflection symmetry for ground state stacking, Li position only on one side of the symmetry line [110] is studied for a single Li absorption. Since a strong binding between Li and  $M_2CX_2+Gr$  bilayer is necessary to avoid the formation of metallic lithium, and therefore to improve the safety and reversibility of lithium-ion batteries, we need to make sure the reported Li binding energy is the largest one (that it is associated to the ground state adsorption site). Thus, we have

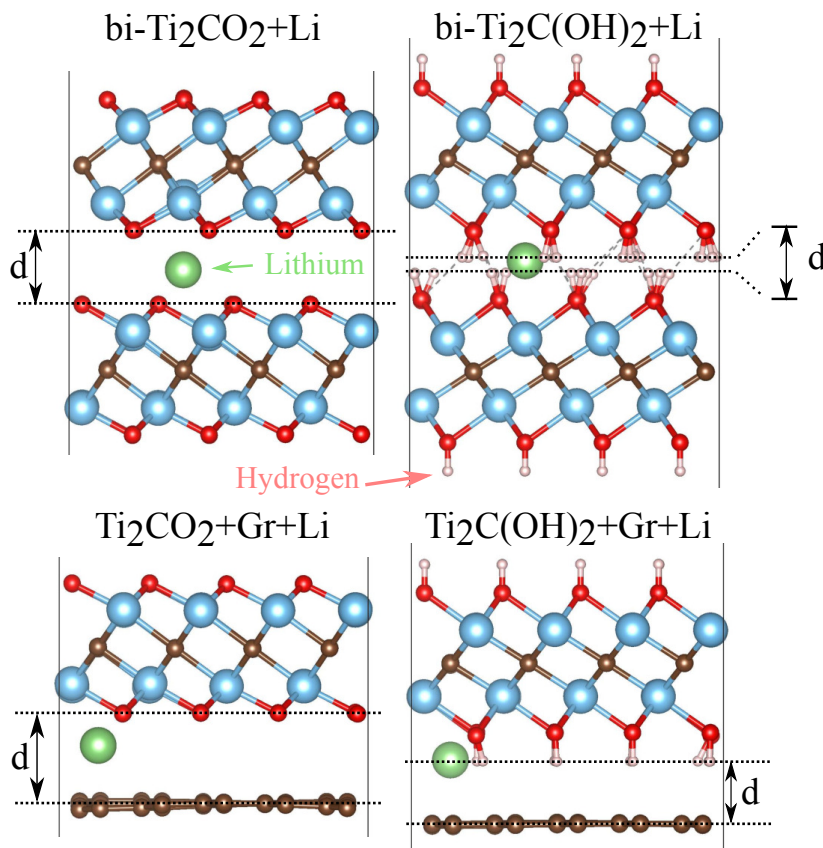


Fig. 4.17 The optimized locations of single Li atoms in different structures and the definition of interlayer distance  $d$ , which ignores the Li atom layer..

calculated all the possible adsorption sites between two layers, see the supplementary materials<sup>†</sup> for details.

The binding energy,  $E_b^{Li}$ , for Li intercalated systems is defined through the following equation:

$$E_b^{Li} = \frac{1}{x}[E(\text{with } x\text{Li}) - E(\text{without Li}) - xE(\text{Li})], \quad (4.6)$$

where  $E(\text{with } x\text{Li})$  and  $E(\text{without Li})$  are the total energies of system with and without  $x$  Li atoms, respectively.  $E(\text{Li})$  is the total energy of a Li atom in its most stable bcc bulk structure. Here, a more negative binding energy indicates a more favourable exothermic binding of Li.

In Table 4.4, the results for different materials in three promising systems are shown. For comparison, we calculated Li intercalation in AA and AB stacked

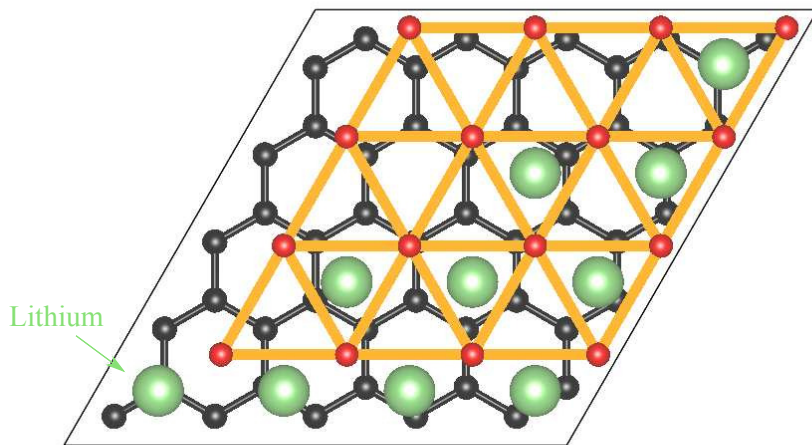


Fig. 4.18 The locations of Li atoms intercalation between  $\text{Ti}_2\text{CO}_2+\text{Gr}$  heterostructure as an example.

graphene bilayers. While the latter is more stable than the former for the pristine systems, the former is energetically more favourable for Li intercalation, consistent with previous calculations[227], see table 4.4. The  $\text{LiC}_{64}$  ( $4\times 4$  bilayer graphene) in AA configuration is energetically favorable to accommodate single Li between bilayer, while the Li atom will not bind at all in AB stack bilayer. However, the magnitude of binding energy generally is small as compared to the heterostructure due to the strong interaction of Li with  $\text{M}_2\text{CO}_2$  layer.

The following findings are concluded from the results: (1) All systems related to  $\text{Sc}_2\text{CO}_2$  experience severe structural distortion upon Li interactions. Two or three of the C atoms in the  $\text{Sc}_2\text{CO}_2$  moving towards each other and showing the tendency to cluster. Therefore, this type of system is unstable for Li intercalation. (2) The binding of Li atom on mono- $\text{M}_2\text{C(OH)}_2$  is not favorable. This can be attributed to the Columbic repulsion between positively charged Li ion and H atoms. (3) As going from mono- to bi- $\text{M}_2\text{C(OH)}_2+\text{Li}$ , Li adsorption is made stable again through the van der Waals interaction that competes with foregoing repulsive interaction. (4) mono- $\text{M}_2\text{CO}_2+\text{Li}$ , bi- $\text{M}_2\text{CX}_2+\text{Li}$  and  $\text{M}_2\text{CX}_2+\text{Gr}+\text{Li}$  exhibit the strongest adsorption for Li atoms. The calculated  $E_b^{Li}$  value at the largest binding energy site is -1.87 eV/atom for the mono- $\text{Ti}_2\text{CO}_2$  and -2.97 eV/atom for the mono- $\text{V}_2\text{CO}_2$ . In the case of  $\text{M}_2\text{CX}_2+\text{Gr}+\text{Li}$ , we observed that  $E_b^{Li}$  slightly decreases for M=Ti and V and X=O. This may be correlated to the reduced van der Waals interaction with respect to the pristine bilayers due to the increase in inter-

layer separation. (5) We have identified three promising candidates with large Li atom adsorption energy, namely  $\text{Sc}_2\text{C}(\text{OH})_2+\text{Gr+Li}$ ,  $\text{Ti}_2\text{CO}_2+\text{Gr+Li}$  and  $\text{V}_2\text{CO}_2+\text{Gr+Li}$ . Therefore, for the rest of the paper, we will focus on these three systems and will study the kinetics of Li diffusion.

### Effect of Li concentration

As a next step, we investigated the effect of the Li ion concentration on the physical properties of  $\text{M}_2\text{CX}_2+\text{Gr+Li}$  heterostructures. Here, the concentration is defined as the ratio of the number of Li atoms and the number of formula unit of  $\text{M}_2\text{CX}_2$  in the heterostructures (e.g. 100% corresponds to one Li atom for each formula unit). Fig. 4.19(a) shows the variation of average  $E_b^{Li}$  as a function of concentration of the Li ions (i.e.  $x$ ). As the number of intercalated Li increases, average  $E_b^{Li}$  decreases gradually. The reduction in binding energy is due to two main factors; One is the weak electrostatic attraction between  $\text{M}_2\text{CX}_2+\text{Gr}$  host and Li cations, and the other one is the enhanced Li-Li repulsion at high Li concentrations. The former is correlated with the reduction of charge transfer from the Li atom to  $\text{M}_2\text{CX}_2+\text{Gr}$  complex at high concentrations, as shown in Fig. 4.19(b). Similarly, the latter is due to the reduction of interatomic distances between positively charged Li ions. Above a critical concentration value, namely 80%,  $E_b^{Li}$  becomes positive for  $\text{Sc}_2\text{C}(\text{OH})_2+\text{Gr+Li}$ , making this system energetically unstable for further Li insertion.  $E_b^{Li}$  is always negative for  $\text{Ti}_2\text{CO}_2+\text{Gr+Li}$  and  $\text{V}_2\text{CO}_2+\text{Gr+Li}$ , suggesting that these heterostructures are stable against Li intercalation, and thus we can safely disregard the phase separation into individual monolayers and bulk Li at high concentrations. In other words, the  $\text{Ti}_2\text{CO}_2+\text{Gr+Li}$  and  $\text{V}_2\text{CO}_2+\text{Gr+Li}$  structures has high stability even with high Li concentration. For  $\text{V}_2\text{CO}_2+\text{Gr+Li}$  ( $\text{Ti}_2\text{CO}_2+\text{Gr+Li}$ ),  $E_b^{Li}$  may vary by about 1 (0.5) eV as a function of Li concentration. Recently, Sun *et al.* Sun *et al.* [228] reported that  $\text{V}_2\text{CO}_2$  undergoes a reversible structural transformation during the adsorption of Li. We also checked the possibility of such structural transformation for  $\text{V}_2\text{CO}_2+\text{Gr}$  bilayer and we found that presence of graphene prevents the transformation of  $\text{V}_2\text{CO}_2$ . Our results clearly demonstrated that  $\text{Ti}_2\text{CO}_2+\text{Gr+Li}$  and  $\text{V}_2\text{CO}_2+\text{Gr+Li}$  can be utilized as an anode material for high capacity Li ion batteries.

Another important point is how the structural stability of  $\text{Ti}_2\text{CO}_2+\text{Gr+Li}$  and  $\text{V}_2\text{CO}_2+\text{Gr+Li}$  is affected as the Li ions coverage is increased. We found that

an increase in the number of Li ions leads to a small expansion in in-plane lattice constants. For instance, the in-plane lattice constant of both  $\text{V}_2\text{CO}_2+\text{Gr+Li}$  and  $\text{Ti}_2\text{CO}_2+\text{Gr+Li}$  expands less than 1%. Besides, we did not observe severe lengthening of the surface Ti/V-O bonds and shortening of Li-O bonds for both  $\text{Ti}_2\text{CO}_2+\text{Gr+Li}$  and  $\text{V}_2\text{CO}_2+\text{Gr+Li}$  heterostructures. For instance, Li-O bond length decreases at most 3% with increasing Li concentration. It is also found that Li intercalation slightly enlarges and later reduces the interlayer separation as Li concentration increased. The calculated interlayer separations suggested that we can have at most 0.5 Å expansion as a result of Li intercalation. These results clearly suggest that we can have a reversible reaction that is requested for rechargeable ion batteries. Thus, the layered  $\text{M}_2\text{CX}_2+\text{Gr}$  heterostructures can effectively defy the volume expansion problem faced by the electrode materials. However,  $\text{Sc}_2\text{C(OH)}_2+\text{Gr}$  is unstable against Li loading to higher concentration.

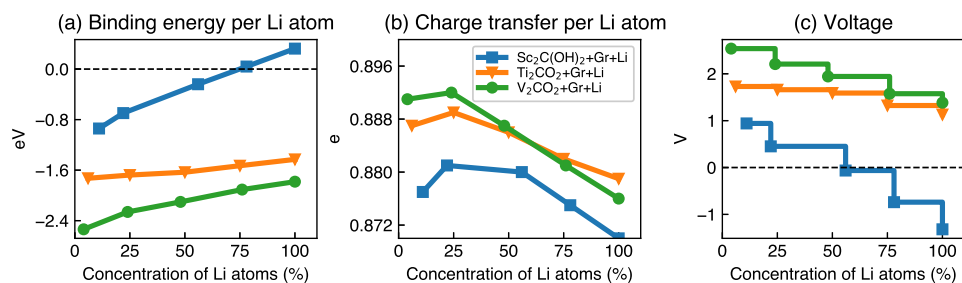


Fig. 4.19 The average binding energy (a) and the average charge transfer (b) of Li atoms and the voltage profile of  $\text{M}_2\text{CX}_2+\text{Gr}$  heterostructure as a function of Li concentration.

### Electrochemical properties

In order to gain insight into the electrochemical properties of the Li intercalation process into  $\text{M}_2\text{CX}_2+\text{Gr}$  heterostructure, the open-circuit-voltage was obtained by calculating the averaged half cell voltage over a range of metal ion concentrations  $x$ , where  $x_1 \leq x \leq x_2$ , using,

$$V \approx \frac{E_{\text{M}_2\text{CX}_2+\text{Gr}+x_1\text{Li}} - E_{\text{M}_2\text{CX}_2+\text{Gr}+x_2\text{Li}} + (x_2 - x_1)E_{\text{Li}}}{(x_2 - x_1)e} \quad (4.7)$$

where  $E_{M_2CX_2+Gr+Li_{x_1}}$  and  $E_{M_2CX_2+Gr+Li_{x_2}}$  are the total energies of  $M_2CX_2+Gr$  heterostructure with  $x_1$  and  $x_2$  Li intercalated, respectively.  $E_{Li}$  is the total energy of bulk bcc Li. First of all, our calculations showed that the charging voltage for Li intercalation decreases with increase of Li atoms, as clearly seen in Fig. 4.19(c). The calculated average voltage corresponding to  $Sc_2C(OH)_2+Gr+Li$  is negative for the Li ion concentration  $x$  larger than 55%. As mentioned above, a phase transition should be expected for the concentrations larger than this critical value. Our results are consistent with a recent work reporting that H and/or OH should be avoided if possible since they result in a lower capacity and negative cell voltage[229, 230]. On the other hand, the available intercalation sites in  $Ti_2CO_2+Gr+Li$  and  $V_2CO_2+Gr+Li$  composites can be fully occupied. As we increase the Li concentration from  $x=50\%$  to 100%, the open-circuit voltage decreases from 1.59 (1.94) V to 1.13 (1.38) V for  $Ti_2CO_2+Gr+Li$  ( $V_2CO_2+Gr+Li$ ). The binding energy change (i.e  $E_b^{Li}$ ) during Li intercalation can be correlated with the voltage value. Since  $V_2CO_2+Gr+Li$  has the largest Li binding energy, the calculated voltage value is also the largest. The calculated average voltage profile is 1.49 V for  $Ti_2CO_2+Gr+Li$  and 1.93 V for  $V_2CO_2+Gr+Li$ , which are higher than those of  $Mo_2C$ [208], graphite[231] and  $TiO_2$  electrode [232] and lower than phosphorene[233]. Experimentally measured maximum voltages for pure  $V_2CO_2$  and  $Ti_2CO_2$  anodes are 3.0 V and 2.5 V, respectively[210, 234]. Combining graphene with  $V_2CO_2$  or  $Ti_2CO_2$  reduces maximum voltages by around 0.5 V. Approximately 50% of capacity of  $V_2CO_2+Gr+Li$  ( $Ti_2CO_2+Gr+Li$ ) is intercalated above 2 (1.6) V, with the rest intercalating at lower voltages. Our results clearly demonstrate that  $Ti_2CO_2+Gr+Li$  can be exploited in low voltage applications and  $V_2CO_2+Gr+Li$  are suitable for high charging voltage applications.

### Diffusion properties

A low diffusion barrier and high mobility are the requirements of an efficient electrode material. In particular, the mobility of a metal atom on an electrode material is a key factor determining the rate performance during charging and discharging of a battery. Following the thermodynamic consideration of Li intercalation, we investigated the single Li kinetics on mono-M+Li, within bi-M+Li and within M+Gr+Li heterostructures, where here M=( $Sc_2C(OH)_2$ ,  $Ti_2CO_2$ ,  $V_2CO_2$ ), by calculating the lowest energy Li atom diffusion path connecting two adjacent

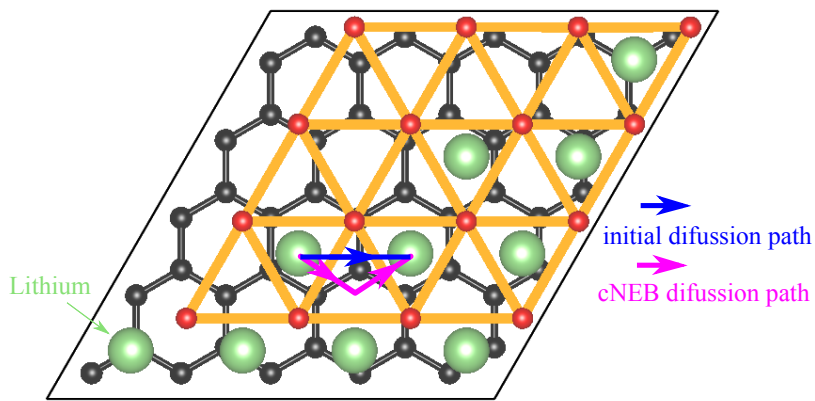


Fig. 4.20 Initial guessed and final resulted Lithium diffusion paths between  $\text{Ti}_2\text{CO}_2+\text{G}$  heterostructure as an example.

binding sites using cNEB method, see Fig. 4.21. The determined energy profiles of the paths are shown in Fig. 4.22. Compared to the bilayer systems, Li displays relatively smaller diffusion barriers on the pristine monolayers. In other words, energy barriers of Li ions in  $\text{M}_2\text{CX}_2+\text{Gr}+\text{Li}$  heterostructure are always higher than those of monolayers. For instance, while energy barriers is calculated as 0.16 eV on the mono- $\text{V}_2\text{CO}_2+\text{Li}$ , it is obtained as 0.6 eV for bi- $\text{V}_2\text{CO}_2+\text{Li}$  and  $\text{V}_2\text{CO}_2+\text{Gr}+\text{Li}$  heterostructure. Since the multilayer system has the advantage of having higher capacity than the single monolayer system in given volume, and also the synthesized  $\text{M}_2\text{CX}_2+\text{Gr}$  will mostly be multilayered, we believe that the monolayer structures represent the lower limit for energy barriers. However, to obtain realistic kinetics properties we should consider diffusion of ions between layers not only on isolated monolayers. Another important point is that surface functionalization increases the barrier remarkably[235]. Interestingly, energy barriers for Ti based systems are similar, varying in the range of 0.22-032 eV. Our calculated energy barriers for mono- $\text{Ti}_2\text{CO}_2+\text{Li}$  is consistent with a recent work[235]. Energy barriers for Ti-based systems are lower than that of graphite (0.5 eV)[236] and high-capacity bulk silicon anode materials with a diffusion barrier around 0.57 eV, comparable to the commercially used anode materials based on  $\text{TiO}_2$ .

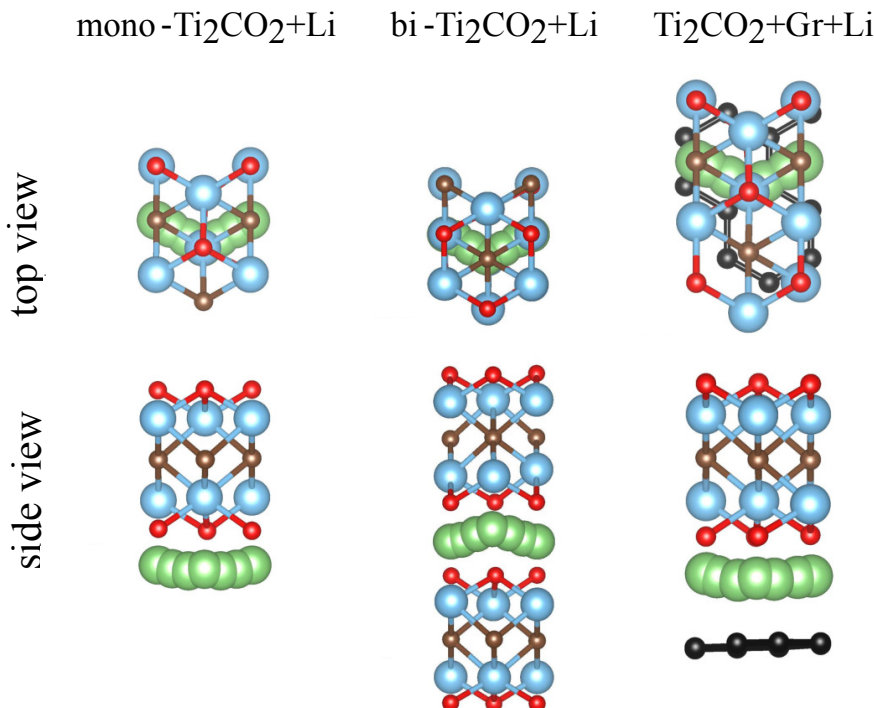


Fig. 4.21 The top view and the side view of Li diffusion paths along the lowest energy diffusion paths in Ti<sub>2</sub>CO<sub>2</sub> related systems as examples.

with a barrier of 0.35–0.65 eV[237–239], suggesting that heterostructures of Ti-based MXenes with graphene are promising candidates for electrode materials in battery applications. The diffusion barriers can be reduced by weakening the interaction of Li ions with the constituent layers. This can be achieved by fabricated pillar structures in which the interlayer distance of graphene and MXenes is enlarged by the help of intercalated molecules [240]. This method can also improve the storage capacity by multilayer absorption between the layers.

#### 4.4.4 Conclusion

We carried out first-principles calculations to systematically investigate the Li atoms intercalation in MXenes/graphene vertical bilayer heterostructure for Li battery application. Six members in Mxenes family were chosen to form heterostructures with graphene: M<sub>2</sub>CX<sub>2</sub>+Gr (where M=Sc, Ti, V and X=OH, O). The ground state stacking types of bilayer and the strongest binding sites of Li atoms are determined first. The strength of the binding of bilayer heterostructure is

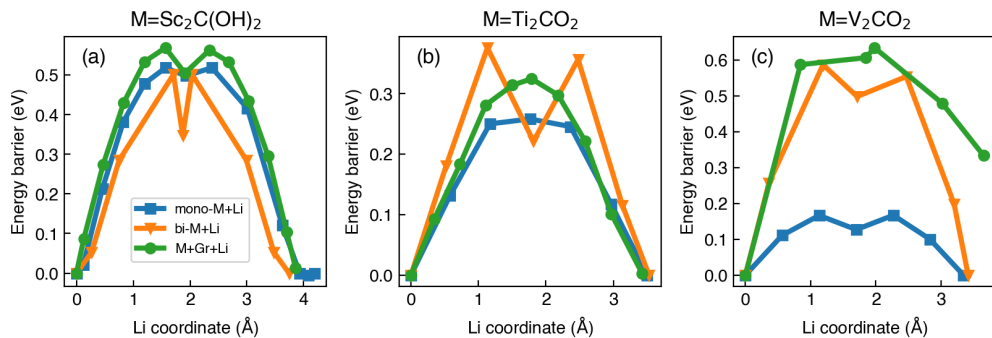


Fig. 4.22 Energy profiles of the Li diffusions in different systems composed of (a)  $\text{Sc}_2\text{C}(\text{OH})_2$ , (b)  $\text{Ti}_2\text{CO}_2$  and (c)  $\text{V}_2\text{CO}_2$  along the lowest energy diffusion paths as indicated in Fig. 4.21.

comparable to that of bilayer graphene, and it is stronger than MXenes bilayers. Due to a finite mismatch of lattice constant of MXenes and graphene, relative motion of bilayer in heterostructure require less energy as compared with the other two cases and giving low friction between them. We identified two promising heterostructure for Li intercalation:  $\text{Ti}_2\text{CO}_2+\text{Gr}$  and  $\text{V}_2\text{CO}_2+\text{Gr}$ . The stability of the heterostructure upon Li intercalation is confirmed through 1) small variations of the structural parameters , e.g. in-plane lattice parameters ( $<1\%$ ) and interlayer separation ( $<0.5 \text{ \AA}$ ); 2) Large negative binding energies of Li atoms, e.g. larger than that in bilayer graphene; 3) Li atom donates a significant amount of charge to the host materials and exists in the cationic state. We found that all possible Li absorption sites can be occupied without destroying stability, namely 100% Li intercalation, leading an average open circuit voltage of 1.49 V for  $\text{Ti}_2\text{CO}_2+\text{Gr}$  and 1.93 V for  $\text{V}_2\text{CO}_2+\text{Gr}$ . Especially,  $\text{Ti}_2\text{CO}_2$  MXene offers a compromise between capacity and kinetics since the calculated diffusion barriers are the lowest among other systems studied and lower than that of graphene. It is suggested from the study that a balance between the storage capacity and kinetics for practical applications should be made when selecting a promising candidate. Due to their lower molecular weights as compared to bare MXenes bilayers, MXene+Gr heterostructure offer higher storage density, they also have the advantage of their good electrical conductivity which is an essential property for a proper operation of a battery.

#### **4.4.5 Principle of Lithium battery**

#### **4.4.6 Key quantities and their modelling**

Table 4.4 A comparison of different MXenes systems: monolayer, bilayer, heterostructure with Li intercalation.  $d$  is the interlayer distance and is defined as shown in Fig. 4.17.  $E_b^{Li}$  is the binding energy of a single Li atom. Only the largest binding energy of Li atom is reported, i.e. ground state adsorption site.  $L_{min}$  is the shortest bond length of a Li atom with others.  $e$  is the charge transfer from a Li atom to a heterostructure. For the consistence of the Li concentrations, all monolayer and bilayer system use the same dimensions as in the corresponding heterostructures. Three different size of bi-Gr are presented to compare with the hereostructures with corresponding size of Gr.

Material	Structure	$d$ Å	$E_b^{Li}$ eV/atom	$L_{min}$ Å	Li charge transfer $e$
graphene	4×4 bi-Gr (AB)+Li	3.591	0.030	2.060	0.873
	4×4 bi-Gr (AA)+Li	3.616	-0.232	2.344	0.868
	5×5 bi-Gr (AA)+Li	3.617	-0.283	2.344	0.878
	6×6 bi-Gr (AA)+Li	3.636	-0.336	2.352	0.879
	mono- $\text{Sc}_2\text{CO}_2+\text{Li}$	-	-9.986	2.024	0.898
	bi- $\text{Sc}_2\text{CO}_2+\text{Li}$	1.791	-32.646	2.208	0.902
$\text{Sc}_2\text{C(OH)}_2$	mono- $\text{Sc}_2\text{C(OH)}_2+\text{Li}$	-	0.048	1.918	0.869
	bi- $\text{Sc}_2\text{C(OH)}_2+\text{Li}$	0.548	-0.309	2.050	0.885
	mono- $\text{Sc}_2\text{C(OH)}_2+\text{Gr+Li}$	-2.078	-0.941	1.953	0.877
	mono- $\text{Ti}_2\text{CO}_2+\text{Li}$	-	-1.870	1.994	0.912
	bi- $\text{Ti}_2\text{CO}_2+\text{Li}$	2.480	-2.308	2.047	0.886
$\text{Ti}_2\text{C(OH)}_2$	mono- $\text{Ti}_2\text{C(OH)}_2+\text{Li}$	-	0.146	1.926	0.792
	bi- $\text{Ti}_2\text{C(OH)}_2+\text{Li}$	0.599	-0.431	2.004	0.879
	mono- $\text{Ti}_2\text{C(OH)}_2+\text{Gr+Li}$	-2.090	-0.229	1.941	0.875
	mono- $\text{Ti}_2\text{C(OH)}_2+\text{Gr}$	-2.791	-1.975	0.921	0.875



# **Chapter 5**

## **Results of Physical Properties Modification in Novel 2D materials**

This is the second part of the results of this thesis. Here we will discuss some of the possible ways to modify the physical properties of 2D materials. As before, each section will be focused on an unique way to change the properties of materials, namely number of layers, mechanical strain, adatom adsorption, heterostructure and defect induction. In consist with the theme of the thesis, which is about novel 2D materials, we will continue to introduce other new 2D that has been discovered and whose properties will be modified. Some of the studies here are the continuum of the works in the previous chapter where properties are determined only, here those properties will be modified.

### **5.1 Number of layers**

#### **5.1.1 Few-layer of Calcium hydroxide<sup>1</sup>**

##### **Introduction**

We have seen several monolayer systems that exacted from layered materials such 2D-BN, 2D-MoS<sub>2</sub>, in this work, we further explore this process for alkaline earth metal hydroxides (AEMHs), which pose a layered structure in the bulk form. It was exfoliated to few-layer, the experiment and the theoretical modelling is

---

<sup>1</sup>This work is published in: P5.

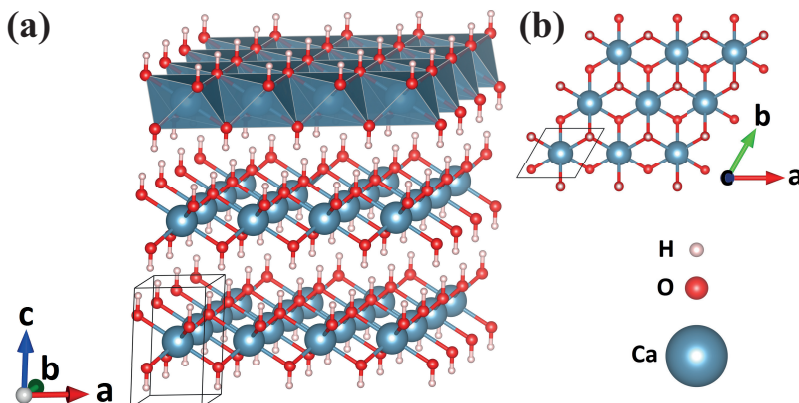


Fig. 5.1 Atomic structure of bulk  $\text{Ca}(\text{OH})_2$ : (a) tilted view, (b) top view of one layer.

reported in this section. In contrast to the abundant literature on graphenelike ultra-thin structures, few-layer AEMHs have not been investigated so far. Bulk forms of AEMHs are layered structures belonging to the  $P\bar{3}m1$  space group[241] and the crystal structure of a layered AEMHs comprises stacked sheets of  $\text{MO}_6$  ( $\text{M}$ =alkaline earth metals) edge-sharing octahedra, see Fig. 5.1. At each corner of an octahedron, each O atom binds one H atom and the latter interacts with three neighboring hydroxyl groups of the adjacent layer. Early studies on bulk AEMHs revealed that the application of temperature and pressure may result in dramatical changes in their crystal structure and their electronic properties[242-249]. Moreover, early theoretical studies showed the reliability of the use of first principle calculations with a plane-waves basis set in combination with the generalized gradient approximation exchange-correlation functional for the investigation of structural and electronic properties of these materials[250-253].

Although the structural and electronic properties of bulk AEMHs have been investigated before [252, 254, 255], single layers of these materials have never been studied before and their stability is still an open question. However, advances in experimental techniques made exfoliation and growth of such structures possible[256, 257]. Especially the Portlandite material,  $\text{Ca}(\text{OH})_2$ , which has been the main product of hydration of Portland cement,  $\text{CaO}$ , is one of the most well-known AEHMs, characteristic properties of ultra-thin structures of Portlandite have not been reported yet. In this study we investigate, both experimentally and theoretically, the structural, electronic, magnetic, vibrational

and mechanical characteristics of bulk, bilayer and monolayer Ca(OH)<sub>2</sub> and discuss how these properties change with the number of layers. Particularly, the result of the phonon calculation is presented for the confirmation of the stability of the newly proposed 2D material.

To assess the mechanical strength of the material, in addition to the elastic moduli that we have introduced in chapter 3, here we calculate another useful parameter that closely related to the Young's modulus, which is called the in-plane stiffness of the materials. We focused on the harmonic range of the elastic deformation, where the structure responded linearly to strain  $\epsilon$ . The stretching of the Ca(OH)<sub>2</sub> is achieved by increasing the equilibrium lattice constant  $a_0$  by  $\Delta a$ , to attain the axial strain  $\epsilon = \Delta a/a_0$ . We optimized the atomic structure at each increment of the strain,  $\Delta\epsilon = 0.01$  and calculated the total energy under strain  $E_T(\epsilon)$ . Then the strain energy can be given by,  $E_S = E_T(\epsilon) - E_T(\epsilon=0)$ ; namely, the total energy at a given strain  $\epsilon$  minus the total energy at zero strain. Then, using the following formula, one can calculate the in-plane stiffness:

$$C = \left( \frac{1}{A_0} \right) \left( \frac{d^2 E_S}{d\epsilon^2} \right), \quad (5.1)$$

where  $A_0$  is the equilibrium area of the supercell.

As explained in detail in the following sections, unitcells including one Ca, two O and two H are the primitive cells of both monolayer and bulk structures, it is doubled for bilayer. Cohesive energy per unit cell,  $E_{coh}$  is presented in table 5.2 and is calculated according to the formula:  $E_{coh} = E_{tot} - nE_{Ca} - 2nE_O - 2nE_H$ , where  $E_{tot}$  is the total energy of the unit cell of Ca(OH)<sub>2</sub>,  $E_X$  is the single atom total energy of atom X and  $n$  is the number of Ca atoms for the corresponding unit cell, i.e.  $n = 1$ ,  $n = 2$  and  $n = 1$  for monolayer, bilayer and bulk, respectively.

## Computational details

**Simulation program:** VASP and PHON[258]

**Energy cut-off:** 500 eV

**Pseudopotentials:** PBE-GGA(PAW)

**k points (Monkhorst-Pack):**  $35 \times 35 \times 1$  and  $25 \times 25 \times 11$  for few-layer and bulk Ca(OH)<sub>2</sub>, respectively

**Vacuum:** 25 Å

**Energy and force convergence criterion:**  $10^{-5}$  eV and  $10^{-2}$  eV/Å, respectively

**vdW corrections:** DFT-D2 method of Grimme [259]

**Charge analysis:** Bader's charge analysis method[216–218]

## Experimental measurements

Before our theoretical investigation of few-layer Ca(OH)<sub>2</sub>, first we present the experimental realization and detailed theoretical analysis of the characteristics of bulk Ca(OH)<sub>2</sub> crystals.

Ca(OH)<sub>2</sub> crystals were grown using the hydrolysis technique by using Ca<sub>3</sub>SiO<sub>5</sub> micro-pallets. Ca<sub>3</sub>SiO<sub>5</sub> was mixed at different water to solid ratios ranging from 0.2 to 0.9 by molar weight. The mixture was heated up to 40 °C in a controlled reaction chamber for 3 hours and controllably cooled down to 5 °C for 24 hours using a temperature controller. The growth time depends on the total water to solid ratio as well as the growth temperature. Growth time was around 8 hours for 0.6 water to solid ratio and 40 °C growth temperature. Longer growth time typically resulted in a dendritic morphology where the growth was mostly in the c-axis direction. Synthesized crystals displayed rather sharp (FWHM 7 cm<sup>-1</sup>) Raman feature at 280 cm<sup>-1</sup> and our XRD measurements displayed sharp (00l) reflections at 19.1, 39, 56.2, 77.7 degrees implying that crystals have lamellar nature.

Synthesized crystals were around 0.1-2 mm in size and they were filtered from the solution. After the filtering process, crystallites were washed off using 18.2 MΩ.cm DI wafer multiple times and dried under inert Ar gas. Crystallites were exfoliated using micro-mechanical exfoliation technique onto thermal silicon oxide / Si substrates. We find that the contrast was improved for an oxide thickness around 265-285 nm. Exfoliated flakes displayed rather sharp edges (see Fig. 5.2) with well-defined angles of 120° and 60° implying that the materials are highly crystalline. Interestingly, synthesized Ca(OH)<sub>2</sub> flakes are layered in agreement with theoretical calculations and these flakes can be easily exfoliated using the Scotch tape technique on different substrates. The exfoliated flakes do not show any signs of structural imperfection, pit formation, and overall rather flat surfaces can be obtained. In Fig. 5.2, the yellowish looking regions actually correspond to regions where the thickness is around 50-100 nm (50-100 layers) while the blue features are only 10-50 nm in thickness. Considering the ease to

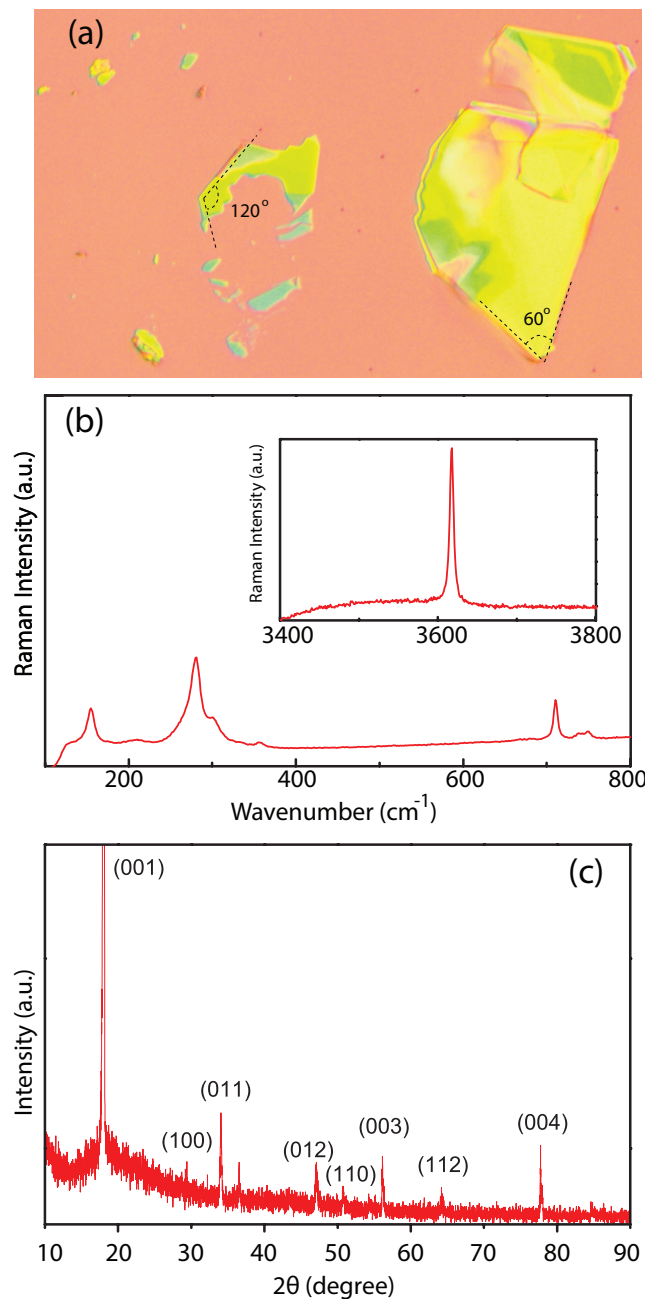


Fig. 5.2 (a) Optical image of the crystal structure and (b) Raman spectrum measured using 488 nm laser in the low and the high frequency region. The fundamental phonon branches located at the low frequency ( $100-400 \text{ cm}^{-1}$  range) and the high frequency ( $3620 \text{ cm}^{-1}$ ) are associated with the OH stretching mode. (c) XRD measurements

exfoliate this material, experimentally and theoretically we predict that they can be eventually isolated down to mono- and few-layers on various substrates.

In addition, micro-Raman measurements were performed using a 488 nm laser on a 2 micron square spot using a high intensity laser of 10 mW. We noticed that few-layers of Ca(OH)<sub>2</sub> were not subject to local over-heating / decomposition effects unlike transition metal dichalcogenides (MoS<sub>2</sub>, WS<sub>2</sub>, etc.) which typically decompose around 100 microWatt power using a similar laser excitation spot. We attribute this to the low absorption of the material associated with the rather large band gap. Raman measurements displayed various peaks in the 100-1000 cm<sup>-1</sup> range. The high frequency peak at 3620 cm<sup>-1</sup> is associated with the O-H stretching mode  $A_{1g}$ . In addition, the low frequency  $E_u(T)$  mode is found at 280 cm<sup>-1</sup>.

Here, we note that even though this material is a direct gap semiconductor, their band gap is well beyond our detectors range and since the insulators cannot be excited with such high laser wavelength, PL measurements are virtually impossible.

### Structure properties

The bulk structure of Portlandite is formed by the stacking of individual Ca(OH)<sub>2</sub> monolayers on top of each other, see Fig. 5.1. As we will exam and discuss the stacking in detail in the following paragraphs, we learned that the AA stacking is the ground state atomic configuration for bulk and multilayer structures of Ca(OH)<sub>2</sub>. In table 5.1, optimized lattice parameters of the bulk structure together with experiments and other theoretical calculation are presented. Our results consist with reference [254] and together they have good agreement with experiments. This justify the reliability of our calculations.

In the 5-atomic hexagonal primitive unit cell of bulk Ca(OH)<sub>2</sub>, the Ca atom sits at the geometrical center of the cell, i.e. {1/2a, 1/2b, 1/2c}. Two O and two H atoms form two hydroxyl groups (-OH<sup>-</sup>) located symmetrically with respect to the Ca atom. In this arrangement, coordinates of H and O only differ by their positions along the **c** lattice axis and their fractional coordinates can be given as {1/6a, 1/6b, (1/2c - c<sub>O</sub>)} and {1/6a, 1/6b, (1/2c - c<sub>H</sub>)} for one hydroxyl, {5/6a, 5/6b, (1/2c + c<sub>O</sub>)} and {5/6a, 5/6b, (1/2c + c<sub>H</sub>)} for the other

Table 5.1 Comparison of calculated results for structures parameter of bulk  $\text{Ca}(\text{OH})_2$  with experimental results and with theoretical results from other reference: lattice constants  $a$  and  $c$ , volume  $V$  and  $c/a$  ratio.

Structure parameters	Exp. <sup>a</sup>	Exp. <sup>b</sup>	PBE-PAW (this work)	PBE-PAW <sup>c</sup>
$a$ ( $\text{\AA}$ )	3.589	3.592	3.614	3.612
$c$ ( $\text{\AA}$ )	4.911	4.906	4.982	4.942
$V$ ( $\text{\AA}^3$ )	54.78	54.82	56.35	55.85
$c/a$	1.368	1.366	1.379	1.368

<sup>a</sup> Ref. [260]

<sup>b</sup> Ref. [261]

<sup>c</sup> Ref. [254]

one, where  $c_O$  and  $c_H$  are the vertical shifts of the positions of O and H atoms from the Ca plane in the unit of  $\text{\AA}$ , respectively.

In the optimized structure, the lattice constants  $a$  and  $c$  are 3.61  $\text{\AA}$  and 4.98  $\text{\AA}$  in the bulk structure, parameters  $c_O$  and  $c_H$  are calculated to be 1.15  $\text{\AA}$  and 2.12  $\text{\AA}$ . Bond length of Ca-O and O-H are 2.36  $\text{\AA}$  and 0.97  $\text{\AA}$ . Interlayer distance which is defined as the distance between the uppermost H-layer of the underlying layer and the lowermost H-layer of the top-lying layer is found to be 0.49  $\text{\AA}$ . Differing from other lamellar bulk crystal structures such as graphite (3.58  $\text{\AA}$ ) and  $\text{MoS}_2$  (3.42  $\text{\AA}$ )[262],  $\text{Ca}(\text{OH})_2$  layers are more closely stacked on top of each other.

Our calculations revealed that going from bulk to monolayer the in-plane lattice parameter  $a$  change to 3.62  $\text{\AA}$ . In our calculations, the  $c$  lattice parameter in the hexagonal unit cell of the monolayer is set to 25  $\text{\AA}$  in order to avoid interlayer interaction between the adjacent layers. In the monolayer  $\text{Ca}(\text{OH})_2$ , parameters  $c_O$  and  $c_H$  are calculated to be  $c_O=1.14 \text{\AA}$  and  $c_H=2.10 \text{\AA}$ , respectively. Ca-O and O-H bond distances are 2.38  $\text{\AA}$  and 0.97  $\text{\AA}$  in the monolayer, respectively. We observed only quite small change as the system going from bulk to monolayer, some of the structure parameters even left unchanged, from this we can conclude quite weak interlayer interaction in  $\text{Ca}(\text{OH})_2$ . In order to study the interlayer interaction we further investigate their effect on stacking, and by including the vdW correction in the functional we are able to identify the nature of this interaction.

Table 5.2 Calculated results for different structures of  $\text{Ca(OH)}_2$ : lattice constants  $a$ , vertical shift of O and H atom  $c_O$   $c_H$ , Ca-O and O-H bond length, energy band gap  $E_{gap}$ , cohesive energy per atom  $E_{coh}$ , charge transfer from Ca atom to O atom  $\Delta Q$ , in-plane Young's modulus  $E_{xx}$ ,  $E_{yy}$ , in-plane Poisson's ratio  $\nu_{xy}$ , in-plane shear modulus  $G_{xy}$  and in-plane stiffness  $C$ . For comparison, theoretical calculation on same quantities of BN are shown in the last row.

	$a$ (Å)	$c_O/c_H$ (Å/Å)	Ca-O/O-H (Å/Å)	$E_{gap}$ (eV)	$E_{coh}$ (eV)	$\Delta Q$ (e)	$E_{xx}, E_{yy}$ (N/m)	$\nu_{xy}$	$G_{xy}$ (N/m)	$C$ (J/m <sup>2</sup> )
Bulk $\text{Ca(OH)}_2$	3.61	1.15/2.12	2.36/0.97	4.08	4.52	1.6	55.0	0.30	21.23	60.1
2L $\text{Ca(OH)}_2$	3.62	1.15/2.12	2.38/0.97	3.70	4.48	1.6	50.7	0.32	19.16	55.6
1L $\text{Ca(OH)}_2$	3.62	1.14/2.11	2.38/0.97	3.67	4.39	1.6	50.7	0.33	19.08	53.2
1L BN	2.51 <sup>a</sup>	-	1.45 <sup>a,b</sup>	4.64 <sup>a</sup>	8.82 <sup>a</sup>	0.43 <sup>a,c</sup>	278.2 <sup>d</sup>	0.22 <sup>d</sup>	113.5 <sup>d</sup>	267 <sup>e</sup>

<sup>a</sup> Ref. [263]

<sup>b</sup> B-N bond length

<sup>c</sup> charge transfer from B to N

<sup>d</sup> Ref. [264]

<sup>e</sup> Ref. [265]

Individual layers of lamellar structures such as graphite, hex-BN and TMDs are held together mainly by the van der Waals force in order to form a bulk layered structure. Such a weak interaction stems from dynamical correlations between fluctuating charge distributions in neighboring layers. Here we investigated the energies of various bilayer configurations. As presented in Fig. 5.3 there are six possible types of stacking between two  $\text{Ca(OH)}_2$  monolayers. Similar to the stacking nomenclature of bilayer graphene, we classify the stacking types to be either AA or AB $n$  ( $n=1,2,\dots,5$ ). The same type of atoms from different monolayers are on top of each other in AA stacking whereas AB stackings can be reached by shifting one of the layers along certain lattice vectors. One set of AB stackings could be realized by shifting the second layer in the AA stacking towards  $[1\bar{1}0]$ , which gives stacking AB1, and by shifting towards the  $[110]$  direction, which gives stacking AB2, see first row in Fig. 5.3. Another set of bilayers are achieved by first flipping the second layer upside down in AA stacking, which would give stacking AB3, then AB4 and AB5 can be constructed by doing the same shifting on the second layer of AB3 towards  $[1\bar{1}0]$  and  $[110]$  directions of the 1st layer, respectively. After relaxation of all stackings, the variation of the  $a$  lattice constant among the different stacking types is less than 0.01 Å. The smallest interlayer distance, as defined previously for bulk, is for AA stacking which equals 0.49 Å, the same as that in bulk. For AB stacking the interlayer distance

is 1~2 Å larger than that for AA stacking. As depicted in Fig. 5.3, AA stacking is 96~137 meV per formula more favorable than all other possible stacking types and hence it corresponds to the lowest energy configuration.

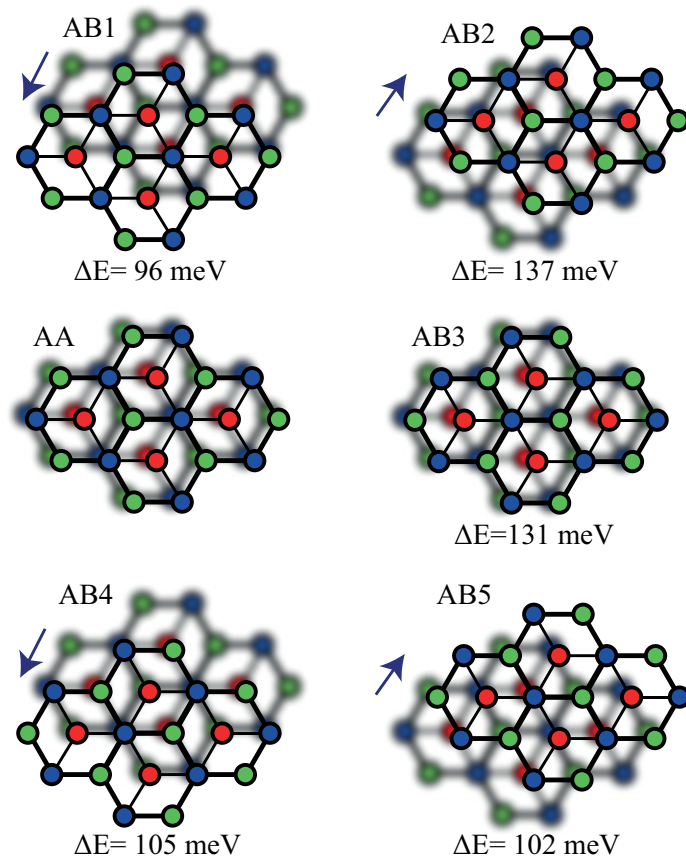


Fig. 5.3 Different stacked bilayers (bottom layer is blurred) and their energy difference with respect to the AA stacking of  $\text{Ca}(\text{OH})_2$ , i.e.  $\Delta E = E_{\text{ABX}} - E_{\text{AA}}$ , ( $X=1,2,\dots,5$ ). Energies are given per formula of  $\text{Ca}(\text{OH})_2$ . Blue, green and red circles are for Ca atom, upper hydroxyl group and lower hydroxyl group, respectively. For clarity, the bottom layer is shifted slightly.

To investigate the nature of the interlayer interaction, we have calculated the interlayer interaction energy (IE) for the AA stacked bilayer structure of  $\text{Ca}(\text{OH})_2$ . The IE is the energy difference between the total energy at a specific interlayer distance and that of a well separated bilayer. The plot of IE versus interlayer distance is shown in Fig. 5.4, where the energy of the well separated bilayer is defined as 0 eV. Two sets of calculations were performed, one set only considers

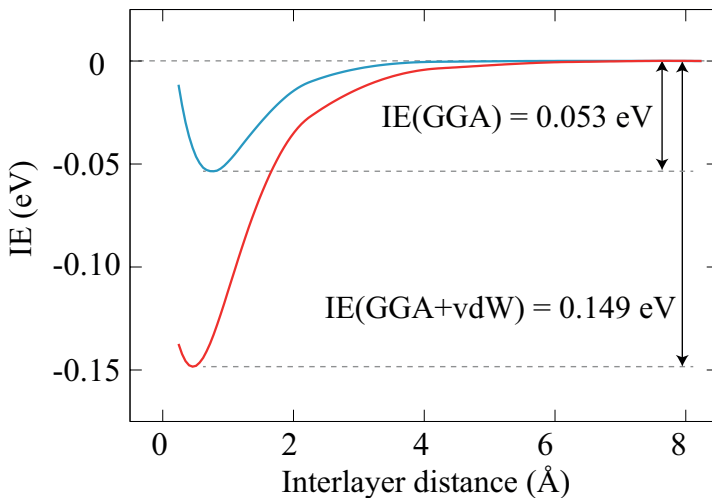


Fig. 5.4 Interlayer interaction energy per formula of AA-stacked bilayer  $\text{Ca}(\text{OH})_2$ . Blue and red curves are for GGA calculations without and with vdW correction, respectively.

GGA exchange correlation; while another set considers both the GGA and vdW interaction. At the optimized interlayer distance for the bilayer structure, almost 2/3 of the attractive interaction comes from the van der Waals interaction, and this is consist with D'Arco *et al.* [253] . They stated that interlayer interaction of Brucite, one of the isomorphous of Portlandite, is mainly a dispersion-type interaction. The nature of interlayer interaction in  $\text{Ca}(\text{OH})_2$  is mainly vdW type weak interaction. Our GGA+vdW calculations revealed that the interlayer interaction between two layers of  $\text{Ca}(\text{OH})_2$  (149 meV per formula) is much stronger than that of bilayers of  $\text{MoS}_2$  (76 meV per formula).

### Electronic properties

Our Bader charge transfer analysis showed that the final (initial) electron charge on Ca, O and H atoms after (before) the formation of the crystal are 6.4e (8.0e), 7.4e (6.0e) and 0.4e (1.0e), respectively. Therefore, in the bulk structure of  $\text{Ca}(\text{OH})_2$ , Ca-O bonds, which are mostly in ionic character, are formed through 0.8e charge transfer from each Ca to O atom. Charge transfer is kept unchanged when it comes to the monolayer structure, except for the rest charge on H atom is 0.6e in monolayer.

Our calculations on the electronic structure reveal that bulk  $\text{Ca(OH)}_2$  is an insulator with a 4.37 eV direct band gap. As shown in Fig. 5.5 (a), the valence band maximum (VBM) and the conduction band minimum (CBM) are located at the  $\Gamma$  point. The partial density of states (DOS) shown in Fig. 5.1 (b) indicates that the major contribution to the states at the valence and conduction band edge originates from the O atoms, while deeper in the conduction band, states are mainly composed of the orbitals of Ca. The orbital character of a state at a particular band can also be deduced from a band and  $k$ -point decomposed charge density. As seen from Fig. 5.5 (c), edges in the top of VBM have  $\text{O-}p_x$  and  $\text{O-}p_y$  orbital character, and the hybridization of these states are also shown in the same figure. While the CBM has some  $p_z$  orbital character from the O atoms, but as the energy of the state increases, the  $d$  orbitals from Ca atom start to contribute, see ⑧ in the same figure.

Electronic properties of  $\text{Ca(OH)}_2$  are quite different from similar two-dimensional graphene-like structures. Unlike TMDs (such as  $\text{MoS}_2$  and  $\text{WSe}_2$ ) that exhibit indirect-to-direct band gap crossover when going from bulk to a single layer structure,  $\text{Ca(OH)}_2$  is a direct band gap semiconductor which is independent of the number of layers. Although the energy band gap at the  $\Gamma$  point decreases from 4.03 to 3.67 eV for a monolayer structure, electronic dispersion of the valence band edge remains almost unchanged, see Fig. 5.5 (d). As shown in Fig. 5.5 (e) the conduction states mainly originate from Ca atoms, while the valence states are mainly composed of the orbitals of O atoms.

Our magnetic state analysis shows that unless a defect is formed in/on the structure, there is no spin polarization in the ground state of both bulk and monolayer  $\text{Ca(OH)}_2$ . Therefore,  $\text{Ca(OH)}_2$  is a non-magnetic insulator regardless of its dimension for the structure.

Moreover, it was seen that the spin-orbit interaction has no considerable effect on the bond lengths and the overall electronic dispersion (except for a 26 meV splitting in the VBM at the  $\Gamma$  point, see Fig. 5.5 (f)). Due to the presence of inversion symmetry of  $\text{Ca(OH)}_2$ , the degeneracy of spin-up and spin-down states still remains, this is also confirmed by the results of our calculation.

Band and  $k$ -point decomposed charge density in Fig. 5.5 are kept with the same isosurface level for comparison. However, as we further reduced the iso-surface level at ④ in (d) and (g) of Fig. 5.5, which is the lowest conduction band

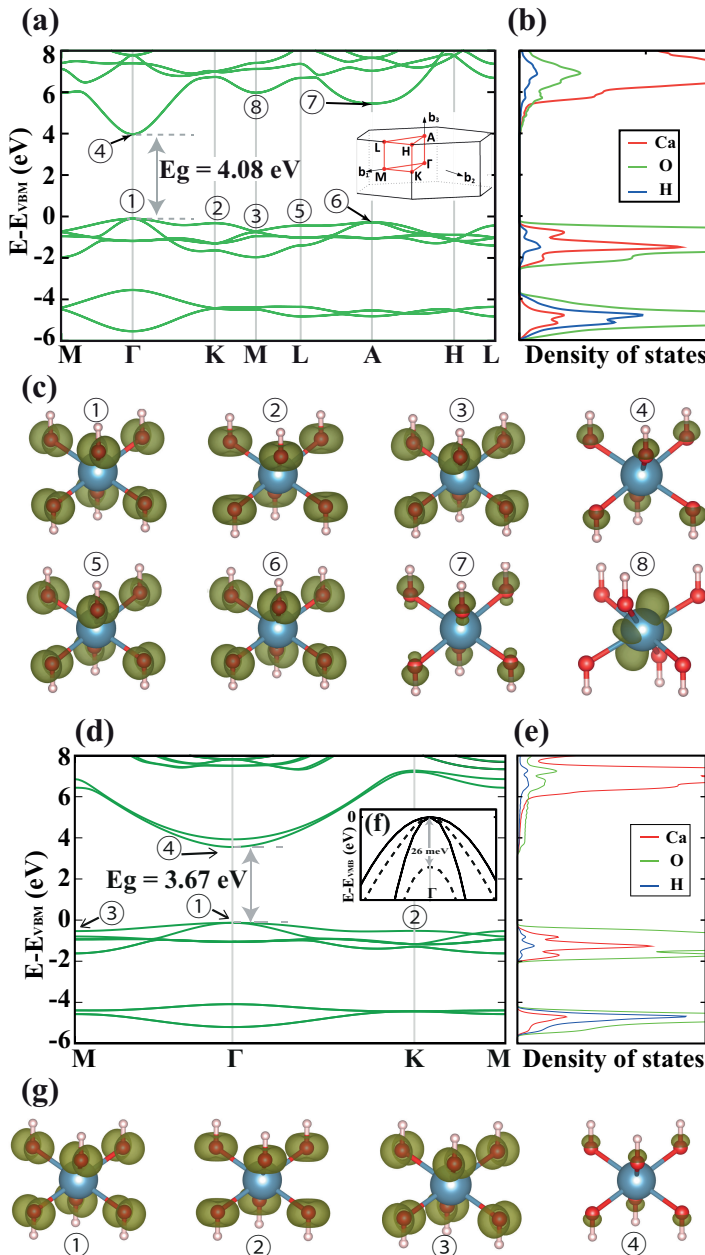


Fig. 5.5 (a) and (d) are the Band structures, (b) and (e) are the partial DOS and (c) and (g) are the band and  $k$ -point decomposed charge densities of the bulk (c) and monolayer (g)  $\text{Ca}(\text{OH})_2$ , respectively. The charge density are the band edges indicated in (a) and (d), isovalue are kept constant. (f) Band structure around  $\Gamma$  point is shown with (dashed line) and without (solid line) spin orbit coupling.

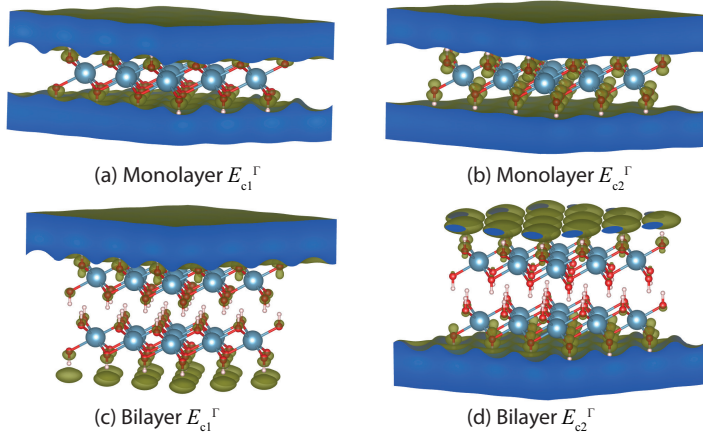


Fig. 5.6 Two lowest conduction band charge density of monolayer and bilayer  $\text{Ca}(\text{OH})_2$  at the  $\Gamma$  point.

of the monolayer at the  $\Gamma$  point:  $E_{c1}^{\Gamma}$ , charge density forms a planar state parallel to the layer on both sides, see Fig. 5.6 (a), this is also the case for the second lowest non-spin-resolved conduction band at the same  $k$ -point:  $E_{c2}^{\Gamma}$ , see Fig. 5.6 (b). These two states are important due to their unique character and having energy right below ionization energy. Such exceptional states having free-electron-like dispersion were reported before[266, 267] for doped graphite. To study the trend in these states, the same states were plotted for bilayer  $\text{Ca}(\text{OH})_2$ , see (c) and (d) in Fig. 5.6.  $E_{c1}^{\Gamma}$  and  $E_{c2}^{\Gamma}$  have lower energies than ionization energy. Therefore, electrons are still close and bond to both sides of monolayers as seen from charge density. In the case of bilayer, interestingly, these states appear only on one side of bilayer.

### Mechanical properties

We present the quantities that describe the mechanical properties of  $\text{Ca}(\text{OH})_2$  in table 5.2. At first, the in-plane Young's modulus of the bulk structure is calculated. Bulk  $\text{Ca}(\text{OH})_2$  has an in-plane Young's modulus (55.0 N/m) and in-plane shear modulus (21.23 N/m). Both these quantities indicating flexible nature to in-plane tensile and shear deformation of bulk  $\text{Ca}(\text{OH})_2$ . In addition, bulk  $\text{Ca}(\text{OH})_2$  has an in-plane Poisson's ratio of 0.30. Additionally, the value of the in-plane stiffness for bulk  $\text{Ca}(\text{OH})_2$  is calculated to be 60.1 J/m<sup>2</sup>.

If we go from bulk to bilayer  $\text{Ca(OH)}_2$ , we see a reduction in either the in-plane Young's modulus or the in-plane shear modulus, which are 50.7 N/m and 19.16 N/m, respectively. The in-plane Poisson's ratio on the other hand is slightly increased to 0.32 and become more spongy-like as opposite to more cork-like character[268]. In addition, the in-plane stiffness value of bilayer  $\text{Ca(OH)}_2$  is calculated to be 55.6 J/m<sup>2</sup>.

We found that monolayer  $\text{Ca(OH)}_2$  has a quite low in-plane Young's modulus (50.7 N/m) when compared to BN (278.2 N/m). The in-plane Poisson ratio (0.33) and the in-plane shear modulus (19.08 N/m) of the monolayer are similar with those for bilayer, and for BN, they are 0.22 and 113.5 N/m respectively. The calculated values of the in-plane stiffness of monolayer  $\text{Ca(OH)}_2$  is 53.2 J/m<sup>2</sup>.

### Vibrational properties

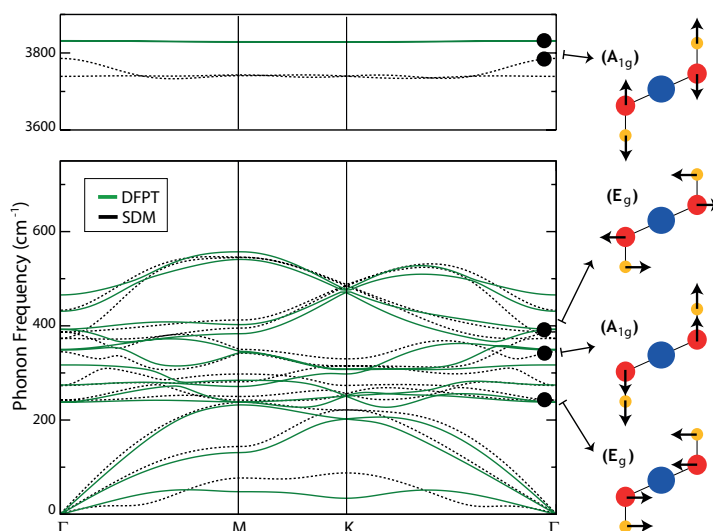


Fig. 5.7 Phonon dispersion of monolayer  $\text{Ca(OH)}_2$ .

Lastly, for the analysis of the vibrational spectrum and further examination of the dynamical stability of monolayer  $\text{Ca(OH)}_2$ , we performed a calculation of the phonon spectrum using both the first-principles small displacement methodology (SDM)[258] and density functional perturbation methodology (DFPT)[173]. Here the non-quadratic dispersion of the flexural mode around the zone center is directly related to the insufficient FFT grid along the vacuum direction. It is seen from Fig. 5.7 that similar to the Raman shift measurements observed from the

bulk crystal structure, monolayer material has also high-frequency OH stretching modes at 3700-3800 cm<sup>-1</sup>.

Further analysis of the analysis of phonon branches shows that the decomposition of the vibration representation of optical modes at the zone center is  $\Gamma = 4E_u + 2A_{2u} + 4E_g + 2A_{1g}$ . As shown in right panel of Fig. 5.7 there are four Raman-active phonon branches around 240, 350, 390 and 3700-3800 cm<sup>-1</sup>. It is also worth to note that differing from other TMD structures having 1T phase, presence of H atoms results in existence of two different  $E_g$  and  $A_{1g}$  modes. Here the phonon dispersion having real eigenfrequencies in the whole Brillouin Zone, which is another indication of the stability of monolayer Ca(OH)<sub>2</sub>.

### summary

By performing first principle calculations on bulk, bilayer and monolayer Ca(OH)<sub>2</sub> and experimental confirmation of the bulk crystal layered structure, we have predicted several important properties of this material and their stability. We found that: (i) Ca(OH)<sub>2</sub> crystals are environmentally stable and their stable structures can be synthesized by experimental methods; (ii) Experimentally, we also demonstrated that Ca(OH)<sub>2</sub> crystals can be grown in layered form and also be exfoliated on arbitrary substrates; (iii) The dimensionality of Ca(OH)<sub>2</sub> will not change the electronic, structural and magnetic properties qualitatively, nevertheless intrinsic mechanical stiffness of each layer will become slightly stiffer as the system go from monolayer to bilayer. (iv) Interlayer interaction is mainly van der Waals dispersion-type force, and the strength of the interaction is stronger than that of similar layered materials (e.g MoS<sub>2</sub> and graphite). (v) The conduction states which have a free-electron-like character may be utilized for high-mobility electron transfer.

We believe that the stable structure and the unique electronic properties of ultra-thin Ca(OH)<sub>2</sub>, predicted for the first time here, will trigger interest in this new class of materials.

### 5.1.2 Few-layer of pentasilicene<sup>2</sup>

#### Introduction

Recently, a new 2D structure for carbon was proposed, called penta-graphene[200]. This crystal is composed entirely of pentagonal rings of C atoms with mixed  $sp^2/sp^3$  orbital hybridization. However, the silicon counterpart of this structure, penta-silicene, contains a dynamical instability in its monolayer form. A few attempts have been made to stabilize this new Si structure by hydrogenation[269] and chemical doping[270].

In the present work, we construct multilayer structures of penta-silicene. We use density functional theory to explore their stability and physical properties. Two types of stacking for the penta-silicene layers are found to give stable few-layer structures. These different stacking types lead to completely different electronic properties since one leads to metallic and the other to semiconducting behavior. Somewhat surprisingly, we found that bilayer penta-silicene has lower formation energy than the most stable hexagonal silicene bilayers. Furthermore, we found that the band gaps of these semiconducting penta-silicene bilayers can be tuned by mechanical strain. We first explore the stability of monolayer penta-silicene and demonstrate its dynamical instability. This forms the motivation to study few-layer systems. Then we investigate different stacking possibilities and the resulting stability. Further, we study their mechanical properties by calculating their elastic constants. We also compare bilayer penta-silicene to the most stable bilayer hexagonal silicene structures. Lastly, The electronic properties of multilayered penta-silicene are discussed.

#### Computational details

**Simulation program:** VASP and Phonopy

**Energy cut-off:** 500 eV

**Pseudopotentials:** PBE-GGA(PAW)

**k points (Monkhorst-Pack):**  $17 \times 17 \times 1$  and  $23 \times 23 \times 1$  for insulating and metallic systems, respectively

**Vacuum:** 20 Å

**Energy and force convergence criterion:**  $10^{-8}$  eV and  $10^{-7}$  eV/Å, respectively

**phonon calculation:** finite displacement method

---

<sup>2</sup>This work is published in: P6.

**Supercell for phonon calculation:**  $4 \times 4 \times 1$  and  $3 \times 3 \times 2$  for few-layer and bulk systems, respectively

**Ab initio molecular dynamics:** Parrinello-Rahman (NpT) dynamics [271, 272] and a Langevin thermostat [273]

**Ab initio molecular dynamics (Energy cut-off):** 300 eV

**Ab initio molecular dynamics (time step):** 2 fs

**Ab initio molecular dynamics (temperature):** 100 K

**Ab initio molecular dynamics (simulation time):** 6 ps

### Monolayer pentasilicene

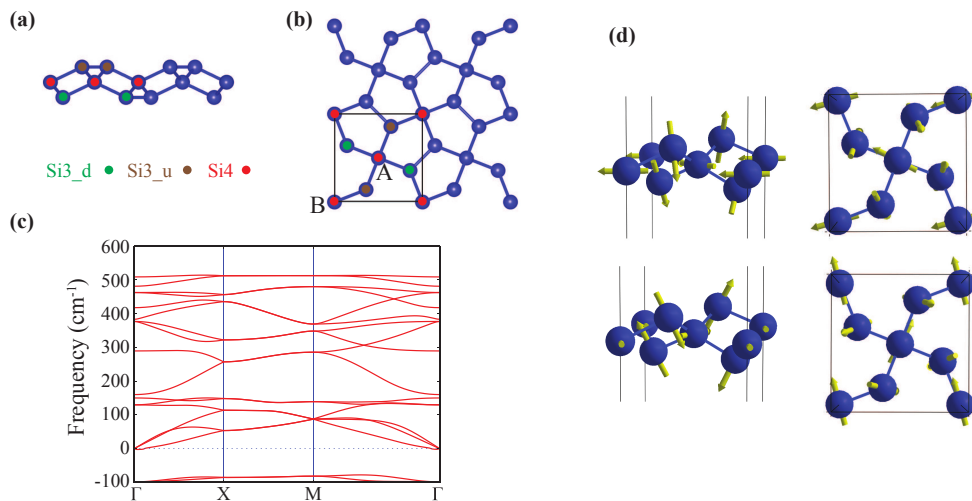


Fig. 5.8 (a) Side view and (b) top view of the atomic structure, (c) phonon spectrum and (d) two vibration modes with imaginary frequency of monolayer penta-silicene. Visualization of vibration modes is done with the V\_Sim package [274].

The layer group symmetry of monolayer penta-silicene (p-Si) is  $p\bar{4}2_1m$  (58). As shown in Fig. 5.8(a) and Fig. 5.8(b), the primitive cell contains six silicon atoms, of which two have fourfold coordination (Si4) and four have threefold coordination (Si3). Two of the Si3 atoms reside above the Si4 atoms, denoted as Si3\_u, while the other two are below the Si4 atoms, denoted as Si3\_d. The Si4 atoms are bonded to four Si3 atoms while the Si3 atoms are connected to two Si4 atoms and one neighboring Si3 atom. Note that the two Si4 atoms have equivalent environments which are rotated by approximately  $41^\circ$  with respect to each other.

Therefore, in analogy to graphene, we can relate these two equivalent Si4 atoms to sublattices which in the following will be referred to as the A and B sublattice.

The dynamical stability of this structure can be studied through its phonon spectrum. As noted before[269, 270] the phonon spectrum of monolayer p-Si contains imaginary frequencies as shown in Fig. 5.8(c), which is a clear signature of its instability. The corresponding atomic vibrations of the two imaginary frequencies at the  $\Gamma$  point are shown in Fig. 5.8(d). These modes correspond mainly to out-of-plane vibrations of the Si3 atoms with respect to the Si4 atoms. As a consequence, the structure is found to fall apart, indicating that there is no stable form of monolayer p-Si. However, the addition of extra layers could reduce these out of plane vibrations and stabilize the structure. This is the motivation to study few-layer p-Si.

### Multilayers of pentasilicene structures

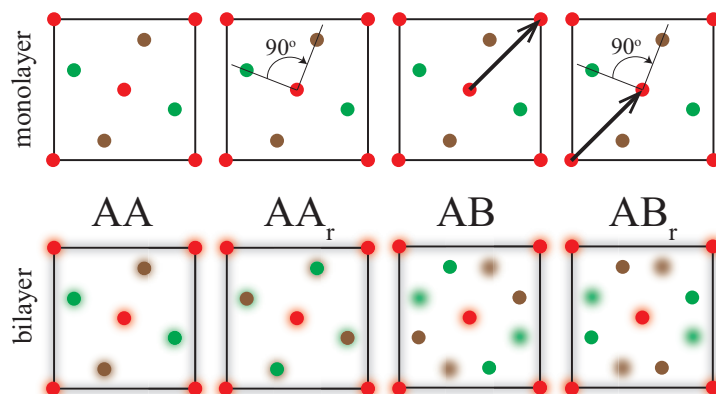


Fig. 5.9 Schematic illustration of the four stacking types for bilayer p-Si. The colors of the symbols correspond to those of the monolayer in Fig. 5.8(a) and Fig. 5.8(b). The bottom layer in the bilayer is blurred for clarity. The arrow represents translation and the angle represents the rotation of the top layer with respect to the bottom layer.

When considering two layers, different stacking configurations are possible. Here we focus on the so-called AA and AB stacking modes of the aforementioned sublattices (see Fig. 5.9). The stacking in which both layers have the same in-plane orientation and the Si atoms are put right on top of each other is called

Table 5.3 The cohesive energy ( $E_{coh}$ ), the interlayer binding distance ( $d_{inter}$ ), the interlayer binding energy ( $E_{inter}$ ), number of interlayer bonds ( $N_b$ ) and energy per bond ( $E_{bond}$ ) of the four possible stacking types of bilayer p-Si. The interlayer binding energy per unit cell is defined as  $E_{inter} = E_{bi} - 2E_{mono}$ .

structure	$E_{coh}$ (eV/atom)	$d_{inter}$ (Å)	$E_{inter}$ (eV)	$N_b$	$E_{bond}$ (eV)
AA	-4.129	0.795	-3.502	4	-0.875
AA <sub>r</sub>	-4.113	2.379	-3.318	2	-1.659
AB	-3.968	2.174	-1.574	2	-0.787
AB <sub>r</sub>	-4.147	1.893	-3.725	2	-1.862
AB <sub>r</sub> <sup>d</sup>	-4.185	1.896	-4.174	2	-2.087

AA stacking. AB stacking arises by shifting the A sublattice of one layer to the B sublattice of the other. This nomenclature was also used by Wang *et al.* [275] for bilayer penta-graphene. Although penta-silicene has a tetragonal lattice symmetry, the highest proper rotational symmetry order is two. Therefore, there are also two different possible orientations of the upper layer with respect to the lower one: One in which the two layers have the same orientation and another in which one layer is rotated over 90° with respect to the other one. We denote this last orientation with a subscript *r* to show that it results from a 90° rotation, e.g. AA<sub>r</sub>. Therefore, there are four possible stacking types for bilayer p-Si. Note that AB<sub>r</sub> stacking corresponds to the recently proposed bulk T12 phase for group IVA elements[276]. However, as discussed in more detail below, perfect AB<sub>r</sub> stacking is not stable in the case of multilayer penta-silicene. A considerable distortion of the outer layers is required to stabilize AB<sub>r</sub> stacking. The distorted structure, which will be referred to as AB<sub>r</sub><sup>d</sup> in the following, is obtained by breaking the symmetry between the two Si<sub>3</sub> atoms at each surface side in AB<sub>r</sub> multilayers. In this way, one of the two Si<sub>3</sub> atoms acquires sp<sup>2</sup> hybridization and loses an electron to the other Si<sub>3</sub> atom that has sp<sup>3</sup> hybridization.

In table 5.3, we compare the energies of the different stacking modes. In all cases the Si<sub>4</sub> atoms are not involved in interlayer bonding since their possible number of bonds is already saturated. Except for the AA stacking where all Si<sub>3</sub> atoms are bound to Si<sub>3</sub> atoms from the other layer, only half of the Si<sub>3</sub> atoms are bonded to the other layer in the other cases. In table 5.3, the size of the interlayer binding energy and the strength per bond are given. The size of the

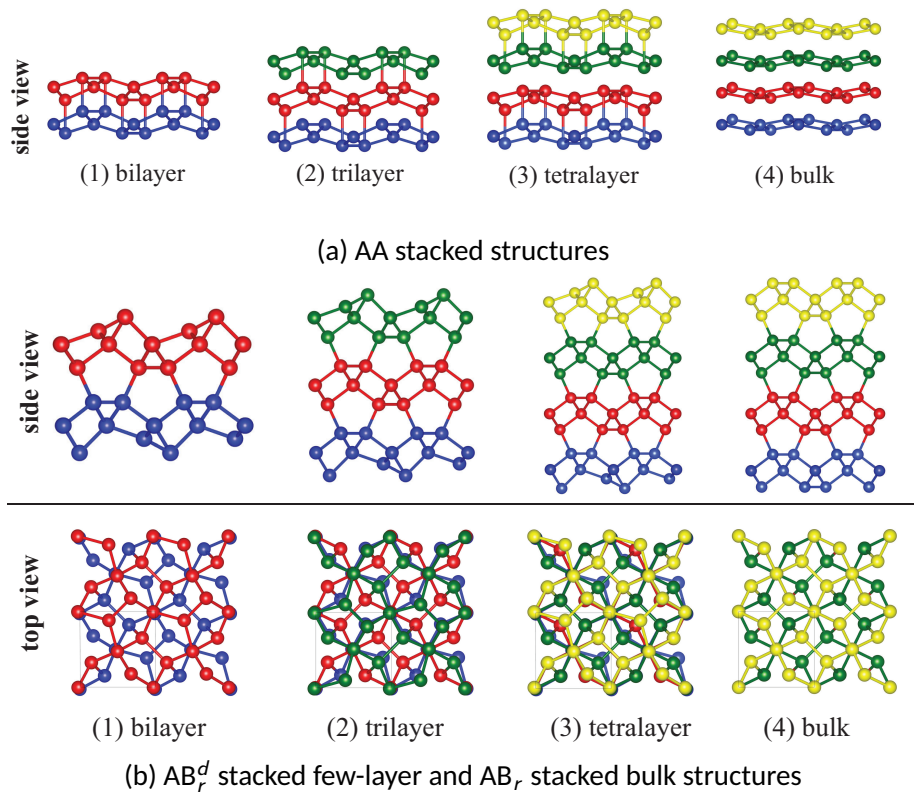


Fig. 5.10 Atomic structure of the  $2 \times 2$  supercell of few-layer p-Si. The number of atomic layers in the bulk structure is fixed to four for comparison (i.e.  $2 \times 2 \times 4$  and  $2 \times 2 \times 2$  supercells for AA and  $\text{AB}_r$  stacked bulk p-Si). (Visualisation using VESTA [204]).

bond energies indicate strong chemical bonding. The  $\text{AB}_r^d$  stacking mode clearly forms the most stable structure. For the rest of the paper, we will only focus on the most stable AA and AB-type stacking, i.e. AA and  $\text{AB}_r^d$ .

Table 5.4 The layer (space) group for few-layer (bulk) systems. The lattice constant ( $a$ ), the interlayer distance ( $d_{\text{inter}}$ ), the nearest-neighbor bond length range ( $d_{\text{min/max}}$ ), the cohesive energy ( $E_{\text{coh}}$ ), and the band gap (PBE) of few-layer and bulk p-Si.

stacking	structure	layer/space group	$a$ (Å)	$d_{\text{inter}}$ (Å)	$d_{\text{min}}$ (Å)	$d_{\text{max}}$ (Å)	$E_{\text{coh}}$ (eV/atom)	band gap (eV)
-	monolayer	$p\bar{4}2_1m$ (58)	5.587	-	2.233	2.363	-3.837	0.046 ( $M \rightarrow \Sigma$ )
AA	bilayer		5.907	0.795	2.363	2.468	-4.129	metal
	trilayer	$p\bar{4}2_1m$ (58)	5.887	1.085	2.330	2.606	-4.108	metal
	tetralayer		5.980	0.996/1.794 <sup>a</sup>	2.368	2.478	-4.150	metal
	bulk	$P\bar{4}2_1m$ (113)	6.234	1.769	2.398	2.463	-4.204	metal
AB <sub>r</sub> <sup>d</sup>	bilayer	$pb2b$ (30) $pm2a$ (31)	5.222	1.896	2.303	2.403	-4.185	0.119 ( $M \rightarrow \Sigma$ )
	trilayer	$p1$ (1)	5.222	1.989	2.298	2.413	-4.291	0.247 ( $M \rightarrow \Sigma$ )
	tetralayer	$pb2b$ (30) $pm2a$ (31)	5.221	1.997	2.298	2.413	-4.345	0.232 ( $M \rightarrow \Sigma$ )
AB <sub>r</sub>	bulk	$P4_2/nmc$ (138)	5.220	1.999	2.358	2.413	-4.508	1.329 ( $M \rightarrow \Delta$ )

<sup>a</sup> The first and the second number indicate the interlayer distance between two monolayers and two bilayers, respectively.

We also investigated the stability of trilayer, tetralayer and bulk p-Si structures by adding extra layers to the stable bilayers mentioned above, their structures are shown in Fig. 5.10a and Fig. 5.10b. We list their structural and energetic properties in table 5.4. Extra layers increase the cohesive energy per atom due to a smaller ratio of surface atoms. For AA stacking, adding a 4th layer to a trilayer system results in a double bilayer system with lesser bonding between them. Going to AA bulk, the interlayer interaction appears to be further reduced and the buckled layers become more flat. Adding extra layers to an  $\text{AB}_r^d$  bilayer results in similar structures in which the Si<sub>3</sub> atoms of the surface layers become distorted. For bulk, the undistorted  $\text{AB}_r$  structure is found in which  $\bar{4}$ -fold symmetry is restored.

## Stabilities

In this section we investigate the stability of the different multilayer structures discussed above. Phonon calculations for the AA and  $\text{AB}_r$  stacking modes reveal that only the AA bilayer is dynamically stable at low temperature. The extra bonds of the Si<sub>3</sub> atoms in AA-stacked structures effectively reduce out-of-plane vibrations and stabilize the structure. Although the AA-stacked bulk structure has weaker interlayer bonding, its phonon spectrum contains no imaginary frequencies, indicating its dynamical stability. The  $\text{AB}_r$ -stacked layers, on the other hand, exhibit similar out-of-plane vibrations of the outermost Si atoms as a monolayer. For  $\text{AB}_r^d$ -stacking the distortion of the outermost layer removes the instabilities from the phonon spectrum, so that these structures are also dynamically stable.

It is also interesting to see whether these structures remain stable at finite temperature. To this end, we performed *ab initio* molecular dynamics calculations at a temperature of 100 K. The evolution of the cohesive energy as a function of simulation time is shown in Fig. 5.12. For comparison, the results for the dynamically unstable monolayer are also shown. The monolayer laterally shrinks and becomes a disordered multilayered system. The AA and  $\text{AB}_r^d$  bilayer systems, on the other hand, remain stable and retain their crystalline structure.

As a final stability check, we investigate the mechanical stability of bilayer p-Si which is determined by the elastic constants of the structures. If the elastic constants satisfy the necessary and sufficient Born criteria generalized by

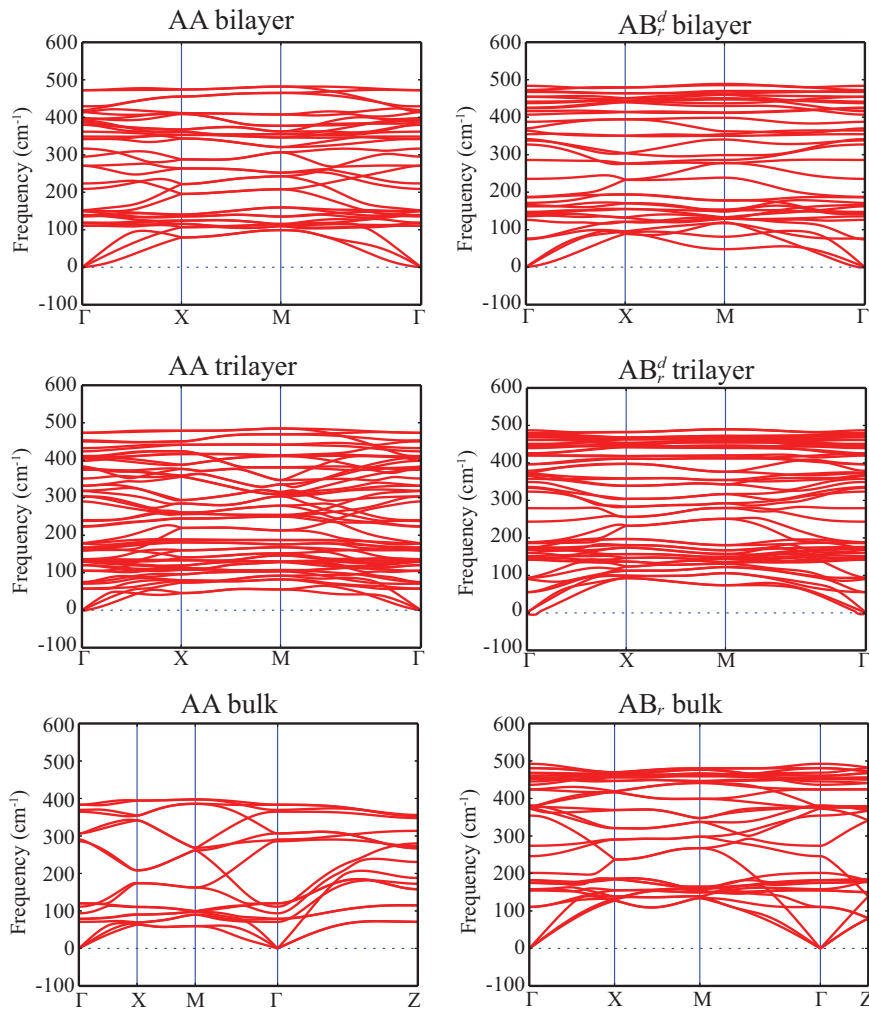


Fig. 5.11 Phonon spectra of different-stacked few-layer p-Si.

Mouhat & Coudert [138], the structures are mechanically stable. AA bilayer p-Si belong to the layer group symmetry of  $p\bar{4}2_1m$ , which belongs to the tetragonal symmetry groups, and the independent elastic constants in 2D are:  $C_{11}=101.43$  N/m,  $C_{12}=36.36$  N/m and  $C_{66}=39.53$  N/m. In the case of  $AB_r^d$  bilayer p-Si, the crystal possesses pb2b or pm2a layer group symmetry which belongs to the orthorhombic crystal systems, and the independent elastic constants are:  $C_{11}=C_{22}=63.83$  N/m,  $C_{12}=26.92$  N/m and  $C_{66}=50.43$  N/m. For mechanical stability, the following criteria must be fulfilled for 2D tetragonal systems:

$$C_{11} > |C_{12}|, C_{66} > 0, \quad (5.2)$$

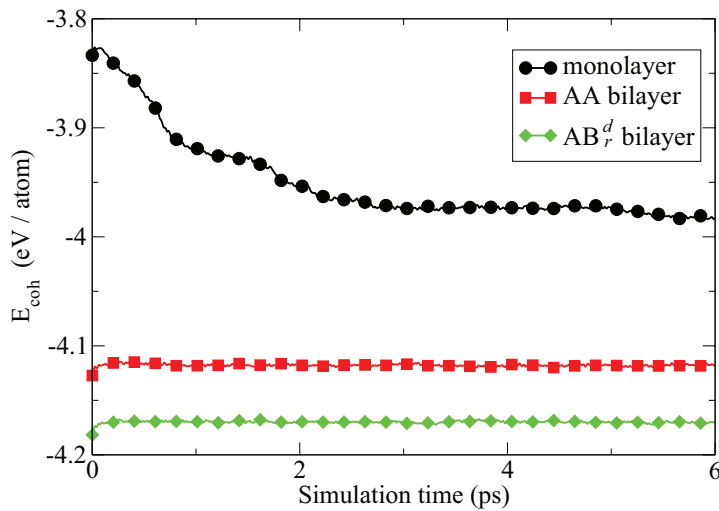


Fig. 5.12 The cohesive energy of monolayer and AA and  $\text{AB}_r^d$  stacked bilayer p-Si as a function of time at a temperature of 100 K under NpT-ensemble.

while 2D orthorhombic systems should satisfy:

$$C_{11} > 0, C_{11}C_{22} > C_{12}^2, C_{66} > 0. \quad (5.3)$$

As one can see, these criteria are satisfied by AA and  $\text{AB}_r^d$  bilayer p-Si which ensures their mechanical stability. Additionally, in table 5.5, we list the (2D) Young's modulus, shear modulus and Poisson's ratio of bilayer p-Si systems. An interesting aspect of the possion's ratio of  $\text{AB}_r^d$  is that it is quite high and close to the theoretical limit of 0.5. This means that this 2D material, prefers to change its shape rather than its surface area under strain, similar to the (3D) cases of rubber and water.

Table 5.5 Mechanical properties of  $\text{AB}_r^d$  bilayer p-Si

Stacking	$E[\text{N/m}]$	$G[\text{N/m}]$	$\nu$
AA	88.40	39.53	0.36
$\text{AB}_r^d$	52.47	50.41	0.42

### Relative phase stability

In this section we compare the cohesive energy of bilayer p-Si to the more familiar bilayer hexagonal silicene structures (h-Si). We examined 3 different stacking

types for h-Si bilayers, denoted as h-Si1, h-Si2, and h-Si3. To the best of our knowledge, these are the most stable hexagonal bilayer structures of silicene predicted so far. The h-Si2 structure corresponds to the re-DL-Si structure suggested by Morishita *et al.* [277] and the h-Si3 is the hex-OR- $2\times 2$  structure that was recently proposed by Sakai & Oshiyama [278]. These structures are constructed from the structure information provided by the authors in the supplementary material of the corresponding papers and re-optimized with our computational procedure. The h-Si1 is a new stable bilayer h-Si structure that we discovered (see ESI† for details). It is composed of two planar, non-buckled, compressed hexagonal silicene planes that are shifted along the crystal plane. This structure is interesting because although its cohesive energy is close to the former two cases, it has a non-buckled nature. To the best of our knowledge, it is the most stable non-buckled bilayer silicene discovered so far.

The cohesive energies of all the stable bilayer Si systems are given in table 5.6. It is seen that the  $\text{AB}_r^d$  bilayer p-Si system has the lowest energy, about 10 meV/atom less than the most stable hexagonal silicene bilayer h-Si3. This means that the  $\text{AB}_r^d$  p-Si structure is the most stable bilayer silicon structure predicted so far, which is a very surprising result. The AA-stacked p-Si has slightly higher energy than h-Si2 and h-Si3.

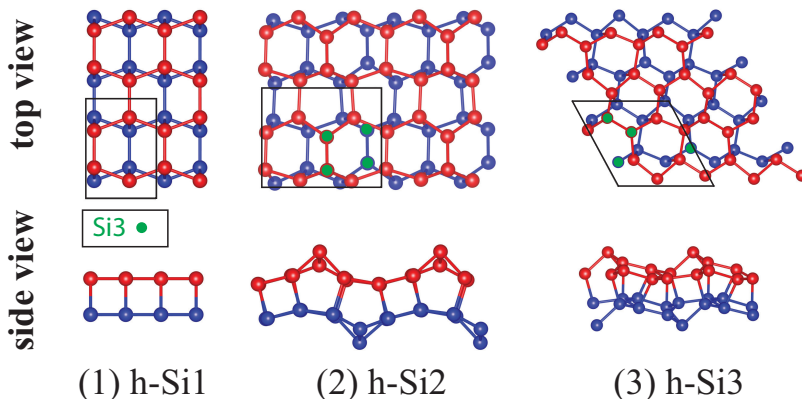


Fig. 5.13 Top and side views of the atomic structures of the  $2\times 2$  supercell of the three examined hexagonal silicene bilayers.

Table 5.6 The interlayer distance  $d_{\text{inter}}$ , the nearest-neighbor bond length range ( $d_{\text{min/max}}$ ) and the cohesive energy per atom  $E_{\text{coh}}$  of the most stable hexagonal bilayer silicene and bilayer p-Si.

structure	$d_{\text{inter}}$ (Å)	$d_{\text{min}}$ (Å)	$d_{\text{max}}$ (Å)	$E_{\text{coh}}$ (eV/atom)
AA bilayer p-Si	0.795	2.363	2.468	-4.129
AB <sub>r</sub> <sup>d</sup> bilayer p-Si	1.896	2.303	2.403	-4.185
h-Si1	2.175	2.358	2.418	-4.115
h-Si2	1.579	2.298	2.453	-4.165
h-Si3	1.378	2.288	2.473	-4.175

## Electronic properties

In the last part of this work, we investigate the electronic properties of few-layer and bulk p-Si. These electronic properties are mainly determined by the electronic spectrum. In Fig. 5.14 and Fig. 5.15a, the electronic band structure of respectively AA and AB<sub>r</sub><sup>d</sup> p-Si multilayers and their bulk counterpart is shown. The band structure of the unstable monolayer is also calculated for comparison. Monolayer p-Si is an indirect semiconductor with a band gap of 0.046 eV (PBE). The band-edge states are mainly composed of  $p_z$  orbitals of Si3 atoms. In contrast to this, all AA-stacked multilayers are metallic. In the case of the AB<sub>r</sub><sup>d</sup> structure, the semiconducting properties of monolayer p-Si are preserved, but the band gap changes somewhat with the number of layers. This can be understood from the position of the electron and hole states which correspond to the conduction band minimum (CBM) and the valence band maximum (VBM), respectively. As seen in Fig. 5.15a, the VBM and CBM states are always localized on the outermost layers. In other words, the electronic properties are mainly determined by the surface region which is nearly independent of the slab thickness. For AB<sub>r</sub>-stacked bulk p-Si, there is no surface and the VBM and CBM correspond to bulk states. This explains the much larger band gap (1.33 eV) in the bulk case.

## Summary

In this work, we proposed several stable structures for few-layer pentasilicene. The stability of these structures was confirmed via their phonon spectrum, finite-temperature molecular dynamics, and their mechanical properties. The type of

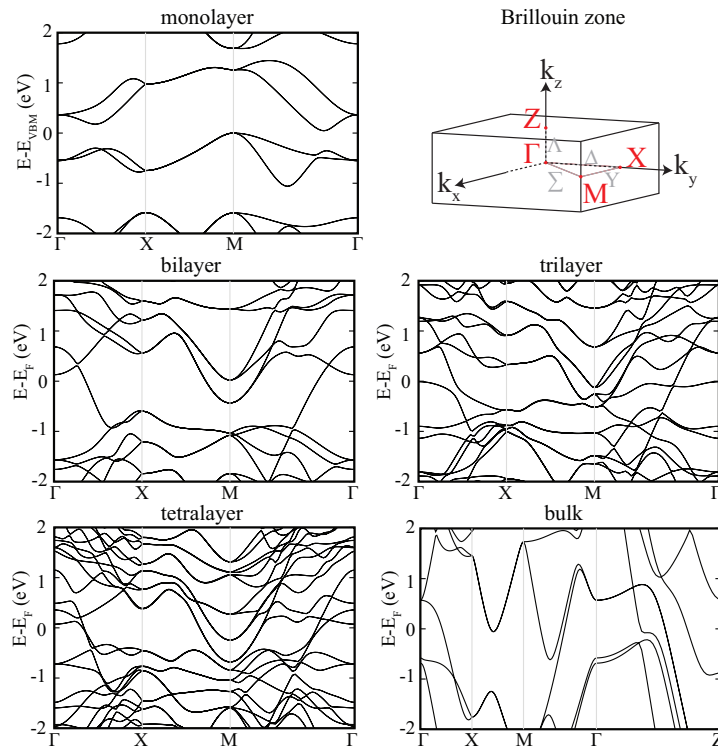


Fig. 5.14 Electronic band structure of AA stacked few-layer and bulk p-Si, and a schematic of the first Brillouin zone.

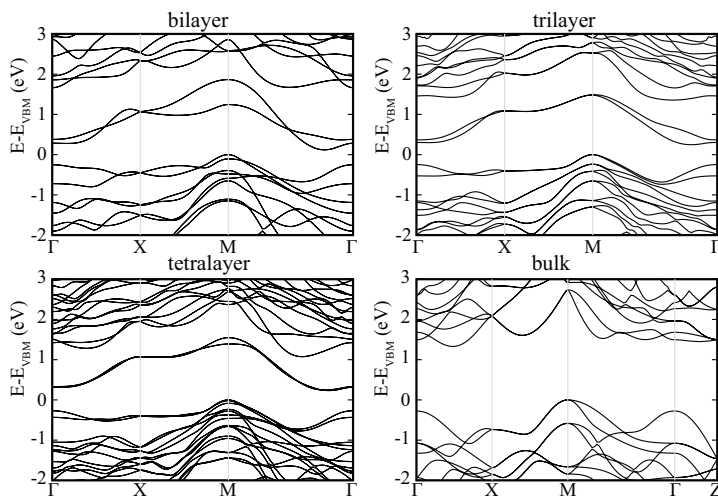
stacking mode, AA or AB, of few-layer pentasilicene has a crucial influence on the electronic properties: AA-stacked systems are metallic, while  $AB_r^d$  stacked ones are semiconducting. Surprisingly, the  $AB_r^d$  stacked bilayer pentasilicene has lower energy than the most stable bilayer hexagonal silicene structures, which makes it the most stable predicted form of bilayer silicon.

## 5.2 Mechanical strain

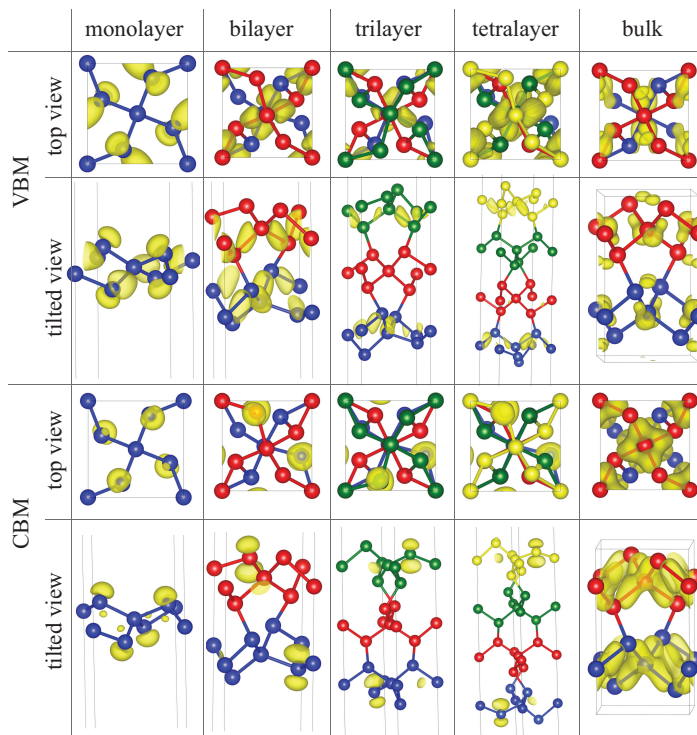
### 5.2.1 Strain modulation of band gap of pentasilicene<sup>3</sup>

Strain is an effective tool to modulate the electronic properties of 2D semiconductors. Here we investigate the band gap variation of  $AB_r^d$  bilayer p-Si with respect to both uniaxial and biaxial tensile strain up to 10% , see Fig. 5.16(a).

<sup>3</sup>This work is published in: P6.



(a) Electronic band structures



(b) Charge density

Fig. 5.15 (a) Electronic band structure of  $AB_r^d$  stacked few-layer and  $AB_r$  stacked bulk p-Si, and (b) the corresponding charge distribution of CBM and VBM. The results for the monolayer are shown for comparison.

We observe, in both cases, a small kink in the band gaps that gives rise to non-monotonic behavior. For uniaxial strain, the band gap first increases from 0.12 eV to 0.27 eV at 4% strain, and then decreases again until the system becomes metallic at 10%. A similar behavior is found for biaxial strain where the band gap increases up to 0.25 eV at 2% strain and the system becomes metallic at 6% tensile strain. In order to explain the kink in the band gap evolution, we plot the relevant band edges with respect to the vacuum level as a function of strain. In the figure, the high-symmetry points of the Brillouin zone where the edges are located are given between round brackets, while the notation VBM-1 is used to denote the first band below the VBM (in the band structure without strain). As can be seen from Fig. 5.16(b) and (c), while the  $\text{CBM}(\Sigma)$ s slightly decrease in a monotonic way, the  $\text{VBM}(M)$  crosses the  $\text{VBM-1}(M)$  once under uniaxial strain, and two crosses, first the  $\text{VBM}(M)$  switches its position from M to Y, and then back to M but for a lower band, occur for biaxial strain. These crosses give rise to abrupt changes in the band gaps.

We found that it is possible to engineer the electronic properties by tensile strain. Both quantitative and qualitative changes can be induced in this way. We explained the variation of the band gap from the band edge crossings that occur under strain. In conclusion, the proposed bilayer pentasilicene structure is the most stable form of bilayer silicon predicted so far and it was shown to have interesting tunable properties.

### 5.2.2 Variation of vibrational modes under strain in phosphorene<sup>4</sup>

In subsection 4.1.4 we calculated the phonon dispersion of black and blue phosphorene, here we will discuss how the vibrational modes change with strain. In Fig. 5.17 we revisit the phonon dispersion of phosphorene, here the  $\Gamma$  point vibrational modes with their irreducible representations and their frequencies are given.

With the knowledge of the space group and its character table it is possible to assign vibrational modes to each band at the  $\Gamma$ -point. A table of all optical modes together with its frequency and irreducible representation for both struc-

---

<sup>4</sup>This work is published in: P2.

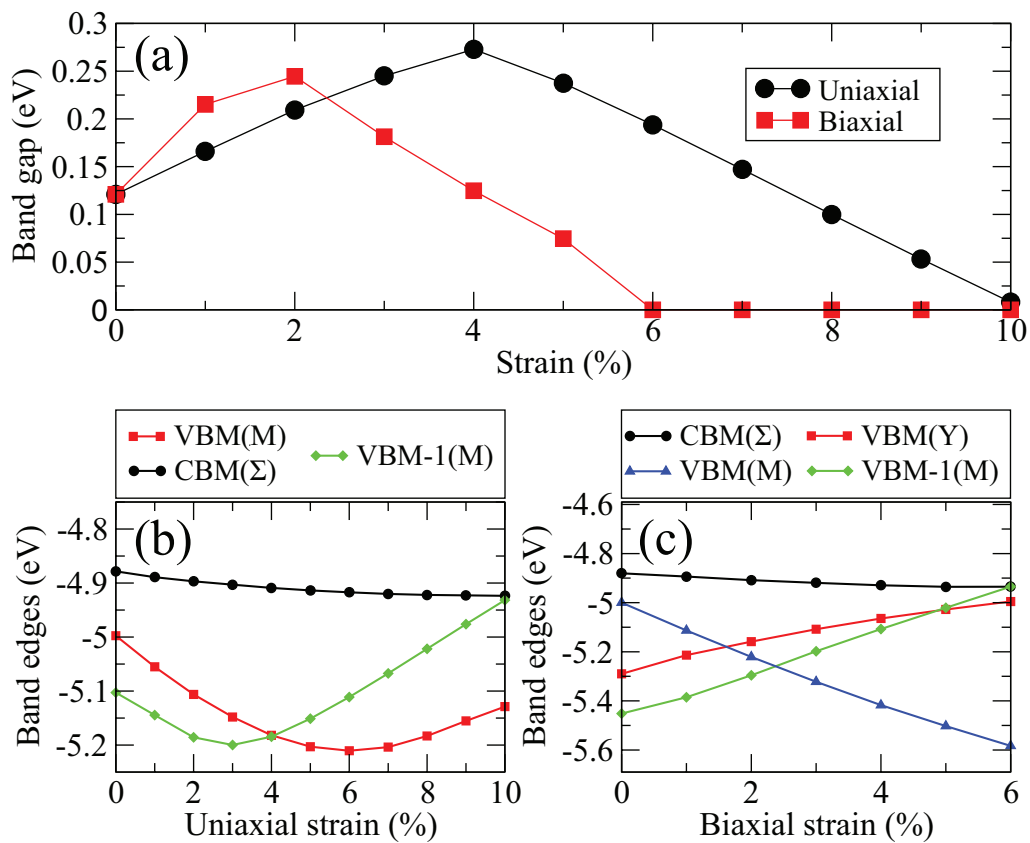


Fig. 5.16 Band gaps (a) and band edges for uniaxially (b) and biaxially (c) strained  $AB_r^d$  bilayer p-Si.

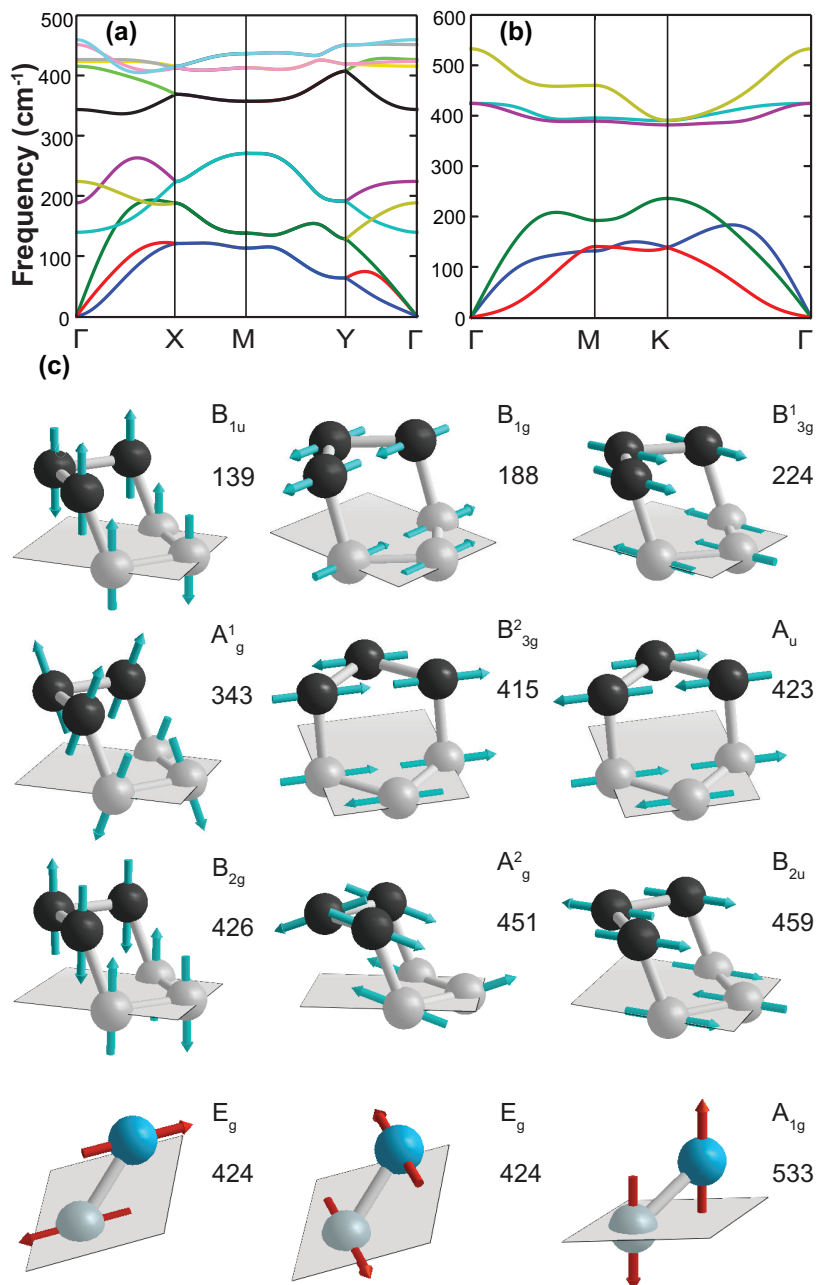


Fig. 5.17 Calculated phonon dispersions for pristine (a) black and (b) blue P. (c) Optical phonon modes together with their frequencies (in units of  $\text{cm}^{-1}$ ) at the  $\Gamma$  point and irreducible representations for black P and blue P. (c) Optical phonon modes together with their frequencies (in units of  $\text{cm}^{-1}$ ) at the  $\Gamma$  point and irreducible representations for black P and blue P.

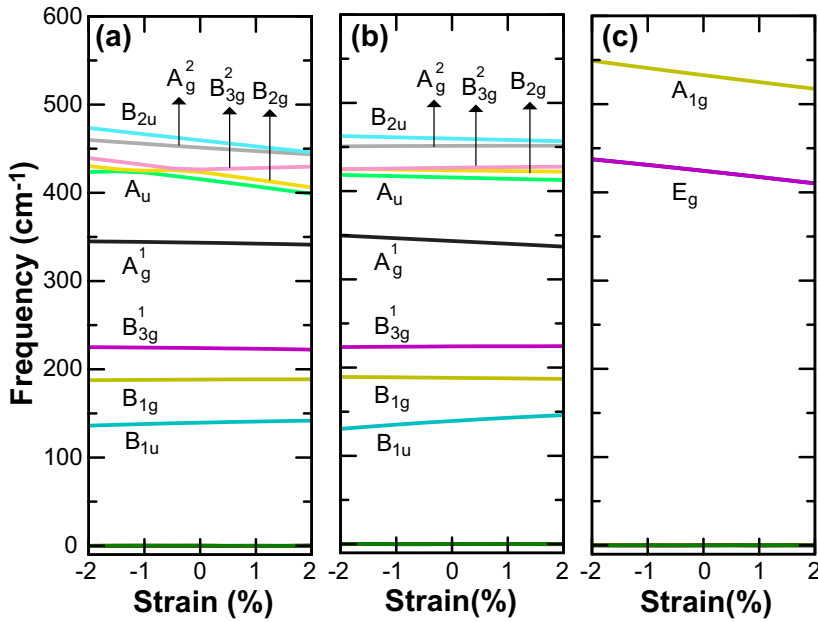


Fig. 5.18 (Color online) Variation of the  $\Gamma$  frequencies with strain: (a) zigzag and (b) armchair direction of black P and (c) blue P.

tures is presented in Fig. 5.17(c) for the stainless structures. In Fig. 5.18, we show the variation of these optical phonons at the  $\Gamma$  point under uniaxial strain. Our calculations agree well with the results of Ref. [164]. The frequency shift by strain can be directly detected using Raman spectroscopy. Depending on the atomic motion of the modes, the magnitude and type of strain, we find that the dependence of the phonon frequency can be different for each mode. Especially, the higher energy optical modes under uniaxial strain, applied along the zigzag direction, exhibit a much larger variation, see Fig. 5.18(a).  $B_{3g}^2$  mode of black P has a different behavior under tensile and compressive strains along the zigzag direction. Applying a tensile (compressive) strain increases (decreases) the frequency of  $B_{3g}^2$  mode. The frequency spacing between  $A_g^2$  and  $B_{2u}$  modes decreases when black P is stretched along both zigzag and armchair directions. While the frequency of  $A_g^2$  mode exhibits almost no variation under strain applied along the armchair direction, it significantly varies under strain applied along the zigzag direction. Among the low lying optical modes (i.e.,  $B_{1u}$ ,  $B_{1g}$  and  $B_{3g}^1$ ), the  $B_{1u}$  mode exhibits a larger variation with applied strain.  $E_g$  and  $A_{1g}$  modes of blue P always are red shifted when changing strain from compressive to tensile. Our

results show that by measuring the frequency shift in the particular modes, it is possible to determine the strain distribution in phosphorene.

Our results show that the frequency shift observed in particular modes can be utilized to determine strain distribution in phosphorene.

### 5.2.3 Carrier mobility enhancement in $\text{TiS}_3$ monolayer with strain<sup>5</sup>

### 5.2.4 Carrier mobility

### 5.2.5 Magnetic properties modulation in penta-hexa-graphnene with strain<sup>6</sup>

This new material has an antiferromagnetic (AFM) ground state which transforms to a ferromagnetic (FM) state under strain. The latter state is protected by a small strain-induced energy barrier. These findings can initiate further research to induce magnetism and spin-flip barriers through strain in other metal-free 2D materials.

Strain is an effective way to modulate the electronic properties of materials. There are different ways to induce strain on 2D materials. Roldán *et al.* [279] gave a comprehensive review on the strain engineering on 2D system both from experimental and theoretical view. Here, we apply biaxial strain to our structure and monitor how the total energy of the different magnetic phases change, see Fig. 5.19. We find that an AFM to FM transition occurs for both compressive and tensile strains of approximately 6% and 8%, respectively. Therefore, strained structures of this kind can give a FM ground state, which is more beneficial for applications. The variation of the band gap under strain is plotted in Fig. 5.20. Both the FM and the AFM band gap has a similar qualitative behavior with a small quantitative difference between the two magnetic phases. The tensile strain decreases the band gap monotonically up to 10%, while the compressive strain gives a non-monotonic behavior due to band crossings. From -5% to 10% strain, CBM and VBM are located at the  $\Gamma$  and K high symmetric k-points, respectively. While two transitions of the location of the VBM happen below -5% strain. First,

<sup>5</sup>This work is published in: P7.

<sup>6</sup>This work is published in: P4.

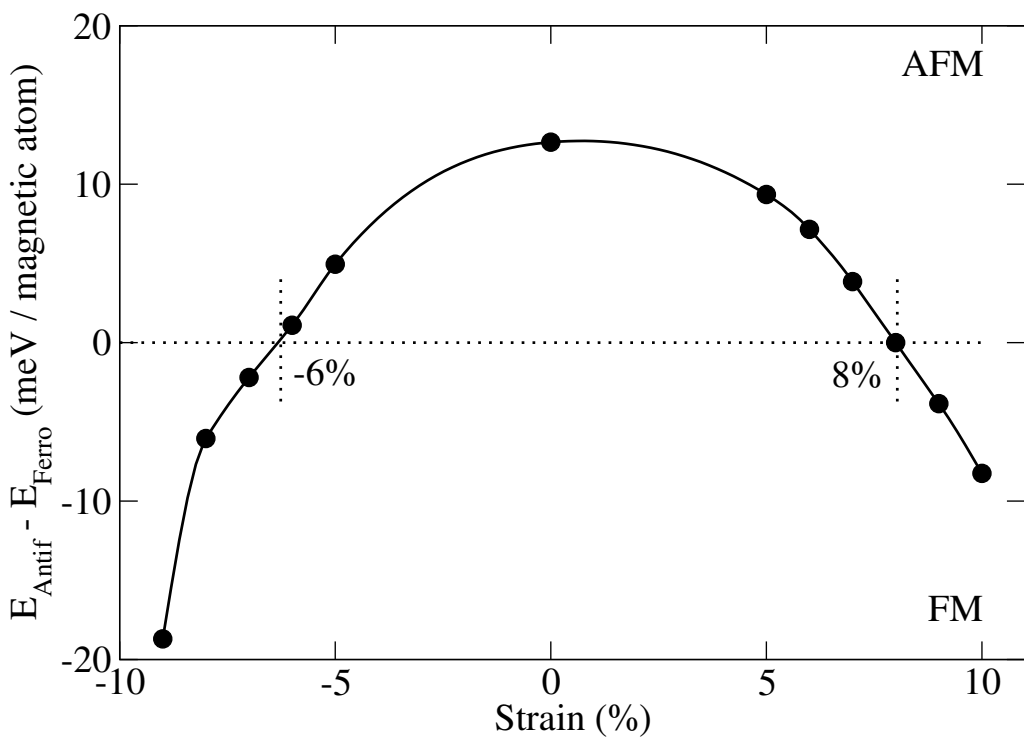


Fig. 5.19 AFM to FM transition of monolayer ph-graphene under strain.

it is shifted to the  $\Gamma$  k-point from the second highest valence band around -8%, and then shifted to the  $\Sigma$  k-path between the  $\Gamma$  and M k-points at -9%.

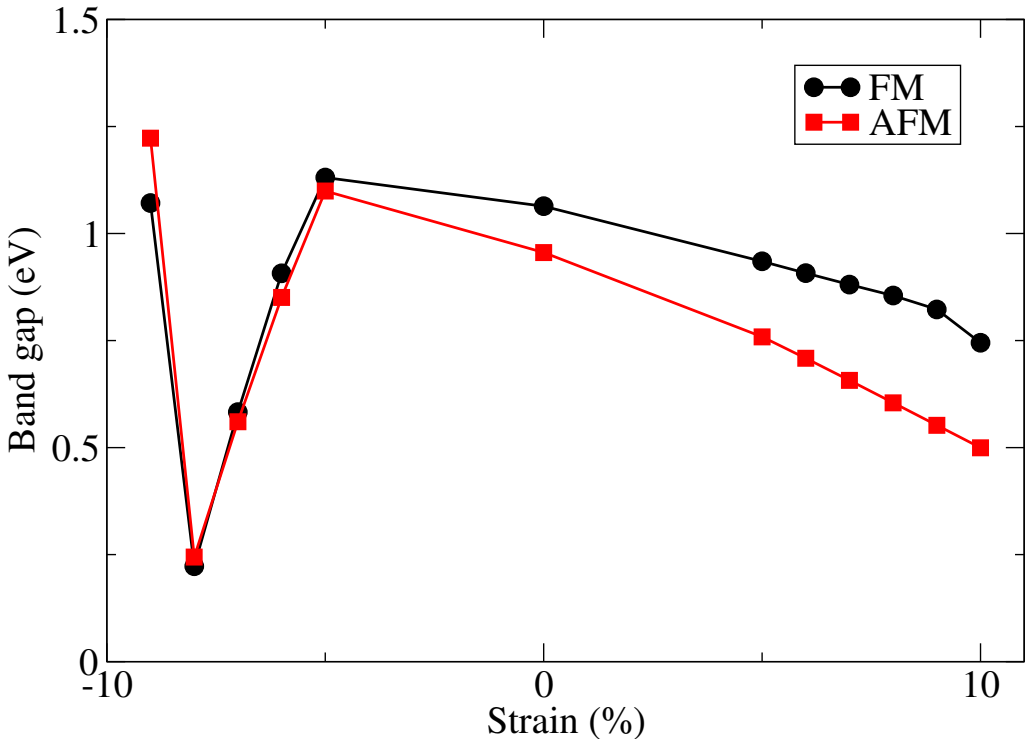


Fig. 5.20 (Color online) Band gap variation of AFM and FM monolayer phosphorene under strain.

As a final property of the two different magnetic ground states, we study the energy barrier for the transition from the FM to AFM state through spin flipping. This calculation is realized by constraining the magnetic moment through a penalty contribution to the total energy in VASP, and rotate one of the moments stepwise through  $180^\circ$ . In this way an energy profile from FM to AFM can be obtained (see Fig. 5.21). The rotation of the magnetic moment was carried along two different planes, one along the zigzag direction and the other along armchair direction, but the difference of the energy profile is negligible. Without strain, there is almost no energy barrier for the transition from the FM to AFM state. However, if the structure is under a 9% tensile strain, in which case the FM state is the ground state, an energy barrier of about 13 meV per magnetic atom arises to return to the AFM state. This is much larger as one consider the energy barrier from the AFM to the FM under the same strain, which is about

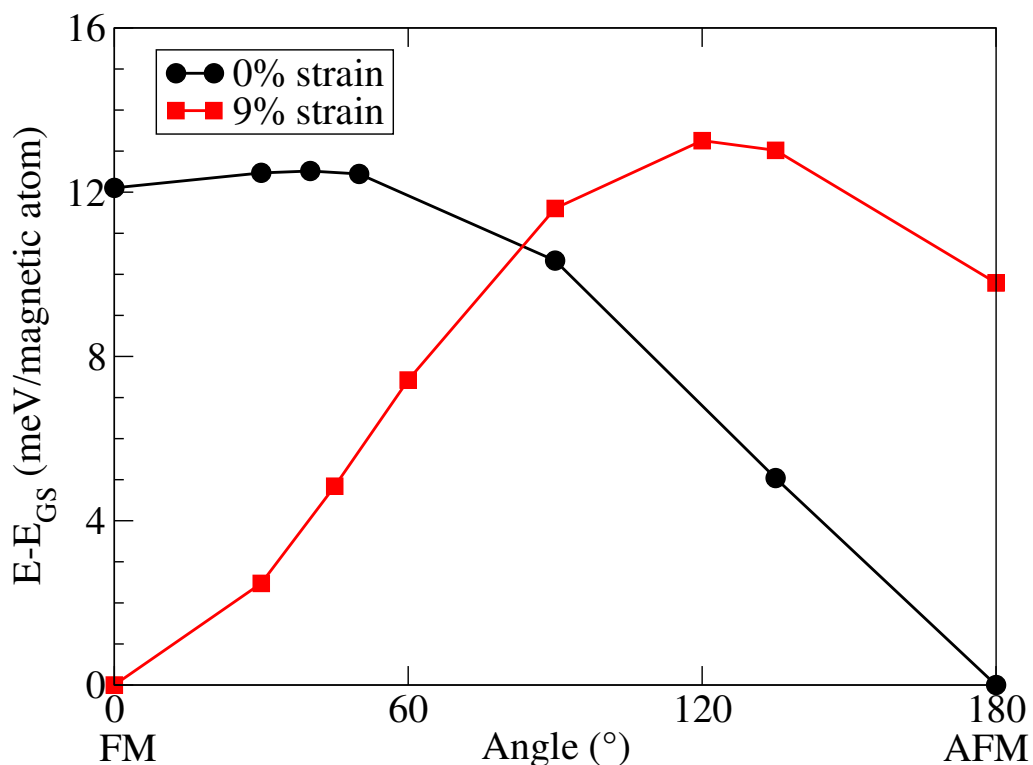


Fig. 5.21 (Color online) AFM to FM transition through spin-flip in monolayer phosphorene.

3.3 meV per magnetic atom. This calculation is performed with the aim to study the stability of each magnetic state, and the possibility to form paramagnetic state even without thermal motion. We found both magnetic state is stable, and there is no tendency to form non-collinear magnetic moment orientation, and possibility of paramagnetic formation is small.

We discovered a strain-driven magnetic ground state transition from AFM to FM around 6% compressive strain and 8% tensile strain. An energy profile with different angles between two local magnetic moments is calculated to study the energy barrier for the transition between FM and AFM. While an energy barrier of about 13 meV/(magnetic atom) protecting the AFM ground state in the pristine case; it is protecting the FM ground state when the system is under 9% tensile strain.

## 5.3 Adatom adsorption

### 5.3.1 Nitrogen edge-decorated graphene nanoribbon<sup>7</sup>

## 5.4 Heterostructures

Another way to explore the property land of materials is to combine different composites to form heterostructure[280–282]. They can be composites made by materials with complementary characters and perform better than each of the material individually, or materials those give new phenomenon and promising properties only when act together. Given the obvious structure anisotropic in 2D materials, there are two types of heterostructures: vertical or lateral, see for example Fig. 5.22. The vertical heterostructures composed of stacks of different 2D materials. They are held together via what holds graphite layers together: van der Waals force. Thus, this type of construction is referred as van der Waals heterostructures. On the other hand, lateral heterostructure[283, 284] is made by joining the edges of different 2D materials and the connection is mostly made through strong bonding, e.g. covalent or ionic. For this case, all the new properties results from the interface. In this section, I will present one for each type of

---

<sup>7</sup>This work will be published as: P10.

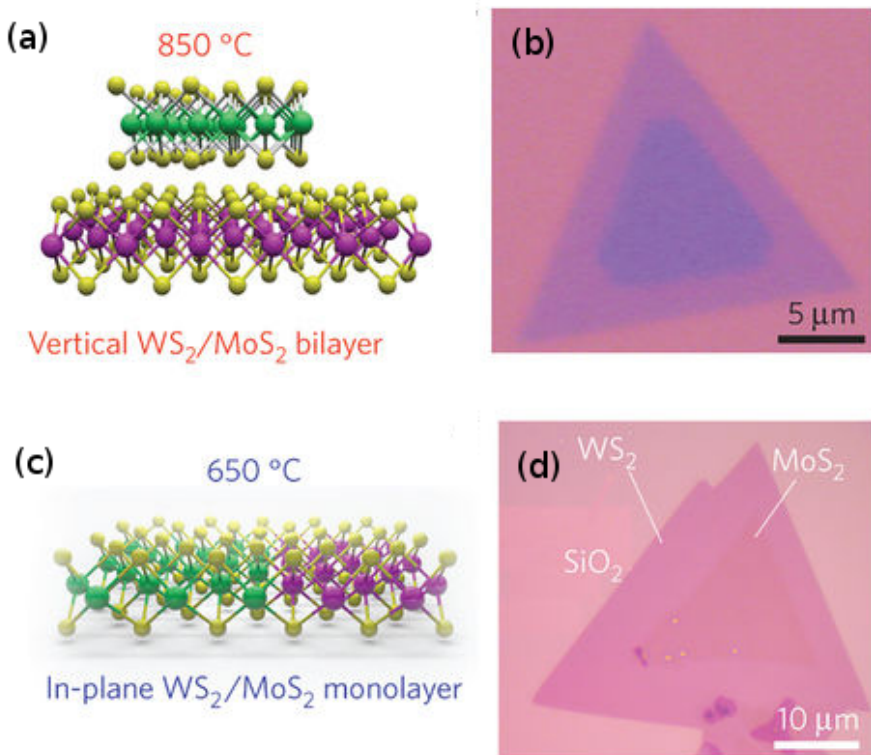


Fig. 5.22 (a) and (d) vertical and (c) and (d) lateral  $\text{WS}_2/\text{MoS}_2$  heterostructures.  
Image adapted from: [285]

the heterostructure and explore one properties. Comparisons will be made to illustrate the advantage of choosing these materials over the homo-structure.

**5.4.1 Electrical transport in 1T/2H/1T MoS<sub>2</sub> lateral heterostructure<sup>8</sup>**

**5.4.2 Li storage and diffusion in MXenes/graphene vertical heterostructure<sup>9</sup>**

## **5.5 Defect induction**

**5.5.1 Faceted blue phosphorene nanotube formed by line defects<sup>10</sup>**

**5.5.2 Electronic structure of penta-hexa defects in graphene<sup>11</sup>**

---

<sup>8</sup>This work is submitted as: P11.

<sup>9</sup>This work will be published as: P9.

<sup>10</sup>This work is published in: P8.

<sup>11</sup>This work is published in: P4.



# **Chapter 6**

## **Conclusions**



# Bibliography

1. Novoselov, K. S., Geim, A. K., Morozov, S. V., Jiang, D., Zhang, Y., Dubonos, S. V., Grigorieva, I. V. & Firsov, A. A. "Electric Field Effect in Atomically Thin Carbon Films". *Science* **306**, 666–669 (2004) (cit. on p. 1).
2. Novoselov, K. S., Jiang, D., Schedin, F., Booth, T. J., Khotkevich, V. V., Morozov, S. V. & Geim, A. K. "Two-dimensional atomic crystals". *Proc. Natl. Acad. Sci. U. S. A.* **102**, 10451–10453 (2005) (cit. on pp. 1, 16).
3. Geim, A. K. & Novoselov, K. S. "The rise of graphene". *Nat. Mater.* **6**, 183–191 (Mar. 2007) (cit. on pp. 1, 5, 6).
4. Of Sciences, T. R. S. A. "The Nobel Prize in Physics 2010 - Information for the public". <[https://www.nobelprize.org/nobel\\_prizes/physics/laureates/2010/popular-physicsprize2010.pdf](https://www.nobelprize.org/nobel_prizes/physics/laureates/2010/popular-physicsprize2010.pdf)> (2010) (cit. on p. 4).
5. Petroski, H. *The Pencil: A History of Design and Circumstance* (Knopf, 1990) (cit. on p. 3).
6. Krishnan, A., Dujardin, E., Treacy, M. M. J., Hugdahl, J., Lynam, S. & Ebbeesen, T. W. "Graphitic cones and the nucleation of curved carbon surfaces". *Nature* **388**, 451–454 (July 1997) (cit. on pp. 3, 5).
7. Ohashi, Y., Koizumi, T., Yoshikawa, T., Hironaka, T. & Shiiki, K. "Size Effect in the In-plane Electrical Resistivity of Very Thin Graphite Crystals". *TANSO* **1997**, 235–238 (1997) (cit. on pp. 3, 5).
8. Dresselhaus, M. S. & Dresselhaus, G. "Intercalation compounds of graphite". *Advances in Physics* **51**, 1–186 (2002) (cit. on p. 3).
9. Shioyama, H. "Cleavage of graphite to graphene". *Journal of Materials Science Letters* **20**, 499–500 (2001) (cit. on p. 3).
10. Peierls, R. "Quelques propriétés typiques des corps solides". fré. *Annales de l'institut Henri Poincaré* **5**, 177–222 (1935) (cit. on p. 3).
11. Landau, L. D. "On the theory of phase transitions. I." *Phys. Z. Sowjet.* **11**, 26 (1937) (cit. on p. 3).
12. Mermin, N. D. "Crystalline Order in Two Dimensions". *Phys. Rev.* **176**, 250–254 (1 Dec. 1968) (cit. on p. 3).
13. Wallace, P. R. "The Band Theory of Graphite". *Phys. Rev.* **71**, 622–634 (9 May 1947) (cit. on pp. 5, 6).

14. Castro Neto, A. H., Guinea, F., Peres, N. M. R., Novoselov, K. S. & Geim, a. K. "The electronic properties of graphene". *Rev. Mod. Phys.* **81**, 109–162 (Jan. 2009) (cit. on pp. 5, 41).
15. Kroto, H. W., Heath, J. R., O'Brien, S. C., Curl, R. F. & Smalley, R. E. "C<sub>60</sub>: Buckminsterfullerene". *Nature* **318**, 162–163 (Nov. 1985) (cit. on p. 5).
16. Krätschmer, W., Lamb, L. D., Fostiropoulos, K. & Huffman, D. R. "Solid C<sub>60</sub>: a new form of carbon". *Nature* **347**, 354–358 (Sept. 1990) (cit. on p. 5).
17. Iijima, S. & Ichihashi, T. "Single-shell carbon nanotubes of 1-nm diameter". *Nature* **363**, 603–605 (June 1993) (cit. on p. 5).
18. Baughman, R. H., Zakhidov, A. A. & de Heer, W. A. "Carbon Nanotubes—the Route Toward Applications". *Science* **297**, 787–792 (2002) (cit. on p. 5).
19. Novoselov, K. S., Geim, A. K., Morozov, S. V., Jiang, D., Katsnelson, M. I., Grigorieva, I. V., Dubonos, S. V. & Firsov, A. A. "Two-dimensional gas of massless Dirac fermions in graphene". *Nature* **438**, 197–200 (Nov. 2005) (cit. on p. 6).
20. Katsnelson, M. I., Novoselov, K. S. & Geim, A. K. "Chiral tunnelling and the Klein paradox in graphene". *Nat Phys* **2**, 620–625 (Sept. 2006) (cit. on p. 6).
21. Novoselov, K. S., Jiang, Z., Zhang, Y., Morozov, S. V., Stormer, H. L., Zeitler, U., Maan, J. C., Boebinger, G. S., Kim, P. & Geim, A. K. "Room-Temperature Quantum Hall Effect in Graphene". *Science* **315**, 1379–1379 (2007) (cit. on p. 6).
22. Güttinger, J., Molitor, F., Stampfer, C., Schnez, S., Jacobsen, A., Dröscher, S., Ihn, T. & Ensslin, K. "Transport through graphene quantum dots". *Reports on Progress in Physics* **75**, 126502 (2012) (cit. on p. 7).
23. Lee, C., Wei, X., Kysar, J. W. & Hone, J. "Measurement of the Elastic Properties and Intrinsic Strength of Monolayer Graphene". *Science* **321**, 385–388 (2008) (cit. on pp. 6, 49).
24. Bolotin, K., Sikes, K., Jiang, Z., Klima, M., Fudenberg, G., Hone, J., Kim, P. & Stormer, H. "Ultrahigh electron mobility in suspended graphene". *Solid State Communications* **146**, 351–355 (2008) (cit. on p. 7).
25. Bolotin, K. I., Sikes, K. J., Hone, J., Stormer, H. L. & Kim, P. "Temperature-Dependent Transport in Suspended Graphene". *Phys. Rev. Lett.* **101**, 096802 (9 Aug. 2008) (cit. on p. 7).
26. Balandin, A. A., Ghosh, S., Bao, W., Calizo, I., Teweldebrhan, D., Miao, F. & Lau, C. N. "Superior Thermal Conductivity of Single-Layer Graphene". *Nano Lett.* **8**, 902–907 (2008) (cit. on p. 7).

27. Ci, L., Song, L., Jin, C., Jariwala, D., Wu, D., Li, Y., Srivastava, A., Wang, Z. F., Storr, K., Balicas, L., Liu, F. & Ajayan, P. M. "Atomic layers of hybridized boron nitride and graphene domains". *Nat. Mater.* **9**, 430–435 (Feb. 2010) (cit. on p. 7).
28. Zhou, S. Y., Gweon, G.-H., Fedorov, A., First, P., De Heer, W., Lee, D.-H., Guinea, F., Neto, A. C. & Lanzara, A. "Substrate-induced bandgap opening in epitaxial graphene". *Nat. Mater.* **6**, 770–775 (2007) (cit. on p. 7).
29. McCann, E. "Asymmetry gap in the electronic band structure of bilayer graphene". *Physical Review B* **74**, 161403 (2006) (cit. on p. 7).
30. Castro, E. V., Novoselov, K., Morozov, S., Peres, N., Dos Santos, J. L., Nilsson, J., Guinea, F., Geim, A. & Neto, A. C. "Biased bilayer graphene: semiconductor with a gap tunable by the electric field effect". *Phys. Rev. Lett.* **99**, 216802 (2007) (cit. on p. 7).
31. Elias, D. C., Nair, R. R., Mohiuddin, T. M. G., Morozov, S. V., Blake, P., Halsall, M. P., Ferrari, A. C., Boukhvalov, D. W., Katsnelson, M. I., Geim, A. K. & Novoselov, K. S. "Control of Graphene's Properties by Reversible Hydrogenation: Evidence for Graphane". *Science* **323**, 610–613 (2009) (cit. on pp. 7, 8).
32. Jeon, K.-J., Lee, Z., Pollak, E., Moreschini, L., Bostwick, A., Park, C.-M., Mendelsberg, R., Radmilovic, V., Kostecki, R., Richardson, T. J. & Rotenberg, E. "Fluorographene: A Wide Bandgap Semiconductor with Ultraviolet Luminescence". *ACS Nano* **5**, 1042–1046 (2011) (cit. on pp. 7, 9).
33. Zhou, S., Siegel, D., Fedorov, A. & Lanzara, A. "Metal to insulator transition in epitaxial graphene induced by molecular doping". *Phys. Rev. Lett.* **101**, 086402 (2008) (cit. on p. 7).
34. Nakada, K., Fujita, M., Dresselhaus, G. & Dresselhaus, M. S. "Edge state in graphene ribbons: Nanometer size effect and edge shape dependence". *Phys. Rev. B* **54**, 17954–17961 (24 Dec. 1996) (cit. on p. 7).
35. Barone, V., Hod, O. & Scuseria, G. E. "Electronic Structure and Stability of Semiconducting Graphene Nanoribbons". *Nano Lett.* **6**, 2748–2754 (2006) (cit. on p. 7).
36. Yang, Z., Sun, Y., Alemany, L. B., Narayanan, T. N. & Billups, W. E. "Birch Reduction of Graphite. Edge and Interior Functionalization by Hydrogen". *J. Am. Chem. Soc.* **134**, 18689–18694 (2012) (cit. on p. 8).
37. Burgess, J. S., Matis, B. R., Robinson, J. T., Bulat, F. A., Perkins, F. K., Houston, B. H. & Baldwin, J. W. "Tuning the electronic properties of graphene by hydrogenation in a plasma enhanced chemical vapor deposition reactor". *Carbon* **49**, 4420–4426 (2011) (cit. on p. 8).
38. Wang, Y., Xu, X., Lu, J., Lin, M., Bao, Q., Ozyilmaz, B. & Loh, K. P. "Toward high throughput interconvertible graphane-to-graphene growth and patterning". *ACS nano* **4**, 6146–6152 (2010) (cit. on p. 8).

39. Samarakoon, D. K. & Wang, X.-Q. "Chair and Twist-Boat Membranes in Hydrogenated Graphene". *ACS Nano* **3**, 4017–4022 (2009) (cit. on p. 8).
40. Ilyin, A., Guseinov, N., Tsyganov, I. & Nemkaeva, R. "Computer simulation and experimental study of graphane-like structures formed by electrolytic hydrogenation". *Physica E: Low-dimensional Systems and Nanosstructures* **43**, 1262–1265 (2011) (cit. on p. 8).
41. Muñoz, E., Singh, A. K., Ribas, M. A., Penev, E. S. & Yakobson, B. I. "The ultimate diamond slab: GraphAne versus graphEne". *Diamond and Related Materials* **19**. Proceedings of Diamond 2009, The 20th European Conference on Diamond, Diamond-Like Materials, Carbon Nanotubes and Nitrides, Part 1, 368–373 (2010) (cit. on p. 8).
42. Zhou, J., Wang, Q., Sun, Q., Chen, X. S., Kawazoe, Y. & Jena, P. "Ferromagnetism in Semihydrogenated Graphene Sheet". *Nano Lett.* **9**, 3867–3870 (Nov. 2009) (cit. on pp. 8, 71).
43. Shkrebtii, A. I., Heritage, E., McNelles, P., Cabellos, J. L. & Mendoza, B. S. "Graphene and graphane functionalization with hydrogen: electronic and optical signatures". *physica status solidi (c)* **9**, 1378–1383 (2012) (cit. on p. 8).
44. Sofo, J. O., Chaudhari, A. S. & Barber, G. D. "Graphane: A two-dimensional hydrocarbon". *Phys. Rev. B* **75**, 153401 (15 Apr. 2007) (cit. on p. 9).
45. Leenaerts, O., Peelaers, H., Hernández-Nieves, A., Partoens, B. & Peeters, F. "First-principles investigation of graphene fluoride and graphane". *Physical Review B* **82**, 195436 (2010) (cit. on p. 9).
46. Zhu, M., Xie, X., Guo, Y., Chen, P., Ou, X., Yu, G. & Liu, M. "Fluorographene nanosheets with broad solvent dispersibility and their applications as a modified layer in organic field-effect transistors". *Phys. Chem. Chem. Phys.* **15**, 20992–21000 (48 2013) (cit. on pp. 8, 9).
47. Samarakoon, D. K., Chen, Z., Nicolas, C. & Wang, X.-Q. "Structural and Electronic Properties of Fluorographene". *Small* **7**, 965–969 (Apr. 2011) (cit. on p. 9).
48. Nair, R. R., Ren, W., Jalil, R., Riaz, I., Kravets, V. G., Britnell, L., Blake, P., Schedin, F., Mayorov, A. S., Yuan, S., et al. "Fluorographene: A Two-Dimensional Counterpart of Teflon". *Small* **6**, 2877–2884 (2010) (cit. on p. 9).
49. Lin, C.-L., Arafune, R., Kawahara, K., Kanno, M., Tsukahara, N., Minamitani, E., Kim, Y., Kawai, M. & Takagi, N. "Substrate-Induced Symmetry Breaking in Silicene". *Phys. Rev. Lett.* **110**, 076801 (7 Feb. 2013) (cit. on pp. 10, 11).
50. Matthes, L., Pulci, O. & Bechstedt, F. "Massive Dirac quasiparticles in the optical absorbance of graphene, silicene, germanene, and tinene". *J. Phys.: Condens. Matter* **25**, 395305 (2013) (cit. on pp. 10, 11).

51. Balendhran, S., Walia, S., Nili, H., Sriram, S. & Bhaskaran, M. "Elemental Analogues of Graphene: Silicene, Germanene, Stanene, and Phosphorene". *Small* **11**, 640–652 (2015) (cit. on p. 10).
52. Garcia, J. C., de Lima, D. B., Assali, L. V. C. & Justo, J. F. "Group IV Graphene- and Graphane-Like Nanosheets". *The Journal of Physical Chemistry C* **115**, 13242–13246 (2011) (cit. on p. 10).
53. Manjanath, A., Kumar, V. & Singh, A. K. "Mechanical and electronic properties of pristine and Ni-doped Si, Ge, and Sn sheets". *Phys. Chem. Chem. Phys.* **16**, 1667–1671 (4 2014) (cit. on p. 11).
54. Vogt, P., De Padova, P., Quaresima, C., Avila, J., Frantzeskakis, E., Asensio, M. C., Resta, A., Ealet, B. & Le Lay, G. "Silicene: compelling experimental evidence for graphenelike two-dimensional silicon". *Phys. Rev. Lett.* **108**, 155501 (2012) (cit. on p. 11).
55. Li, L., Lu, S.-z., Pan, J., Qin, Z., Wang, Y.-q., Wang, Y., Cao, G.-y., Du, S. & Gao, H.-J. "Buckled germanene formation on Pt (111)". *Advanced Materials* **26**, 4820–4824 (2014) (cit. on p. 11).
56. Lin, C.-L., Arafune, R., Kawahara, K., Tsukahara, N., Minamitani, E., Kim, Y., Takagi, N. & Kawai, M. "Structure of silicene grown on Ag (111)". *Applied Physics Express* **5**, 045802 (2012) (cit. on p. 11).
57. Kaloni, T. P. & Schwingenschlögl, U. "Weak interaction between germanene and GaAs (0001) by H intercalation: a route to exfoliation". *J. Appl. Phys.* **114**, 184307 (2013) (cit. on p. 11).
58. Alem, N., Erni, R., Kisielowski, C., Rossell, M. D., Gannett, W. & Zettl, A. "Atomically thin hexagonal boron nitride probed by ultrahigh-resolution transmission electron microscopy". *Physical Review B* **80**, 155425 (2009) (cit. on p. 11).
59. Zhuang, H. L. & Hennig, R. G. "Electronic structures of single-layer boron pnictides". *Appl. Phys. Lett.* **101**, 153109 (2012) (cit. on p. 12).
60. Bosak, A., Serrano, J., Krisch, M., Watanabe, K., Taniguchi, T. & Kanda, H. "Elasticity of hexagonal boron nitride: Inelastic x-ray scattering measurements". *Phys. Rev. B* **73**, 041402 (4 Jan. 2006) (cit. on p. 12).
61. Jo, I., Pettes, M. T., Kim, J., Watanabe, K., Taniguchi, T., Yao, Z. & Shi, L. "Thermal Conductivity and Phonon Transport in Suspended Few-Layer Hexagonal Boron Nitride". *Nano Lett.* **13**, 550–554 (2013) (cit. on p. 12).
62. Li, L. H. & Chen, Y. "Atomically Thin Boron Nitride: Unique Properties and Applications". *Adv. Funct. Mater.* **26**, 2594–2608 (Apr. 2016) (cit. on p. 12).
63. Lee, G.-H., Yu, Y.-J., Cui, X., Petrone, N., Lee, C.-H., Choi, M. S., Lee, D.-Y., Lee, C., Yoo, W. J., Watanabe, K., Taniguchi, T., Nuckolls, C., Kim, P. & Hone, J. "Flexible and Transparent MoS<sub>2</sub> Field-Effect Transistors on Hexagonal Boron Nitride-Graphene Heterostructures". *ACS Nano* **7**, 7931–7936 (2013) (cit. on p. 12).

64. R., D., F., Y., MericI., LeeC., WangL., SorgenfreiS., WatanabeK., TaniguchiT., KimP., L., S. & HoneJ. "Boron nitride substrates for high-quality graphene electronics". *Nat Nano* **5**, 722–726 (Oct. 2010) (cit. on p. 12).
65. Benjah-bmm27 (Own work) [Public domain], v. W. C. "Boron-nitride-(hexagonal)-side-3D-balls". <[https://commons.wikimedia.org/wiki/File%3ABoron-nitride-\(hexagonal\)-side-3D-balls.png](https://commons.wikimedia.org/wiki/File%3ABoron-nitride-(hexagonal)-side-3D-balls.png)> (2007) (cit. on p. 12).
66. Wang, Q. H., Kalantar-Zadeh, K., Kis, A., Coleman, J. N. & Strano, M. S. "Electronics and optoelectronics of two-dimensional transition metal dichalcogenides". *Nat. Nanotechnol.* **7**, 699–712 (Nov. 2012) (cit. on pp. 13, 60).
67. Zhu, Z. Y., Cheng, Y. C. & Schwingenschlögl, U. "Giant spin-orbit-induced spin splitting in two-dimensional transition-metal dichalcogenide semiconductors". *Phys. Rev. B* **84**, 153402 (15 Oct. 2011) (cit. on p. 13).
68. Kim, J., Byun, S., Smith, A. J., Yu, J. & Huang, J. "Enhanced Electrocatalytic Properties of Transition-Metal Dichalcogenides Sheets by Spontaneous Gold Nanoparticle Decoration". *The Journal of Physical Chemistry Letters* **4**, 1227–1232 (2013) (cit. on p. 13).
69. Huang, Y., Miao, Y.-E., Zhang, L., Tjiu, W. W., Pan, J. & Liu, T. "Synthesis of few-layered MoS<sub>2</sub> nanosheet-coated electrospun SnO<sub>2</sub> nanotube heterostructures for enhanced hydrogen evolution reaction". *Nanoscale* **6**, 10673–10679 (18 2014) (cit. on p. 13).
70. Radisavljevic, B., Radenovic, A., Brivio, J., Giacometti, V. & Kis, A. "Single-layer MoS<sub>2</sub> transistors". *Nature Nanotech.* **6**, 147–150 (Jan. 2011) (cit. on p. 13).
71. Sun, G., Liu, J., Zhang, X., Wang, X., Li, H., Yu, Y., Huang, W., Zhang, H. & Chen, P. "Fabrication of Ultralong Hybrid Microfibers from Nanosheets of Reduced Graphene Oxide and Transition-Metal Dichalcogenides and their Application as Supercapacitors". *Angewandte Chemie* **126**, 12784–12788 (2014) (cit. on p. 13).
72. Chang, K. & Chen, W. "I-Cysteine-Assisted Synthesis of Layered MoS<sub>2</sub>/Graphene Composites with Excellent Electrochemical Performances for Lithium Ion Batteries". *ACS Nano* **5**, 4720–4728 (2011) (cit. on p. 13).
73. Chen, D., Ji, G., Ding, B., Ma, Y., Qu, B., Chen, W. & Lee, J. Y. "In situ nitrogenated graphene-few-layer WS<sub>2</sub> composites for fast and reversible Li<sup>+</sup> storage". *Nanoscale* **5**, 7890–7896 (17 2013) (cit. on p. 13).
74. Li, Y., Li, Y.-L., Araujo, C. M., Luo, W. & Ahuja, R. "Single-layer MoS<sub>2</sub> as an efficient photocatalyst". *Catal. Sci. Technol.* **3**, 2214–2220 (9 2013) (cit. on p. 13).
75. Parzinger, E., Miller, B., Blaschke, B., Garrido, J. A., Ager, J. W., Holleitner, A. & Wurstbauer, U. "Photocatalytic Stability of Single- and Few-Layer MoS<sub>2</sub>". *ACS Nano* **9**, 11302–11309 (2015) (cit. on p. 13).

76. Cheng, L., Liu, J., Gu, X., Gong, H., Shi, X., Liu, T., Wang, C., Wang, X., Liu, G., Xing, H., Bu, W., Sun, B. & Liu, Z. "PEGylated WS<sub>2</sub> Nanosheets as a Multifunctional Theranostic Agent for in vivo Dual-Modal CT/Photoacoustic Imaging Guided Photothermal Therapy". *Advanced Materials* **26**, 1886–1893 (2014) (cit. on p. 13).
77. Yin, W., Yan, L., Yu, J., Tian, G., Zhou, L., Zheng, X., Zhang, X., Yong, Y., Li, J., Gu, Z. & Zhao, Y. "High-Throughput Synthesis of Single-Layer MoS<sub>2</sub> Nanosheets as a Near-Infrared Photothermal-Triggered Drug Delivery for Effective Cancer Therapy". *ACS Nano* **8**, 6922–6933 (2014) (cit. on p. 13).
78. Chhowalla, M., Shin, H. S., Eda, G., Li, L.-J., Loh, K. P. & Zhang, H. "The chemistry of two-dimensional layered transition metal dichalcogenide nanosheets". *Nat. Chem.* **5**, 263–275 (Mar. 2013) (cit. on p. 14).
79. Wang, X., Ouyang, Y., Li, X., Wang, H., Guo, J. & Dai, H. "Room-Temperature All-Semiconducting Sub-10-nm Graphene Nanoribbon Field-Effect Transistors". *Phys. Rev. Lett.* **100**, 206803 (20 May 2008) (cit. on p. 15).
80. Han, M. Y., Özyilmaz, B., Zhang, Y. & Kim, P. "Energy Band-Gap Engineering of Graphene Nanoribbons". *Phys. Rev. Lett.* **98**, 206805 (20 May 2007) (cit. on p. 15).
81. Son, Y.-W., Cohen, M. L. & Louie, S. G. "Half-metallic graphene nanoribbons". *Nature* **444**, 347–349 (cit. on p. 15).
82. Bandaru, P. R. "Electrical Properties and Applications of Carbon Nanotube Structures". *J. Nanosci. Nanotechnol.* **7**, 1239–1267 (Apr. 2007) (cit. on p. 15).
83. Prasek, J., Drbohlavova, J., Chomoucka, J., Hubalek, J., Jasek, O., Adam, V. & Kizek, R. "Methods for carbon nanotubes synthesis-review". *J. Mater. Chem.* **21**, 15872–15884 (40 2011) (cit. on p. 15).
84. Ferrari, A. C., Bonaccorso, F., Fal'ko, V., Novoselov, K. S., Roche, S., Bøggild, P., Borini, S., Koppens, F. H. L., Palermo, V., Pugno, N., Garrido, J. A., Soridan, R., Bianco, A., Ballerini, L., Prato, M., Lidorikis, E., Kivioja, J., Marinelli, C., Ryhänen, T., Morpurgo, A., Coleman, J. N., Nicolosi, V., Colombo, L., Fert, A., Garcia-Hernandez, M., Bachtold, A., Schneider, G. F., Guinea, F., Dekker, C., Barbone, M., Sun, Z., Gallois, C., Grigorenko, A. N., Konstantatos, G., Kis, A., Katsnelson, M., Vandersypen, L., Loiseau, A., Morandi, V., Neumaier, D., Treossi, E., Pellegrini, V., Polini, M., Tredicucci, A., Williams, G. M., Hee Hong, B., Ahn, J.-H., Min Kim, J., Zirath, H., van Wees, B. J., van der Zant, H., Occhipinti, L., Di Matteo, A., Kinloch, I. A., Seyller, T., Quesnel, E., Feng, X., Teo, K., Rupesinghe, N., Hakonen, P., Neil, S. R. T., Tannock, Q., Löfwander, T. & Kinaret, J. "Science and technology roadmap for graphene, related two-dimensional crystals, and hybrid systems". *Nanoscale* **7**, 4598–4810 (2015) (cit. on p. 16).

85. Ni, Z. H., Ponomarenko, L. A., Nair, R. R., Yang, R., Anissimova, S., Grigorieva, I. V., Schedin, F., Blake, P., Shen, Z. X., Hill, E. H., Novoselov, K. S. & Geim, A. K. "On Resonant Scatterers As a Factor Limiting Carrier Mobility in Graphene". *Nano Lett.* **10**, 3868–3872 (2010) (cit. on p. 16).
86. Mishra, N., Boeckl, J., Motta, N. & Iacopi, F. "Graphene growth on silicon carbide: A review". *physica status solidi (a)* **213**, 2277–2289 (2016) (cit. on p. 17).
87. Petrone, N., Dean, C. R., Meric, I., van der Zande, A. M., Huang, P. Y., Wang, L., Muller, D., Shepard, K. L. & Hone, J. "Chemical Vapor Deposition-Derived Graphene with Electrical Performance of Exfoliated Graphene". *Nano Lett.* **12**, 2751–2756 (2012) (cit. on p. 18).
88. Bae, S., Kim, H., Lee, Y., Xu, X., Park, J.-S., Zheng, Y., Balakrishnan, J., Lei, T., Ri Kim, H., Song, Y. I., Kim, Y.-J., Kim, K. S., Ozyilmaz, B., Ahn, J.-H., Hong, B. H. & Iijima, S. "Roll-to-roll production of 30-inch graphene films for transparent electrodes". *Nat Nano* **5**, 574–578 (Aug. 2010) (cit. on p. 18).
89. Kirklin, S., Saal, J. E., Meredig, B., Thompson, A., Doak, J. W., Aykol, M., Rühl, S. & Wolverton, C. "The Open Quantum Materials Database (OQMD): assessing the accuracy of DFT formation energies". *npj Comput. Mater.* **1**, 15010 (Dec. 2015) (cit. on p. 19).
90. Hohenberg, P. & Kohn, W. "Inhomogeneous Electron Gas". *Phys. Rev.* **136**, B864–B871 (3B Nov. 1964) (cit. on p. 19).
91. Kohn, W. & Sham, L. J. "Self-Consistent Equations Including Exchange and Correlation Effects". *Phys. Rev.* **140**, A1133–A1138 (4A Nov. 1965) (cit. on p. 20).
92. Drummond, N. "QMC Studies of Real Systems". <<http://slideplayer.com/slide/4763755/>> (2017) (cit. on p. 20).
93. Born, M. & Oppenheimer, R. "Zur Quantentheorie der Moleküle". *Annalen der Physik* **389**, 457–484 (1927) (cit. on p. 21).
94. Levy, M. "Universal variational functionals of electron densities, first-order density matrices, and natural spin-orbitals and solution of the v-representability problem". *Proceedings of the National Academy of Sciences* **76**, 6062–6065 (1979) (cit. on p. 21).
95. Perdew, J. P. *Electronic structure of solids' 91* (Akademie Verlag, Berlin, 1991) (cit. on p. 24).
96. Perdew, J. P., Chevary, J. A., Vosko, S. H., Jackson, K. A., Pederson, M. R., Singh, D. J. & Fiolhais, C. "Atoms, molecules, solids, and surfaces: Applications of the generalized gradient approximation for exchange and correlation". *Phys. Rev. B* **46**, 6671–6687 (11 Sept. 1992) (cit. on p. 24).
97. Perdew, J. P., Burke, K. & Ernzerhof, M. "Generalized Gradient Approximation Made Simple [Phys. Rev. Lett. 77, 3865 (1996)]". *Phys. Rev. Lett.* **78**, 1396–1396 (Feb. 1997) (cit. on pp. 24, 78).

98. Peng, Q., Duarte, F. & Paton, R. S. "Computing organic stereoselectivity - from concepts to quantitative calculations and predictions". *Chem. Soc. Rev.* **45**, 6093–6107 (22 2016) (cit. on p. 25).
99. Adamo, C. & Barone, V. "Toward reliable density functional methods without adjustable parameters: The PBE0 model". *The Journal of Chemical Physics* **110**, 6158–6170 (1999) (cit. on p. 24).
100. Heyd, J., Scuseria, G. E. & Ernzerhof, M. "Hybrid functionals based on a screened Coulomb potential". *The Journal of Chemical Physics* **118**, 8207–8215 (2003) (cit. on p. 24).
101. Lucero, M. J., Henderson, T. M. & Scuseria, G. E. "Improved semiconductor lattice parameters and band gaps from a middle-range screened hybrid exchange functional". *J. Phys.: Condens. Matter* **24**, 145504 (2012) (cit. on p. 26).
102. Langreth, D. C. & Perdew, J. P. "Theory of nonuniform electronic systems. I. Analysis of the gradient approximation and a generalization that works". *Phys. Rev. B* **21**, 5469–5493 (12 June 1980) (cit. on p. 26).
103. Fiolhais, C., Nogueira, F. & Marques, M. *A Primer in Density Functional Theory* doi:10.1007/3-540-37072-2 (Springer-Verlag Berlin Heidelberg, 2003) (cit. on p. 27).
104. Godby, R. W., Schlüter, M. & Sham, L. J. "Self-energy operators and exchange-correlation potentials in semiconductors". *Phys. Rev. B* **37**, 10159–10175 (17 June 1988) (cit. on p. 28).
105. Vanderbilt, D. "Soft self-consistent pseudopotentials in a generalized eigenvalue formalism". *Phys. Rev. B* **41**, 7892–7895 (11 Apr. 1990) (cit. on p. 30).
106. Blöchl, P. E. "Projector augmented-wave method". *Phys. Rev. B* **50**, 17953–17979 (Dec. 1994) (cit. on pp. 30, 78).
107. Kresse, G. & Joubert, D. "From ultrasoft pseudopotentials to the projector augmented-wave method". *Phys. Rev. B* **59**, 1758–1775 (3 Jan. 1999) (cit. on p. 30).
108. "List of quantum chemistry and solid-state physics software". <[https://en.wikipedia.org/wiki/List\\_of\\_quantum\\_chemistry\\_and\\_solid-state\\_physics\\_software](https://en.wikipedia.org/wiki/List_of_quantum_chemistry_and_solid-state_physics_software)> (2017) (cit. on p. 31).
109. Lejaeghere, K., Bihlmayer, G., Björkman, T., Blaha, P., Blügel, S., Blum, V., Caliste, D., Castelli, I. E., Clark, S. J., Dal Corso, A., de Gironcoli, S., Deutsch, T., Dewhurst, J. K., Di Marco, I., Draxl, C., Dułak, M., Eriksson, O., Flores-Livas, J. A., Garrity, K. F., Genovese, L., Giannozzi, P., Giantomassi, M., Goedecker, S., Gonze, X., Gränäs, O., Gross, E. K. U., Gulans, A., Gygi, F., Hamann, D. R., Hasnip, P. J., Holzwarth, N. A. W., Iuşan, D., Jochym, D. B., Jollet, F., Jones, D., Kresse, G., Koepernik, K., Küçükbenli, E., Kvashnin, Y. O., Locht, I. L. M., Lubeck, S., Marsman, M., Marzari, N., Nitzsche, U., Nordström, L., Ozaki, T., Paulatto, L., Pickard, C. J., Poelmans, W., Probert,

- M. I. J., Refson, K., Richter, M., Rignanese, G.-M., Saha, S., Scheffler, M., Schlipf, M., Schwarz, K., Sharma, S., Tavazza, F., Thunström, P., Tkatchenko, A., Torrent, M., Vanderbilt, D., van Setten, M. J., Van Speybroeck, V., Wills, J. M., Yates, J. R., Zhang, G.-X. & Cottenier, S. "Reproducibility in density functional theory calculations of solids". *Science* **351**. doi:10.1126/science. aad3000 (2016) (cit. on p. 31).
110. Kresse, G. & Hafner, J. "Ab initio molecular-dynamics simulation of the liquid-metal-amorphous-semiconductor transition in germanium". *Phys. Rev. B* **49**, 14251–14269 (20 May 1994) (cit. on pp. 31, 78).
111. Kresse, G. & Furthmüller, J. "Efficiency of ab-initio total energy calculations for metals and semiconductors using a plane-wave basis set". *Computational Materials Science* **6**, 15–50 (1996) (cit. on pp. 31, 78).
112. Van der Waals, J. D. "Over de Continuiteit van den Gas- en Vloeistoftoestand (on the continuity of the gas and liquid state)". Ph.D. thesis (University of Leiden, 1873) (cit. on p. 33).
113. Partoens, B. & Peeters, F. M. "From graphene to graphite: Electronic structure around the  $K$  point". *Phys. Rev. B* **74**, 075404 (7 Aug. 2006) (cit. on pp. 34, 35).
114. Mak, K. F., Sfeir, M. Y., Misewich, J. A. & Heinz, T. F. "The evolution of electronic structure in few-layer graphene revealed by optical spectroscopy". *Proceedings of the National Academy of Sciences* **107**, 14999–15004 (2010) (cit. on p. 34).
115. Saito, R., Dresselhaus, G. & Dresselhaus, M. *Physical Properties of Carbon Nanotubes* (Imperial College Press, 1998) (cit. on p. 35).
116. Mak, K. F., Lee, C., Hone, J., Shan, J. & Heinz, T. F. "Atomically Thin MoS<sub>2</sub>: A New Direct-Gap Semiconductor". *Phys. Rev. Lett.* **105**, 136805 (13 Sept. 2010) (cit. on p. 36).
117. Padilha, J. E., Peelaers, H., Janotti, A. & Van de Walle, C. G. "Nature and evolution of the band-edge states in MoS<sub>2</sub>: From monolayer to bulk". *Phys. Rev. B* **90**, 205420 (20 Nov. 2014) (cit. on p. 37).
118. photo, S. & royalty-free images on Fotolia.com - Pic 128894654. "sp3 sp2 sp hybrid orbitals". <<https://www.fotolia.com/id/128894654>> (2016) (cit. on p. 38).
119. Coulson, C. & Moffitt, W. "I. The properties of certain strained hydrocarbons". *Phil. Mag.* **40**, 1–35 (1949) (cit. on pp. 37, 74).
120. Wassmann, T., Seitsonen, A. P., Saitta, A. M., Lazzeri, M. & Mauri, F. "Clar's Theory,  $\pi$ -Electron Distribution, and Geometry of Graphene Nanoribbons". *J. Am. Chem. Soc.* **132**, 3440–3451 (Mar. 2010) (cit. on p. 39).
121. Cole, T. "Double bond". <[http://images.slideplayer.com/14/4339766/slides/slide\\_7.jpg](http://images.slideplayer.com/14/4339766/slides/slide_7.jpg)> (2004) (cit. on p. 40).

122. Liu, Z., Wang, J. & Li, J. "Dirac cones in two-dimensional systems: from hexagonal to square lattices". *Phys. Chem. Chem. Phys.* **15**, 18855–18862 (43 2013) (cit. on pp. 41, 42).
123. Wang, J., Deng, S., Liu, Z. & Liu, Z. "The rare two-dimensional materials with Dirac cones". *Natl. Sci. Rev.* **2**, 22–39 (Mar. 2015) (cit. on p. 41).
124. Hasegawa, Y., Konno, R., Nakano, H. & Kohmoto, M. "Zero modes of tight-binding electrons on the honeycomb lattice". *Phys. Rev. B* **74**, 033413 (3 July 2006) (cit. on p. 42).
125. Ackland, G. J., Warren, M. C. & Clark, S. J. "Practical methods in ab initio lattice dynamics". *J. Phys. Condens. Matter* **9**, 7861–7872 (Sept. 1997) (cit. on p. 44).
126. Parlinski, K. "Phonons calculated from first-principles". *École thématique la Société Française la Neutron*. **12**, 161–166 (June 2011) (cit. on p. 44).
127. Kittel, C. *Introduction to Solid State Physics* (John Wiley & Sons, Inc., New York, 2004) (cit. on p. 45).
128. Neek-Amal, M. & Peeters, F. M. "Lattice thermal properties of graphane: Thermal contraction, roughness, and heat capacity". *Phys. Rev. B* **83**, 235437 (23 June 2011) (cit. on p. 45).
129. Brivio, J., Alexander, D. T. L. & Kis, A. "Ripples and Layers in Ultrathin MoS<sub>2</sub> Membranes". *Nano Lett.* **11**, 5148–5153 (2011) (cit. on p. 45).
130. Togo, A. & Tanaka, I. "First principles phonon calculations in materials science". *Scr. Mater.* **108**, 1–5 (2015) (cit. on p. 47).
131. Nye, J. *Physical Properties of Crystals: Their Representation by Tensors and Matrices* (Clarendon Press, 1985) (cit. on pp. 48, 65).
132. Kudin, K. N., Scuseria, G. E. & Yakobson, B. I. "C<sub>2</sub>F". *Phys. Rev. B* **64**, 235406 (23 Nov. 2001) (cit. on p. 49).
133. Topsakal, M., Cahangirov, S. & Ciraci, S. "The response of mechanical and electronic properties of graphane to the elastic strain". *Appl. Phys. Lett.* **96**, 091912 (2010) (cit. on p. 49).
134. Bertolazzi, S., Brivio, J. & Kis, A. "Stretching and Breaking of Ultrathin MoS<sub>2</sub>". *ACS Nano* **5**, 9703–9709 (2011) (cit. on p. 49).
135. Cooper, R. C., Lee, C., Marianetti, C. A., Wei, X., Hone, J. & Kysar, J. W. "Nonlinear elastic behavior of two-dimensional molybdenum disulfide". *Phys. Rev. B* **87**, 035423 (3 Jan. 2013) (cit. on pp. 49, 65).
136. Department, C. U. E. "Materials Data Book". <<http://www-mdp.eng.cam.ac.uk/web/library/enginfo/cueddatabooks/materials.pdf>> (2003) (cit. on p. 49).
137. Born, M. "On the stability of crystal lattices. I". *Mathematical Proceedings of the Cambridge Philosophical Society* **36**, 160–172 (1940) (cit. on p. 49).

138. Mouhat, F. & Coudert, F.-X. "Necessary and sufficient elastic stability conditions in various crystal systems". *Phys. Rev. B* **90**, 224104 (Dec. 2014) (cit. on pp. 49, 115).
139. Liu, H., Neal, A. T., Zhu, Z., Luo, Z., Xu, X., Tomanek, D. & Ye, P. D. "Phosphorene: An Unexplored 2D Semiconductor with a High Hole Mobility". *ACS Nano* **8**, 4033–4041 (2014) (cit. on pp. 51, 53).
140. Li, L., Yu, Y., Ye, G. J., Ge, Q., Ou, X., Wu, H., Feng, D., Chen, X. H. & Zhang, Y. "Black phosphorus field-effect transistors." *Nat. Nanotechnol.* **9**, 372–7 (2014) (cit. on pp. 51, 53).
141. Zhu, Z. & Tománek, D. "Semiconducting Layered Blue Phosphorus: A Computational Study". *Phys. Rev. Lett.* **112**, 176802 (May 2014) (cit. on pp. 52, 53, 57).
142. Guan, J., Zhu, Z. & Tománek, D. "Phase Coexistence and Metal-Insulator Transition in Few-Layer Phosphorene: A Computational Study". *Phys. Rev. Lett.* **113**, 046804 (July 2014) (cit. on p. 52).
143. Wu, M., Fu, H., Zhou, L., Yao, K. & Zeng, X. C. "Nine New Phosphorene Polymorphs with Non-Honeycomb Structures: A Much Extended Family". *Nano Lett.* **15**, 3557–3562 (2015) (cit. on p. 52).
144. Çakır, D., Sahin, H. & Peeters, F. M. "Tuning of the electronic and optical properties of single-layer black phosphorus by strain". *Phys. Rev. B* **90**, 205421 (20 Nov. 2014) (cit. on pp. 53, 57).
145. Wang, X., Jones, A. M., Seyler, K. L., Tran, V., Jia, Y., Zhao, H., Wang, H., Yang, L., Xu, X. & Xia, F. "Highly anisotropic and robust excitons in monolayer black phosphorus". *Nat. Nanotechnol.* **10**, 517–521 (Apr. 2015) (cit. on p. 53).
146. Maruyama, Y., Suzuki, S., Kobayashi, K. & Tanuma, S. "Synthesis and some properties of black phosphorus single crystals". *Physica B+C* **105**, 99–102 (1981) (cit. on p. 53).
147. Narita, S., Akahama, Y., Tsukiyama, Y., Muro, K., Mori, S., Endo, S., Taniguchi, M., Seki, M., Suga, S., Mikuni, A. & Kanzaki, H. "Electrical and optical properties of black phosphorus single crystals". *Physica B+C* **117**, 422–424 (1983) (cit. on p. 53).
148. Jain, A. & McGaughey, A. J. H. "Strongly anisotropic in-plane thermal transport in single-layer black phosphorene". *Sci. Rep.* **5**, 8501 (2015) (cit. on p. 53).
149. Wei, Q. & Peng, X. "Superior mechanical flexibility of phosphorene and few-layer black phosphorus". *Appl. Phys. Lett.* **104**, 251915 (2014) (cit. on p. 53).
150. Kou, L., Frauenheim, T. & Chen, C. "Phosphorene as a Superior Gas Sensor: Selective Adsorption and Distinct I-V Response". *J. Phys. Chem. Lett.* **5**, 2675–2681 (2014) (cit. on p. 53).

151. Tahir, M., Vasilopoulos, P. & Peeters, F. M. "Magneto-optical transport properties of monolayer phosphorene". *preprint arXiv:1505.06780* (May 2015) (cit. on p. 53).
152. Zhou, X., Zhang, R., Sun, J., Zou, Y., Zhou, G., Zhai, F. & Chang, K. "Landau levels and magneto-transport property of monolayer phosphorene". *arXiv preprint arXiv:1411.4275* (2014) (cit. on p. 53).
153. Mounet, N. & Marzari, N. "First-principles determination of the structural, vibrational and thermodynamic properties of diamond, graphite, and derivatives". *Phys. Rev. B* **71**, 205214 (20 May 2005) (cit. on pp. 54, 55, 59).
154. Çakır, D., Peeters, F. M. & Sevik, C. "Mechanical and thermal properties of h-MX<sub>2</sub> (M = Cr, Mo, W; X = O, S, Se, Te) monolayers: A comparative study". *Appl. Phys. Lett.* **104**, 203110 (May 2014) (cit. on pp. 54, 58, 65).
155. Sevik, C. "Assessment on lattice thermal properties of two-dimensional honeycomb structures: Graphene, h-BN, h-MoS<sub>2</sub>, and h-MoSe<sub>2</sub>". *Phys. Rev. B* **89**, 035422 (3 Jan. 2014) (cit. on pp. 54, 58).
156. Baroni, S., Giannozzi, P. & Isaev, E. "Density-Functional Perturbation Theory for Quasi-Harmonic Calculations". *Reviews in Mineralogy and Geochemistry* **71**, 39–57 (2010) (cit. on p. 54).
157. Hamdi, I., Aouissi, M., Qteish, A. & Meskini, N. "Pressure dependence of vibrational, thermal, and elastic properties of ZnSe: An ab initio study". *Phys. Rev. B* **73**, 174114 (17 May 2006) (cit. on p. 54).
158. Grabowski, B., Ismer, L., Hickel, T. & Neugebauer, J. "Ab initio up to the melting point: Anharmonicity and vacancies in aluminum". *Phys. Rev. B* **79**, 134106 (13 Apr. 2009) (cit. on p. 54).
159. Karki, B. B., Wentzcovitch, R. M., de Gironcoli, S. & Baroni, S. "High-pressure lattice dynamics and thermoelasticity of MgO". *Phys. Rev. B* **61**, 8793–8800 (13 Apr. 2000) (cit. on p. 54).
160. Pavone, P., Karch, K., Schütt, O., Strauch, D., Windl, W., Giannozzi, P. & Baroni, S. "Ab initio lattice dynamics of diamond". *Phys. Rev. B* **48**, 3156–3163 (5 Aug. 1993) (cit. on p. 55).
161. Togo, A., Chaput, L., Tanaka, I. & Hug, G. "First-principles phonon calculations of thermal expansion in Ti<sub>3</sub>SiC<sub>2</sub>, Ti<sub>3</sub>AlC<sub>2</sub>, and Ti<sub>3</sub>GeC<sub>2</sub>". *Phys. Rev. B* **81**, 174301 (17 May 2010) (cit. on p. 56).
162. Togo, A. "phonopy". <https://atztogo.github.io/phonopy/> (2017) (cit. on p. 56).
163. Sa, B., Li, Y.-L., Qi, J., Ahuja, R. & Sun, Z. "Strain Engineering for Phosphorene: The Potential Application as a Photocatalyst". *The Journal of Physical Chemistry C* **118**, 26560–26568 (2014) (cit. on p. 56).

164. Fei, R. & Yang, L. "Lattice vibrational modes and Raman scattering spectra of strained phosphorene". *Appl. Phys. Lett.* **105**, 083120 (2014) (cit. on pp. 56, 124).
165. Fei, R. & Yang, L. "Strain-Engineering the Anisotropic Electrical Conductance of Few-Layer Black Phosphorus". *Nano Lett.* **14**, 2884–2889 (2014) (cit. on p. 57).
166. Jiang, J.-W. & Park, H. S. "Negative poisson's ratio in single-layer black phosphorus". *Nat. Commun.* **5**, 4727 (Aug. 2014) (cit. on p. 58).
167. Jariwala, D., Sangwan, V. K., Lauhon, L. J., Marks, T. J. & Hersam, M. C. "Emerging Device Applications for Semiconducting Two-Dimensional Transition Metal Dichalcogenides". *ACS Nano* **8**, 1102–1120 (2014) (cit. on p. 60).
168. Duerloo, K.-A. N., Ong, M. T. & Reed, E. J. "Intrinsic Piezoelectricity in Two-Dimensional Materials". *The Journal of Physical Chemistry Letters* **3**, 2871–2876 (2012) (cit. on pp. 61–63, 65, 67, 68).
169. Zhu, H., Wang, Y., Xiao, J., Liu, M., Xiong, S., Wong, Z. J., Ye, Z., Ye, Y., Yin, X. & Zhang, X. "Observation of piezoelectricity in free-standing monolayer MoS<sub>2</sub>". *Nature nanotechnology* **10**, 151–155 (2015) (cit. on pp. 61, 68).
170. Li, W. & Li, J. "Piezoelectricity in two-dimensional group-III monochalcogenides". *Nano Research* **8**, 3796–3802 (Dec. 2015) (cit. on p. 61).
171. Xiang, H. J., Yang, J., Hou, J. G. & Zhu, Q. "Piezoelectricity in ZnO nanowires: A first-principles study". *Appl. Phys. Lett.* **89**, 223111 (2006) (cit. on p. 61).
172. Tomasz, G. & Zielinski, W. "How does a piezoelectric igniter work?" <<https://qph.ec.quoracdn.net/main-qimg-b9c33a87f3be9dd104214145364cfaf2>> (2013) (cit. on p. 62).
173. Baroni, S., de Gironcoli, S., Dal Corso, A. & Giannozzi, P. "Phonons and related crystal properties from density-functional perturbation theory". *Rev. Mod. Phys.* **73**, 515–562 (2 July 2001) (cit. on pp. 62, 106).
174. Wu, X., Vanderbilt, D. & Hamann, D. R. "Systematic treatment of displacements, strains, and electric fields in density-functional perturbation theory". *Phys. Rev. B* **72**, 035105 (3 July 2005) (cit. on p. 62).
175. Vanderbilt, D. "Berry-phase theory of proper piezoelectric response". *J. Phys. Chem. Solids* **61**, 147–151 (2000) (cit. on pp. 62, 64, 67).
176. Ong, M. T., Duerloo, K.-A. N. & Reed, E. J. "The Effect of Hydrogen and Fluorine Coadsorption on the Piezoelectric Properties of Graphene". *The Journal of Physical Chemistry C* **117**, 3615–3620 (2013) (cit. on p. 63).
177. Kim, H. J., Noor-A-Alam, M., Son, J. Y. & Shin, Y.-H. "Origin of piezoelectricity in monolayer halogenated graphane piezoelectrics". *Chem. Phys. Lett.* **603**, 62–66 (2014) (cit. on p. 63).
178. Rasmussen, F. A. & Thygesen, K. S. "Computational 2D Materials Database: Electronic Structure of Transition-Metal Dichalcogenides and Oxides". *The Journal of Physical Chemistry C* **119**, 13169–13183 (2015) (cit. on p. 64).

179. Ataca, C., Şahin, H. & Ciraci, S. "Stable, Single-Layer MX<sub>2</sub> Transition-Metal Oxides and Dichalcogenides in a Honeycomb-Like Structure". *The Journal of Physical Chemistry C* **116**, 8983–8999 (2012) (cit. on p. 65).
180. Guo, H., Lu, N., Wang, L., Wu, X. & Zeng, X. C. "Tuning Electronic and Magnetic Properties of Early Transition-Metal Dichalcogenides via Tensile Strain". *The Journal of Physical Chemistry C* **118**, 7242–7249 (2014) (cit. on p. 65).
181. Peng, Q. & De, S. "Outstanding mechanical properties of monolayer MoS<sub>2</sub> and its application in elastic energy storage". *Phys. Chem. Chem. Phys.* **15**, 19427–19437 (44 2013) (cit. on p. 65).
182. Kang, J., Tongay, S., Zhou, J., Li, J. & Wu, J. "Band offsets and heterostructures of two-dimensional semiconductors". *Appl. Phys. Lett.* **102**, 012111 (2013) (cit. on p. 65).
183. Born, M. & Huang, K. *Dynamical Theory of Crystal Lattices* (Clarendon Press, 1998) (cit. on p. 65).
184. Zhuang, H. L., Johannes, M. D., Blonsky, M. N. & Hennig, R. G. "Computational prediction and characterization of single-layer CrS<sub>2</sub>". *Appl. Phys. Lett.* **104**, 022116 (2014) (cit. on p. 67).
185. Michel, K. H. & Verberck, B. "Theory of elastic and piezoelectric effects in two-dimensional hexagonal boron nitride". *Phys. Rev. B* **80**, 224301 (22 Dec. 2009) (cit. on p. 67).
186. Michel, K. H. & Verberck, B. "Phonon dispersions and piezoelectricity in bulk and multilayers of hexagonal boron nitride". *Phys. Rev. B* **83**, 115328 (11 Mar. 2011) (cit. on p. 67).
187. Michel, K. H. & Verberck, B. "Theory of phonon dispersions and piezoelectricity in multilayers of hexagonal boron-nitride". *physica status solidi (b)* **248**, 2720–2723 (2011) (cit. on p. 67).
188. Ong, M. T. & Reed, E. J. "Engineered Piezoelectricity in Graphene". *ACS Nano* **6**, 1387–1394 (2012) (cit. on p. 69).
189. Bechmann, R. "Elastic and Piezoelectric Constants of Alpha-Quartz". *Phys. Rev.* **110**, 1060–1061 (5 June 1958) (cit. on p. 69).
190. Lueng, C. M., Chan, H. L. W., Surya, C. & Choy, C. L. "Piezoelectric coefficient of aluminum nitride and gallium nitride". *J. Appl. Phys.* **88**, 5360–5363 (2000) (cit. on p. 69).
191. KAN, E., LI, Z. & YANG, J. "MAGNETISM IN GRAPHENE SYSTEMS". *Nano* **03**, 433–442 (Dec. 2008) (cit. on p. 71).
192. Xu, K., Li, X., Chen, P., Zhou, D., Wu, C., Guo, Y., Zhang, L., Zhao, J., Wu, X. & Xie, Y. "Hydrogen dangling bonds induce ferromagnetism in two-dimensional metal-free graphitic-C<sub>3</sub>N<sub>4</sub> nanosheets". *Chem. Sci.* **6**, 283–287 (1 2015) (cit. on p. 71).

193. Eng, A. Y. S., Poh, H. L., Šaněk, F., Maryško, M., Matějková, S., Sofer, Z. & Pumera, M. "Searching for Magnetism in Hydrogenated Graphene: Using Highly Hydrogenated Graphene Prepared via Birch Reduction of Graphite Oxides". *ACS Nano* **7**, 5930–5939 (July 2013) (cit. on p. 71).
194. Okada, S. & Oshiyama, A. "Magnetic Ordering in Hexagonally Bonded Sheets with First-Row Elements". *Phys. Rev. Lett.* **87**, 146803 (14 Sept. 2001) (cit. on p. 71).
195. Miao, Q., Wang, L., Liu, Z., Wei, B., Xu, F. & Fei, W. "Magnetic properties of N-doped graphene with high Curie temperature". *Sci. Rep.* **6**, 21832 (Feb. 2016) (cit. on p. 71).
196. Pereira, V. M., Guinea, F., Lopes dos Santos, J. M. B., Peres, N. M. R. & Castro Neto, A. H. "Disorder Induced Localized States in Graphene". *Phys. Rev. Lett.* **96**, 036801 (3 Jan. 2006) (cit. on p. 71).
197. Yazyev, O. V. & Helm, L. "Defect-induced magnetism in graphene". *Phys. Rev. B* **75**, 125408 (12 Mar. 2007) (cit. on p. 71).
198. Baughman, R., Eckhardt, H. & Kertesz, M. "Structure-property predictions for new planar forms of carbon: Layered phases containing sp<sup>2</sup> and sp atoms". *The Journal of chemical physics* **87**, 6687–6699 (1987) (cit. on p. 71).
199. Ivanovskii, A. "Graphynes and graphdyines". *Prog. Solid State Chem.* **41**, 1–19 (2013) (cit. on p. 71).
200. Zhang, S., Zhou, J., Wang, Q., Chen, X., Kawazoe, Y. & Jena, P. "Penta-graphene: A new carbon allotrope". *PNAS* **112**, 2372–2377 (Feb. 2015) (cit. on pp. 71, 108).
201. Wang, F. Q., Yu, J., Wang, Q., Kawazoe, Y. & Jena, P. "Lattice thermal conductivity of penta-graphene". *Carbon* **105**, 424–429 (2016) (cit. on p. 71).
202. Yu, Z. G. & Zhang, Y.-W. "A comparative density functional study on electrical properties of layered penta-graphene". *J. Appl. Phys.* **118**, 165706 (2015) (cit. on p. 71).
203. Berdiyorov, G. R. & Madjet, M. E.-A. "First-principles study of electronic transport and optical properties of penta-graphene, penta-SiC<sub>2</sub> and penta-CN<sub>2</sub>". *RSC Adv.* **6**, 50867–50873 (56 2016) (cit. on p. 71).
204. Momma, K. & Izumi, F. "VESTA3 for three-dimensional visualization of crystal, volumetric and morphology data". *J. Appl. Cryst.* **44**, 1272–1276 (Dec. 2011) (cit. on pp. 72, 112).
205. Zhang, X., Wei, L., Tan, J. & Zhao, M. "Prediction of an ultrasoft graphene allotrope with Dirac cones". *Carbon N. Y.* **105**, 323–329 (Aug. 2016) (cit. on p. 74).
206. Wang, X., Weng, Q., Yang, Y., Bando, Y. & Golberg, D. "Hybrid two-dimensional materials in rechargeable battery applications and their microscopic mechanisms". *Chem. Soc. Rev.* **45**, 4042–4073 (15 2016) (cit. on p. 77).

207. Pomerantseva, E. & Gogotsi, Y. "Two-dimensional heterostructures for energy storage". *Nature Energy* **2**, 17089 (June 2017) (cit. on p. 77).
208. Cakir, D., Sevik, C., Gulseren, O. & Peeters, F. M. "Mo<sub>2</sub>C as a high capacity anode material: a first-principles study". *J. Mater. Chem. A* **4**, 6029–6035 (16 2016) (cit. on pp. 77, 86).
209. Ren, C. E., Zhao, M.-Q., Makaryan, T., Halim, J., Boota, M., Kota, S., Anasori, B., Barsoum, M. W. & Gogotsi, Y. "Porous Two-Dimensional Transition Metal Carbide (MXene) Flakes for High-Performance Li-Ion Storage". *ChemElectroChem* **3**, 689–693 (2016) (cit. on p. 77).
210. Naguib, M., Halim, J., Lu, J., Cook, K. M., Hultman, L., Gogotsi, Y. & Barsoum, M. W. "New Two-Dimensional Niobium and Vanadium Carbides as Promising Materials for Li-Ion Batteries". *Journal of the American Chemical Society* **135**, 15966–15969 (2013) (cit. on pp. 77, 86).
211. Eames, C. & Islam, M. S. "Ion Intercalation into Two-Dimensional Transition-Metal Carbides: Global Screening for New High-Capacity Battery Materials". *Journal of the American Chemical Society* **136**, 16270–16276 (2014) (cit. on p. 77).
212. Kresse, G. & Furthmüller, J. "Efficiency of ab-initio total energy calculations for metals and semiconductors using a plane-wave basis set". *Comput. Mater. Sci.* **6**, 15–50 (1996) (cit. on p. 78).
213. Kresse, G. & Furthmüller, J. "Efficient iterative schemes for *ab initio* total-energy calculations using a plane-wave basis set". *Phys. Rev. B* **54**, 11169–11186 (Oct. 1996) (cit. on p. 78).
214. Perdew, J. P., Burke, K. & Ernzerhof, M. "Generalized Gradient Approximation Made Simple". *Phys. Rev. Lett.* **77**, 3865–3868 (Oct. 1996) (cit. on p. 78).
215. Grimme, S., Ehrlich, S. & Goerigk, L. "Effect of the damping function in dispersion corrected density functional theory". *Journal of Computational Chemistry* **32**, 1456–1465 (2011) (cit. on p. 78).
216. Tang, W., Sanville, E. & Henkelman, G. "A grid-based Bader analysis algorithm without lattice bias". *J. Phys.: Condens. Matter* **21**, 084204 (2009) (cit. on pp. 78, 96).
217. Sanville, E., Kenny, S. D., Smith, R. & Henkelman, G. "Improved grid-based algorithm for Bader charge allocation". *J. Comput. Chem.* **28**, 899–908 (2007) (cit. on pp. 78, 96).
218. Henkelman, G., Arnaldsson, A. & Jónsson, H. "A fast and robust algorithm for Bader decomposition of charge density". *Computational Materials Science* **36**, 354–360 (2006) (cit. on pp. 78, 96).
219. Yu, M. & Trinkle, D. R. "Accurate and efficient algorithm for Bader charge integration". *The Journal of Chemical Physics* **134** (2011) (cit. on p. 78).

220. Henkelman, G., Uberuaga, B. P. & Jansson, H. "A climbing image nudged elastic band method for finding saddle points and minimum energy paths". *The Journal of Chemical Physics* **113**, 9901–9904 (2000) (cit. on p. 78).
221. Henkelman, G. & Jansson, H. "Improved tangent estimate in the nudged elastic band method for finding minimum energy paths and saddle points". *The Journal of Chemical Physics* **113**, 9978–9985 (2000) (cit. on p. 78).
222. Mostaani, E., Drummond, N. D. & Fal'ko, V. I. "Quantum Monte Carlo Calculation of the Binding Energy of Bilayer Graphene". *Phys. Rev. Lett.* **115**, 115501 (11 Sept. 2015) (cit. on p. 80).
223. Guo, G.-C., Wang, D., Wei, X.-L., Zhang, Q., Liu, H., Lau, W.-M. & Liu, L.-M. "First-Principles Study of Phosphorene and Graphene Heterostructure as Anode Materials for Rechargeable Li Batteries". *J. Phys. Chem. Lett.* **6**, 5002–5008 (Dec. 2015) (cit. on p. 80).
224. Samad, A., Noor-A-Alam, M. & Shin, Y.-H. "First principles study of a SnS<sub>2</sub>/graphene heterostructure: a promising anode material for rechargeable Na ion batteries". *J. Mater. Chem. A* **4**, 14316–14323 (2016) (cit. on p. 80).
225. Lee, E. & Persson, K. A. "Li Absorption and Intercalation in Single Layer Graphene and Few Layer Graphene by First Principles". *Nano Lett.* **12**, 4624–4628 (Sept. 2012) (cit. on p. 80).
226. Ashton, M., Hennig, R. G. & Sinnott, S. B. "Computational characterization of lightweight multilayer MXene Li-ion battery anodes". *Applied Physics Letters* **108**, 023901 (2016) (cit. on p. 80).
227. Shirodkar, S. N. & Kaxiras, E. "Li intercalation at graphene/hexagonal boron nitride interfaces". *Phys. Rev. B* **93**, 245438 (24 June 2016) (cit. on p. 83).
228. Sun, D., Hu, Q., Chen, J., Zhang, X., Wang, L., Wu, Q. & Zhou, A. "Structural Transformation of MXene (V<sub>2</sub>C, Cr<sub>2</sub>C, and Ta<sub>2</sub>C) with O Groups during Lithiation: A First-Principles Investigation". *ACS Applied Materials & Interfaces* **8**, 74–81 (2016) (cit. on p. 84).
229. Xie, Y., Naguib, M., Mochalin, V. N., Barsoum, M. W., Gogotsi, Y., Yu, X., Nam, K.-W., Yang, X.-Q., Kolesnikov, A. I. & Kent, P. R. C. "Role of Surface Structure on Li-Ion Energy Storage Capacity of Two-Dimensional Transition-Metal Carbides". *J. Am. Chem. Soc.* **136**, 6385–6394 (Apr. 2014) (cit. on p. 86).
230. Tang, Q., Zhou, Z. & Shen, P. "Are MXenes Promising Anode Materials for Li Ion Batteries? Computational Studies on Electronic Properties and Li Storage Capability of Ti<sub>3</sub>C<sub>2</sub> and Ti<sub>3</sub>C<sub>2</sub>X<sub>2</sub> (X = F, OH) Monolayer". *J. Am. Chem. Soc.* **134**, 16909–16916 (Oct. 2012) (cit. on p. 86).
231. Persson, K., Hinuma, Y., Meng, Y. S., Van der Ven, A. & Ceder, G. "Thermodynamic and kinetic properties of the Li-graphite system from first-principles calculations". *Phys. Rev. B* **82**, 125416 (12 Sept. 2010) (cit. on p. 86).

232. Koudriachova, M. V., Harrison, N. M. & de Leeuw, S. W. "Open circuit voltage profile for Li-intercalation in rutile and anatase from first principles". *Solid State Ionics* **152–153**. {PROCEEDINGS} {OF} {INTERNATIONAL} {CONFERENCE} {ON} {SOLID} {STATE} IONICS, (MATERIALS {AND} {PROCESSES} {FOR} {ENERGY} {AND} ENVIRONMENT), CAIRNS, AUSTRALIA, 8-13 JULY, 2001, 189–194 (2002) (cit. on p. 86).
233. Li, W., Yang, Y., Zhang, G. & Zhang, Y.-W. "Ultrafast and Directional Diffusion of Lithium in Phosphorene for High-Performance Lithium-Ion Battery". *Nano Letters* **15**, 1691–1697 (2015) (cit. on p. 86).
234. M., N., J., C., B., D., V., P., L., T. P., P., S., W., B. M. & Y., G. "MXene: A promising transition metal carbide anode for lithium-ion batteries". *Electrochim. Commun.* **16**, 61 (2012) (cit. on p. 86).
235. Zhao, S., Kang, W. & Xue, J. "Role of Strain and Concentration on the Li Adsorption and Diffusion Properties on Ti<sub>2</sub>C Layer". *The Journal of Physical Chemistry C* **118**, 14983–14990 (2014) (cit. on p. 87).
236. Thinius, S., Islam, M. M., Heitjans, P. & Bredow, T. "Theoretical Study of Li Migration in Lithium?Graphite Intercalation Compounds with Dispersion-Corrected DFT Methods". *The Journal of Physical Chemistry C* **118**, 2273–2280 (2014) (cit. on p. 87).
237. Lunell, S., Stashans, A., Ojamae, L., Lindstrom, H. & Hagfeldt, A. "Li and Na Diffusion in TiO<sub>2</sub> from Quantum Chemical Theory versus Electrochemical Experiment". *Journal of the American Chemical Society* **119**, 7374–7380 (1997) (cit. on p. 88).
238. Lindstram, H., Sadegren, S., Solbrand, A., Rensmo, H., Hjelm, J., Hagfeldt, A. & Lindquist, S.-E. "Li<sup>+</sup> Ion Insertion in TiO<sub>2</sub> (Anatase). 1. Chronoamperometry on CVD Films and Nanoporous Films". *The Journal of Physical Chemistry B* **101**, 7710–7716 (1997) (cit. on p. 88).
239. Olson, C. L., Nelson, J. & Islam, M. S. "Defect Chemistry, Surface Structures, and Lithium Insertion in Anatase TiO<sub>2</sub>". *The Journal of Physical Chemistry B* **110**, 9995–10001 (2006) (cit. on p. 88).
240. Luo, J., Zhang, W., Yuan, H., Jin, C., Zhang, L., Huang, H., Liang, C., Xia, Y., Zhang, J., Gan, Y. & Tao, X. "Pillared Structure Design of MXene with Ultralarge Interlayer Spacing for High-Performance Lithium-Ion Capacitors". *ACS Nano* **11**, 2459–2469 (2017) (cit. on p. 88).
241. Lieth, R. *Preparation and crystal growth of materials with layered structures* (Springer, 1977) (cit. on p. 94).
242. Meade, C. & Jeanloz, R. "Static compression of Ca(OH)<sub>2</sub> at room temperature: Observations of amorphization and equation of state measurements to 10.7 GPa". *Geophys. Res. Lett.* **17**, 1157–1160 (1990) (cit. on p. 94).
243. Kruger, M. B., Williams, Q. & Jeanloz, R. "Vibrational spectra of Mg(OH)<sub>2</sub> and Ca(OH)<sub>2</sub> under pressure". *The Journal of Chemical Physics* **91**, 5910–5915 (1989) (cit. on p. 94).

244. Nguyen, J. H., Kruger, M. B. & Jeanloz, R. "Evidence for "Partial" (Sublattice) Amorphization in  $\text{Co(OH)}_2$ ". *Phys. Rev. Lett.* **78**, 1936–1939 (10 Mar. 1997) (cit. on p. 94).
245. Raugei, S., Silvestrelli, P. L. & Parrinello, M. "Pressure-Induced Frustration and Disorder in  $\text{Mg(OH)}_2$  and  $\text{Ca(OH)}_2$ ". *Phys. Rev. Lett.* **83**, 2222–2225 (11 Sept. 1999) (cit. on p. 94).
246. Duffy, T. S., Meade, C., Fei, Y., Mao, H.-K. & Hemley, R. J. "High-pressure phase transition in brucite,  $\text{Mg(OH)}_2$ ". *Am. Mineral.* **80**, 222–230 (1995) (cit. on p. 94).
247. Ekbundit, S., Leinenweber, K., Yarger, J., Robinson, J., Verhelst-Voorhees, M. & Wolf, G. "New High-Pressure Phase and Pressure-Induced Amorphization of  $\text{Ca(OH)}_2$ : Grain Size Effect". *J. Solid State Chem.* **126**, 300–307 (1996) (cit. on p. 94).
248. Catalli, K., Shim, S.-H. & Prakapenka, V. B. "A crystalline-to-crystalline phase transition in  $\text{Ca(OH)}_2$  at 8 GPa and room temperature". *Geophys. Res. Lett.* **35**, L05312 (2008) (cit. on p. 94).
249. Iizuka, R., Kagi, H., Komatsu, K., Ushijima, D., Nakano, S., Sano-Furukawa, A., Nagai, T. & Yagi, T. "Pressure responses of portlandite and H-D isotope effects on pressure-induced phase transitions". *Phys. Chem. Miner.* **38**, 777–785 (Dec. 2011) (cit. on p. 94).
250. Winkler, B., Milman, V., Hennion, B., Payne, M., Lee, M.-H. & Lin, J. "Ab initio total energy study of brucite, diaspore and hypothetical hydrous wadsleyite". *English. Phys. Chem. Miner.* **22**, 461–467 (1995) (cit. on p. 94).
251. Baranek, P., Lichanot, A., Orlando, R. & Dovesi, R. "Structural and vibrational properties of solid  $\text{Mg(OH)}_2$  and  $\text{Ca(OH)}_2$  – performances of various hamiltonians". *Chemical Physics Letters* **340**, 362–369 (2001) (cit. on p. 94).
252. Azuma, K., Oda, T. & Tanaka, S. "Vibration analysis of O–H stretching mode in  $\text{Mg(OH)}_2$ ,  $\text{Ca(OH)}_2$ ,  $\text{LiOH}$ , and  $\text{NaOH}$  by plane-wave pseudopotential DFT calculation". *Comput. Theor. Chem.* **963**, 215–220 (Jan. 2011) (cit. on p. 94).
253. D'Arco, P., Causà, M., Roetti, C. & Silvi, B. "Periodic Hartree-Fock study of a weakly bonded layer structure: Brucite  $\text{Mg(OH)}_2$ ". *Phys. Rev. B* **47**, 3522–3529 (7 Feb. 1993) (cit. on pp. 94, 102).
254. Pishtshev, A., Karazhanov, S. Z. & Klopov, M. "Materials properties of magnesium and calcium hydroxides from first-principles calculations". *Computational Materials Science* **95**, 693–705 (2014) (cit. on pp. 94, 98, 99).
255. Pishtshev, A., Karazhanov, S. Z. & Klopov, M. "Excitons in  $\text{Mg(OH)}_2$  and  $\text{Ca(OH)}_2$  from ab initio calculations". *Solid State Commun.* **193**, 11–15 (2014) (cit. on p. 94).

256. Ren, W. & Cheng, H.-M. *The global growth of graphene* Oct. 2014. doi:10.1038/nnano.2014.229 (cit. on p. 94).
257. Yu, Y., Li, C., Liu, Y., Su, L., Zhang, Y. & Cao, L. *Controlled Scalable Synthesis of Uniform, High-Quality Monolayer and Few-layer MoS<sub>2</sub> Films* May 2013. doi:10.1038/srep01866 (cit. on p. 94).
258. Alfè, D. "PHON: A program to calculate phonons using the small displacement method". *Comput. Phys. Commun.* **180**, 40 YEARS OF CPC: A celebratory issue focused on quality software for high performance, grid and novel computing architectures, 2622–2633 (2009) (cit. on pp. 95, 106).
259. Grimme, S. "Semiempirical GGA-type density functional constructed with a long-range dispersion correction". *J. Comput. Chem.* **27**, 1787–1799 (2006) (cit. on p. 96).
260. Desgranges, L., Grebille, D., Calvarin, G., Chevrier, G., Floquet, N. & Niepce, J.-C. "Hydrogen thermal motion in calcium hydroxide: Ca(OH)<sub>2</sub>". *Acta Crystallographica Section B* **49**, 812–817 (Oct. 1993) (cit. on p. 99).
261. Busing, W. R. & Levy, H. A. "Neutron Diffraction Study of Calcium Hydroxide". *The Journal of Chemical Physics* **26**, 563–568 (1957) (cit. on p. 99).
262. Ataca, C., Topsakal, M., Aktürk, E. & Ciraci, S. "A Comparative Study of Lattice Dynamics of Three- and Two-Dimensional MoS<sub>2</sub>". *The Journal of Physical Chemistry C* **115**, 16354–16361 (2011) (cit. on p. 99).
263. Topsakal, M., Aktürk, E. & Ciraci, S. "First-principles study of two- and one-dimensional honeycomb structures of boron nitride". *Phys. Rev. B* **79**, 115442 (11 Mar. 2009) (cit. on p. 100).
264. Peng, Q., Ji, W. & De, S. "Mechanical properties of the hexagonal boron nitride monolayer: Ab initio study". *Computational Materials Science* **56**, 11–17 (2012) (cit. on p. 100).
265. Şahin, H., Cahangirov, S., Topsakal, M., Bekaroglu, E., Akturk, E., Senger, R. T. & Ciraci, S. "Monolayer honeycomb structures of group-IV elements and III-V binary compounds: First-principles calculations". *Phys. Rev. B* **80**, 155453 (15 Oct. 2009) (cit. on p. 100).
266. Posternak, M., Baldereschi, A., Freeman, A. J. & Wimmer, E. "Prediction of Electronic Surface States in Layered Materials: Graphite". *Phys. Rev. Lett.* **52**, 863–866 (10 Mar. 1984) (cit. on p. 105).
267. Posternak, M., Baldereschi, A., Freeman, A. J., Wimmer, E. & Weinert, M. "Prediction of Electronic Interlayer States in Graphite and Reinterpretation of Alkali Bands in Graphite Intercalation Compounds". *Phys. Rev. Lett.* **50**, 761–764 (10 Mar. 1983) (cit. on p. 105).
268. Greaves, G. N., Greer, A. L., Lakes, R. S. & Rouxel, T. "Poisson's ratio and modern materials". *Nat. Mater.* **10**, 823–837 (Oct. 2011) (cit. on p. 106).

269. Ding, Y. & Wang, Y. "Hydrogen-induced stabilization and tunable electronic structures of penta-silicene: a computational study". *J. Mater. Chem. C* **3**, 11341–11348 (2015) (cit. on pp. 108, 110).
270. Li, X., Dai, Y., Li, M., Wei, W. & Huang, B. "Stable Si-based pentagonal monolayers: high carrier mobilities and applications in photocatalytic water splitting". *J. Mater. Chem. A* **3**, 24055–24063 (2015) (cit. on pp. 108, 110).
271. Parrinello, M. & Rahman, A. "Crystal Structure and Pair Potentials: A Molecular-Dynamics Study". *Phys. Rev. Lett.* **45**, 1196–1199 (14 Oct. 1980) (cit. on p. 109).
272. Parrinello, M. & Rahman, A. "Polymorphic transitions in single crystals: A new molecular dynamics method". *J. Appl. Phys.* **52**, 7182–7190 (1981) (cit. on p. 109).
273. Allen, M. & Tildesley, D. *Computer Simulation of Liquids* (Clarendon Press, 1989) (cit. on p. 109).
274. Caliste, D. "V\_Sim atomic visualization package available online". <[http://inac.cea.fr/L\\_Sim/V\\_Sim/index.en.html](http://inac.cea.fr/L_Sim/V_Sim/index.en.html)> (2016) (cit. on p. 109).
275. Wang, Z., Dong, F., Shen, B., Zhang, R., Zheng, Y., Chen, L., Wang, S., Wang, C., Ho, K., Fan, Y.-J., Jin, B.-Y. & Su, W.-S. "Electronic and optical properties of novel carbon allotropes". *Carbon* **101**, 77–85 (2016) (cit. on p. 111).
276. Zhao, Z., Tian, F., Dong, X., Li, Q., Wang, Q., Wang, H., Zhong, X., Xu, B., Yu, D., He, J., Wang, H.-T., Ma, Y. & Tian, Y. "Tetragonal Allotrope of Group 14 Elements". *JACS* **134**, 12362–12365 (2012) (cit. on p. 111).
277. Morishita, T., Spencer, M. J., Russo, S. P., Snook, I. K. & Mikami, M. "Surface reconstruction of ultrathin silicon nanosheets". *Chem. Phys. Lett.* **506**, 221–225 (Apr. 2011) (cit. on p. 117).
278. Sakai, Y. & Oshiyama, A. "Structural stability and energy-gap modulation through atomic protrusion in freestanding bilayer silicene". *Phys. Rev. B* **91**, 201405 (May 2015) (cit. on p. 117).
279. Roldán, R., Castellanos-Gómez, A., Cappelluti, E. & Guinea, F. "Strain engineering in semiconducting two-dimensional crystals". *J. Phys.: Condens. Matter* **27**, 313201 (2015) (cit. on p. 125).
280. Geim, A. K. & Grigorieva, I. V. "Van der Waals heterostructures". *Nature* **499**, 419–425 (July 2013) (cit. on p. 129).
281. Liu, Y., Weiss, N. O., Duan, X., Cheng, H.-C., Huang, Y. & Duan, X. "Van der Waals heterostructures and devices". *Nat. Rev. Mater.* **1**, 16042 (July 2016) (cit. on p. 129).
282. Pomerantseva, E. & Gogotsi, Y. "Two-dimensional heterostructures for energy storage". *Nat. Energy* **2**, 17089 (June 2017) (cit. on p. 129).
283. Jena, D., Banerjee, K. & Xing, G. H. "2D crystal semiconductors: Intimate contacts". *Nat. Mater.* **13**, 1076–1078 (Nov. 2014) (cit. on p. 129).

284. Chhowalla, M., Voiry, D., Yang, J., Shin, H. S. & Loh, K. P. "Phase-engineered transition-metal dichalcogenides for energy and electronics". *MRS Bull.* **40**, 585–591 (July 2015) (cit. on p. 129).
285. Gong, Y., Lin, J., Wang, X., Shi, G., Lei, S., Lin, Z., Zou, X., Ye, G., Vajtai, R., Yakobson, B. I. & et al. "Vertical and in-plane heterostructures from WS<sub>2</sub>/MoS<sub>2</sub> monolayers". *Nature Materials* **13**, 1135–1142 (Sept. 2014) (cit. on p. 130).



# List of Publications

## Published

- P1. Yimamu, A., Beysen, S., Peng, D. & Aierken, Y. "Mixed-solvent thermal synthesis and magnetic properties of flower-like microstructured nickel". *Particuology* **10**, 392–396 (2012).
- P2. Aierken, Y., Çakır, D., Sevik, C. & Peeters, F. M. "Thermal properties of black and blue phosphorenes from a first-principles quasiharmonic approach". *Phys. Rev. B* **92**, 081408 (8 Aug. 2015) (cit. on pp. 51, 53, 121).
- P3. Alyörük, M. M., Aierken, Y., Çakır, D., Peeters, F. M. & Sevik, C. "Promising Piezoelectric Performance of Single Layer Transition-Metal Dichalcogenides and Dioxides". *The Journal of Physical Chemistry C* **119**, 23231–23237 (2015) (cit. on p. 60).
- P4. Aierken, Y., Leenaerts, O. & Peeters, F. M. "Intrinsic magnetism in penta-hexa-graphene: A first-principles study". *Phys. Rev. B* **94**, 155410 (15 Oct. 2016) (cit. on pp. 71, 125, 131).
- P5. Aierken, Y., Sahin, H., Iyikanat, F., Horzum, S., Suslu, A., Chen, B., Senger, R. T., Tongay, S. & Peeters, F. M. "Portlandite crystal: Bulk, bilayer, and monolayer structures". *Phys. Rev. B* **91**, 245413 (24 June 2015) (cit. on p. 93).
- P6. Aierken, Y., Leenaerts, O. & Peeters, F. M. "A first-principles study of stable few-layer penta-silicene". *Phys. Chem. Chem. Phys.* **18**, 18486–18492 (27 2016) (cit. on pp. 108, 119).

- P7. Aierken, Y., Çakır, D. & Peeters, F. M. "Strain enhancement of acoustic phonon limited mobility in monolayer TiS<sub>3</sub>". *Phys. Chem. Chem. Phys.* **18**, 14434–14441 (21 2016) (cit. on p. 125).
- P8. Aierken, Y., Leenaerts, O. & Peeters, F. M. "Defect-induced faceted blue phosphorene nanotubes". *Phys. Rev. B* **92**, 104104 (10 Sept. 2015) (cit. on p. 131).

## Under Review

- P9. Aierken, Y., Sevik, C., Gülseren, O., Peeters, F. M. & Çakır, D. "A first principles study of stacking and Lithium atom intercalation in MXenes/graphene heterostructures". in Preparation. 2017 (cit. on pp. 76, 131).
- P10. Aierken, Y., Leenaerts, O. & Peeters, F. M. "Edge-decoration of graphene nanoribbon with Nitrogens – A first principles study". in Preparation. 2017 (cit. on p. 129).
- P11. Aierken, Y., Sevik, C., Gülseren, O., Peeters, F. M. & Çakır, D. "In pursuit of barrierless transition metal dichalcogenides lateral heterojunctions". submitted to PCCP. June 2017 (cit. on p. 131).